Max-Planck-Institut für Meteorologie
Max Planck Institute for Meteorology

MAX-PLANCK-GESELLSCHAFT

Monitoring and detecting changes in the meridional overturning circulation at 26°N in the Atlantic Ocean - The simulation of an observing array in numerical models

Johanna Baehr

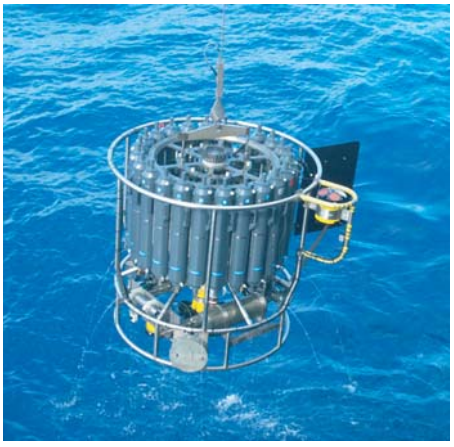

Berichte zur Erdsystemforschung 38/2006

Reports on Earth System Science

Hinweis

Die Berichte zur Erdsytemforschung werden vom Max-Planck-Institut für Meteorologie in Hamburg in unregelmäßiger Abfolge herausgegeben.

Sie enthalten wissenschaftliche und technische Beiträge, inklusive Dissertationen.

Die Beiträge geben nicht notwendigerweise die Auffassung des Instituts wieder.

Die "Berichte zur Erdsystemforschung" führen die vorherigen Reihen "Reports" und "Examensarbeiten" weiter.

Notice

The Reports on Earth System Science are published by the Max Planck Institute for Meteorology in Hamburg. They appear in irregular intervals.

They contain scientific and technical contributions, including Ph. D. theses.

The Reports do not necessarily reflect the opinion of the Institute.

The "Reports on Earth System Science" continue the former "Reports" and "Examensarbeiten" of the Max Planck Institute.

Anschrift / Address

Max-Planck-Institut für Meteorologie
Bundesstrasse 53
20146 Hamburg
Deutschland

Tel.: +49-(0)40-4 11 73-0
Fax: +49-(0)40-4 11 73-298
Web: www.mpimet.mpg.de

Layout:

Bettina Diallo, PR & Grafik

Titelfotos:
vorne:
Christian Klepp - Jochem Marotzke - Christian Klepp
hinten:
Clotilde Dubois - Christian Klepp - Katsumasa Tanaka

Berichte zur Erdsystemforschung 38/2006

Monitoring and detecting changes in the meridional overturning circulation at 26°N in the Atlantic Ocean - The simulation of an observing array in numerical models

Dissertation zur Erlangung des Doktorgrades der Naturwissenschaften
im Departement Geowissenschaften der Universität Hamburg
vorgelegt von

Johanna Baehr
aus Jena

Hamburg 2006

Reports on Earth System Science 38/2006

ISSN 1614-1199

Johanna Baehr
Max-Planck-Institut für Meteorologie
Bundesstrasse 53
20146 Hamburg
Germany

Als Dissertation angenommen
vom Departement Geowissenschaften der Universität Hamburg

auf Grund der Gutachten von
Prof. Dr. Jochem Marotzke
und
Prof. Dr. Detlef Stammer

Hamburg, den 4. Dezember 2006
Prof. Dr. Kay-Christian Emeis
Leiter des Departements für Geowissenschaften

ISSN 1614-1199

Monitoring and detecting changes in the meridional overturning circulation at 26°N in the Atlantic Ocean - The simulation of an observing array in numerical models

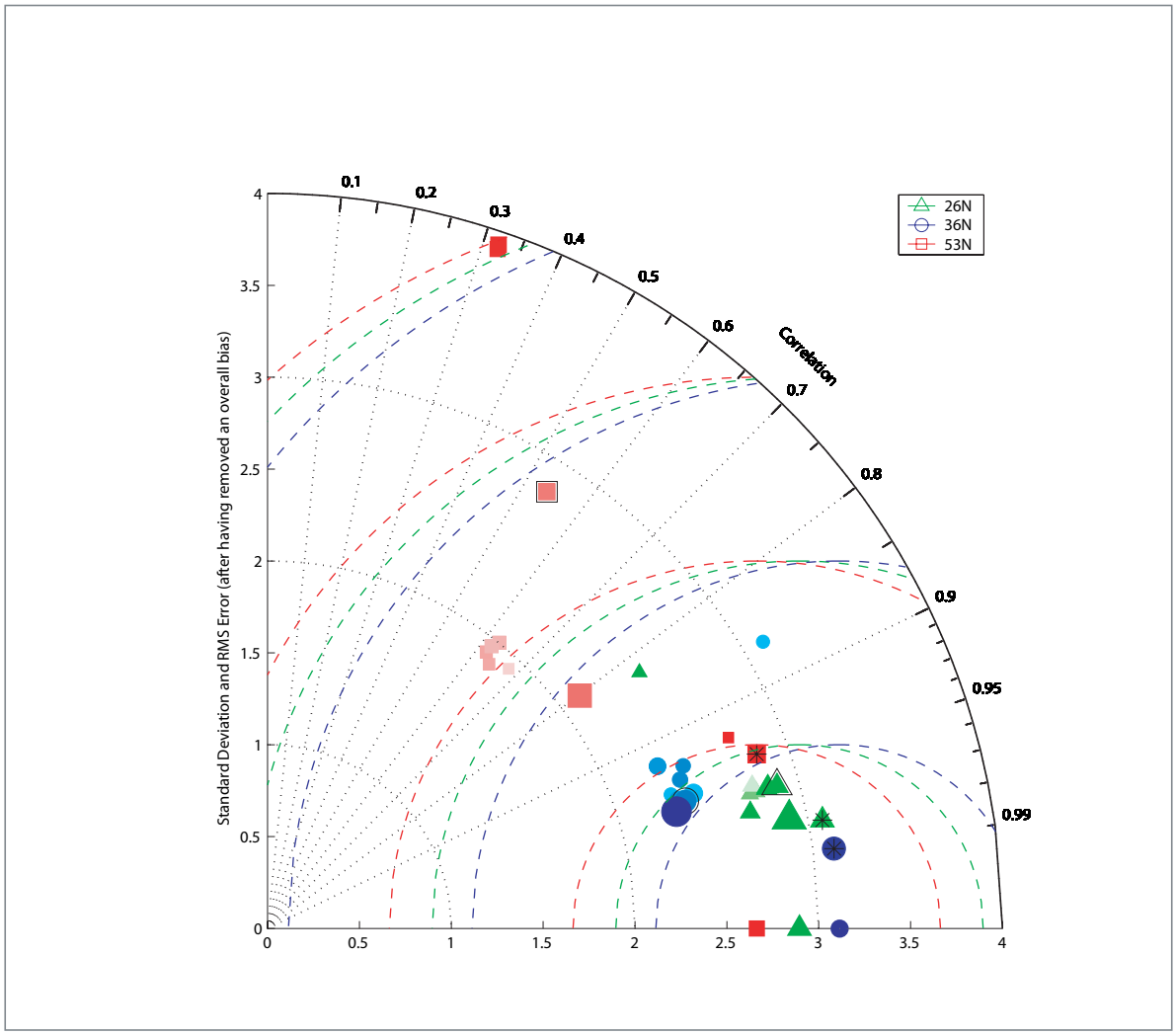

Johanna Baehr

Hamburg 2006

Abstract

A monitoring array for the continuous observation of the Atlantic meridional overturning circulation (MOC) is 'deployed' in numerical models. The objective is to improve the array's design, and to test its ability to observe changes in the MOC, allowing in turn to estimate detection times. The simulated monitoring array consists of continuous measurements of density and zonal wind stress along a longitude-depth transect. Meridional velocities are inferred from the thermal wind (using zonal density differences) and Ekman transports (using the zonal wind stress). The resulting meridional transport field is corrected by a spatially - but not temporally - constant correction to ensure zero net mass transport across the zonal section. The simulated array resembles the recently deployed RAPID-MOC 26°N array.

Using intuition-based array design, the simulated array is tested at three different latitudes. The MOC can only be reliably estimated at latitudes where either bottom velocities are small, or the complete bottom velocity field across the transect can be measured. If bottom velocities are negligible, about 10 density profiles can capture the temporal and vertical structure of the MOC for that latitude. Global optimization of the placement of density profiles can provide results of comparable quality as intuition-based array design. However, the interpretation requires caution as the optimal solution might arise because misfits compensate each other coincidentally.

The array is tested in a simulation of the IPCC (Intergovernmental Panel on Climate Change) scenario A1B in a coupled climate model. The simulated array is able to capture the short-term to long-term (*i.e.*, up to multidecadal) variability, as well as changes in the mean strength of the MOC induced by anthropogenic forcing. Hence, the array allows to detect MOC changes at 26°N based on an integrated MOC timeseries. Using a univariate detection analysis, an observation error of 3 Sv, and detection with 95 percent reliability, continuous observations based on the simulated array result in a detection time of 100 years, while frequent hydrographic occupations every 20 years result in a detection time of 120 years.

Comparing the five hydrographic occupations of the 26°N transect, and model simulations, I find that zonal density gradients yield a reliable detection variable for MOC changes at 26°N. Using a multivariate detection analysis, in a modified version of Hasselmann's fingerprint technique, detection of MOC changes based on the simulated array can be achieved within a couple of decades: for zonal density gradients between 1700 m and 3100 m at 26°N, with an assumed observation error of 0.01 kg m^{-3}, the detection time (95 percent reliability) is about 30 years.

The results from this thesis should be able to guide future MOC monitoring, and could serve as a reference point for observation-based detection of future MOC changes.

Zusammenfassung

In numerischen Modellen wird ein System zur kontinuierlichen Beobachtung der meridionalen Umwälzbewegung (meridional overturning circulation, MOC) im Atlantischen Ozean 'verankert'. Ziel ist, das Design des Beobachtungssystems zu verbessern und die Fähigkeit des Systems zu testen, Veränderungen zu beobachten, um auf diese Weise Entdeckungszeiten abzuschätzen zu können. Das simulierte Beobachtungssystem besteht aus kontinuierlichen Dichte- und Windstress-Messungen entlang eines Längen-Tiefe-Schnitts. Meridionale Geschwindigkeiten werden abgeleitet vom thermischen Wind (unter Verwendung zonaler Dichtedifferenzen) und Ekman-Transporten (unter Verwendung des zonalen Windstress). Das resultierende meridionale Transportfeld wird mittels eines räumlich - aber nicht zeitlich - konstanten Korrekturwertes berichtigt, der sicherstellt, dass der Netto-Masse-Transport über den zonalen Schnitt Null ist. Das simulierte Beobachtungssystem gleicht dem kürzlich verankerten RAPID-MOC-Beobachtungssystem bei 26°N.

Auf der Basis eines intuitiven Beobachtungssystem-Designs wird das simulierte System an drei unterschiedlichen Breiten getestet. Die MOC kann nur an Breiten verlässlich abgeschätzt werden, wo entweder die Bodengeschwindigkeiten klein sind oder das komplette Bodengeschwindigkeitsfeld entlang des Schnitts vermessen werden kann. Wenn die Bodengeschwindigkeiten zu vernachlässigen sind, können ca. 10 Dichteprofile die zeitliche und vertikale Struktur der MOC an diesen Breiten abbilden. Eine globale Optimierung der Positionierung der Dichteprofile kann Ergebnisse von vergleichbarer Qualität liefern wie ein intuitives Beobachtungssystem-Design. Diese Interpretation steht allerdings unter dem Vorbehalt, dass die optimale Lösung auch Ergebnis einer zufälligen Fehler-Kompensation sein kann.

Das Beobachtungssystem wird in einer Simulation des IPCC (Intergovernmental Panel on Climate Change) Szenarios A1B eines gekoppelten Klimamodells getestet. Das simulierte System ist in der Lage, die gesamte Bandbreite von kurz- bis zu langfristiger (d.h. multidekadischer) Variabilität abzubilden. Zudem kann es durch anthropogene Einflüsse hervorgerufene Änderungen in der mittleren Stärke der MOC abbilden. Deshalb erlaubt das Beobachtungssystem die Entdeckung von Veränderungen der MOC bei 26°N auf der Basis einer integrierten MOC-Zeitserie. Legt man eine univariate Entdeckungsanalyse, einen Beobachtungsfehler von 3 Sv und eine Entdeckung mit 95-prozentiger Sicherheit zu Grunde, führen kontinuierliche Beobachtungen auf der Grundlage des simulierten Systems zu einer Entdeckungszeit von 100 Jahren, während hydrographische Schnitte mit einem 20-Jahres-Rythmus zu einer Entdeckungszeit von 120 Jahren führen.

Ein Vergleich der fünf hydrographischen Vermessungen des Schnitts bei 26°N mit Modell-Simulationen ergibt, dass zonale Dichtedifferenzen eine verlässliche Entde-

ckungsvariable für Veränderungen der MOC bei 26°N liefern. Auf der Grundlage einer multivariaten Entdeckungsanalyse, die eine modifizierte Form von Hasselmanns Fingerabdruck-Technik darstellt, können Veränderungen der MOC mithilfe des simulierten Beobachtungssystems bereits innerhalb einiger Dekaden entdeckt werden: für zonale Dichtedifferenzen zwischen 1700 m und 3100 m Tiefe bei 26°N beträgt die Entdeckungszeit bei einem angenommenen Beobachtungsfehler von 0,01 kg m^{-3} mit 95-prozentiger Sicherheit ungefähr 30 Jahre.

Die Ergebnisse dieser Doktorarbeit sollen die künftige Überwachung der MOC anleiten und können als Referenz für eine beobachtungsbasierte Entdeckung von Veränderungen der MOC dienen.

CONTENTS

1. INTRODUCTION

1.1 Motivation

A variety of numerical models predict a change in the Earth's climate under the influence of anthropogenically increased atmospheric concentrations of greenhouse gases. In the ocean, one of the variables eminently associated with both past and future climate changes is the Atlantic meridional overturning circulation (MOC). The MOC is the zonally and vertically integrated meridional flow as a function of latitude and depth, which in the Atlantic comprises both a - dominating - buoyancy forced contribution, *i.e.*, the thermohaline circulation, and a wind-driven contribution. Numerical simulations suggest that the Atlantic MOC is sensitive to anthropogenic climate change (*e.g.*, Manabe and Stouffer, 1994; Mikolajewicz and Voss, 2000; Thorpe et al., 2001; Gregory et al., 2005), with potentially strong effects on the climate over the North Atlantic and its adjacent regions (Manabe and Stouffer, 1994; Vellinga and Wood, 2002). It is hence an important scientific task to detect an ongoing change in the MOC or predict an impending one. Doing so requires careful observation of the MOC.

Measurements of the MOC are, however, difficult to obtain. While ship-based transoceanic sections yield the most reliable estimates of the MOC (*e.g.*, Hall and Bryden, 1982; Ganachaud and Wunsch, 2000; Bryden et al., 2005), they deliver only temporal snapshots. At 26°N in the Atlantic, one of the most frequently occupied transoceanic sections, the MOC has been measured five times (1957, 1981, 1992, 1998, 2004) during last 50 years (Bryden et al., 2005). The resulting estimates of the meridional transport at 26°N point to considerable variations in the MOC: upper layer transports (above 1000 m) have increased from about -13 Sv (1957) to about -23 Sv (2004), whereas lower layer transports (3000 m to 5000 m) decreased from about -15 Sv (1957) to about -7 Sv (2004) (Bryden et al., 2005). Whether these variations mirror a decrease in the MOC or its natural variability has been widely discussed (*e.g.*, Kerr, 2005; Quadfasel, 2005). The temporally sparse sampling and the uncertainties associated with the unknown magnitude of natural variations in the MOC prohibit a conclusive answer to this question at present. To improve the assessment of MOC variations, continuous observations of the MOC are needed.

1.2 Continuous MOC Monitoring

A strategy to monitor the MOC continuously was proposed by Marotzke et al. (1999): in principle, only systematic observations of density at the eastern and western sidewalls would be required to monitor the MOC continuously. The conceptual starting point is the thermal wind relationship, which links the zonal density difference to the zonally averaged meridional flow. If the meridional flow were everywhere in thermal wind balance, and if there were vertical sidewalls and no bottom topography, the vertical structure of the MOC would be proportional to the east-west density difference. This relationship took center stage in the theory of a purely buoyancy-driven flow (Marotzke, 1997; Marotzke and Klinger, 2000). However, under more realistic circumstances, *i.e.*, with realistic wind forcing and irregular bottom topography, the situation becomes considerably more complicated: a time-varying Ekman contribution (Lee and Marotzke, 1998; Jayne and Marotzke, 2001), and the external mode (Robbins and Toole, 1997; Lee and Marotzke, 1998) have to be taken into account. Both of these contributions are not in thermal wind balance.

In the North Atlantic, the thermal wind part and the Ekman transport are the dominant contributions to the MOC (Köhl, 2005; Hirschi and Marotzke, 2006). Both contributions can be measured, the thermal wind contribution by zonal density gradients, and the Ekman contribution by zonal wind stress. Marotzke et al. (2002) formally proposed the deployment of such a monitoring array, and suggested 26°N for several reasons: (*i*) 26°N is one of the latitudes with the most frequent hydrographic occupations, (*ii*) 26°N is close to the meridional heat transport maximum (Trenberth and Solomon, 1994), thus capturing the entire ocean heat transport convergence into the North Atlantic, (*iii*) the western boundary current is largely confined to the Florida Strait, where cable measurements have been measuring the total mass transport for more than 20 years (Baringer and Larsen, 2001).

Prior to its deployment, the proposed MOC monitoring array was simulated in two numerical models - OCCAM: 1/4° resolution (Webb, 1996), and FLAME: 1/3° resolution (Dengg et al., 1999) - to test its feasibility (Hirschi et al., 2003). The simulated array consists of a suite of 'measurements':

1. continuous density 'measurements' with intensified coverage at the eastern and western boundary (figure 1.1a), resulting in an estimate of the thermal wind velocity v_g (figure 1.2),

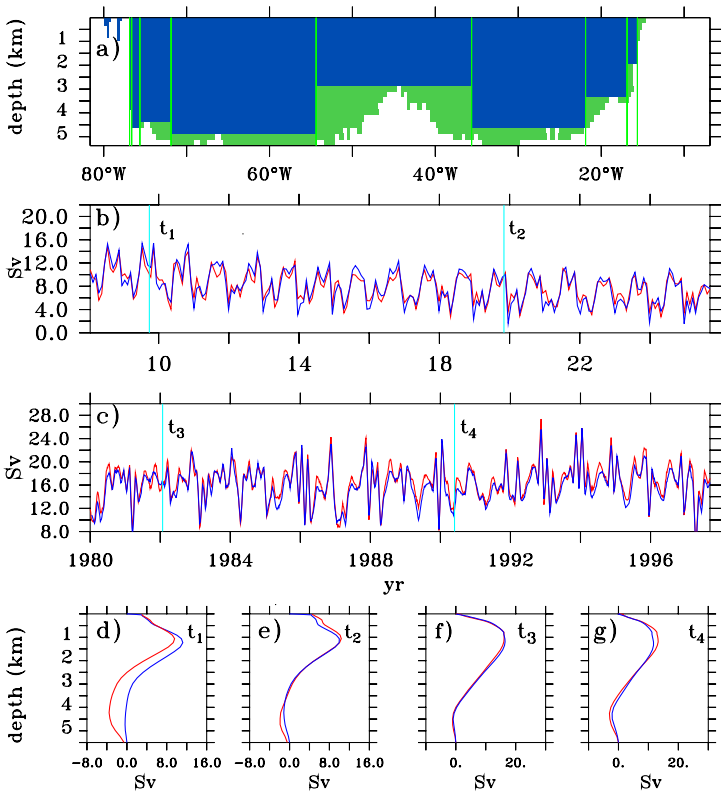

Fig. 1.1: Transport reconstructions based on 9 vertical profiles of density and Ekman contributions. (a) Distribution of vertical profiles in the OCCAM model (vertical green lines). The blue shading indicates where the vertical profiles provide an estimate of the velocity shear. In the green areas (bottom triangles) the vertical shear cannot be estimated from adjacent profiles. (b) and (c) timeseries comparing the reconstructed maximum meridional overturning (blue) with the maximum overturning derived from the full model velocities (red) at 26.5°N (OCCAM, panel b) and 26°N (FLAME, panel c). (d)-(g) comparison of simulated vertical flow patterns of the MOC (red) with its reconstructed estimate (blue). Snapshots are shown at different times (t_1 - t_4) for OCCAM (panels d, e), and FLAME (panels f, g). Figure re-printed from Hirschi et al. (2003).

2. 'observations' of zonal wind stress τ_x, resulting in the Ekman velocity v_{ek} (figure 1.2),

3. knowledge of the Florida Strait transport from cable measurements (Baringer and Larsen, 2001), resulting in a velocity field v_F (figure 1.2),

4. spatially - but not temporally - constant corrections for the Ekman velocity field (v_b), and the thermal wind and Florida Strait velocity field (v_c) (figure 1.2), ensuring mass balance, *i.e.* no net meridional transport across the zonal section (Hall and Bryden, 1982).

The reconstructed meridional velocity field, obtained from the contributions described above, was used to derive a reconstruction of the meridional transport

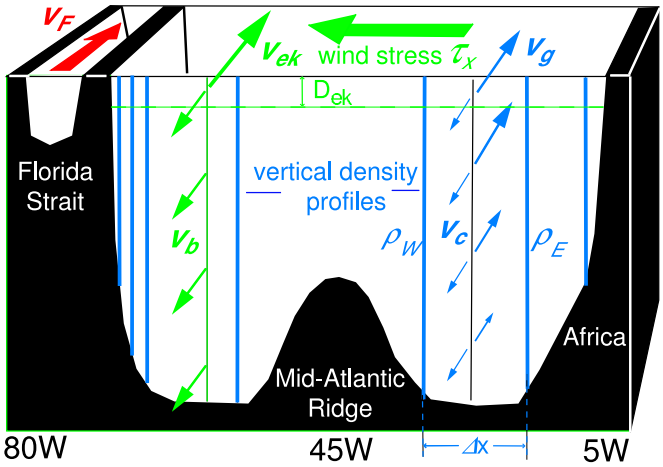

Fig. 1.2: Schematic of an MOC observing system across 26°N in the North Atlantic. The MOC is estimated from the zonal wind stress and from vertical density profiles taken at different longitudes across the basin. The transport across the Florida Strait is assumed to be known (v_F). From known wind stress, the Ekman velocity v_{ek} can be calculated. A constant return flow with velocity v_b is assumed over the whole water column in order to ensure zero net meridional transport related to wind stress. East of the Florida Strait a depth-dependent velocity field v_g is estimated using the thermal wind relation between adjacent density profiles. The meridional transport associated with v_g and v_F is compensated by a spatially constant velocity correction v_c in order to ensure zero net meridional transport for the thermal wind contribution. Figure re-printed from Hirschi et al. (2003).

(Hirschi et al., 2003). For both models, the reconstruction captures the time-mean value and the variability of the MOC timeseries quite well (figure 1.1b-c). The vertical structure is largely captured, although parts of the deep northward flow are missed (figure 1.1d-g).

The simulated measuring system resembles the subsequently deployed RAPID-MOC array (Schiermeier, 2004; Rayner, 2005), which is currently funded until 2008. Its moorings are currently replaced every year, some even semi-annually, and the results of the first and second years of deployment are presently analyzed.

1.3 Objective of the Thesis

With the deployment of the RAPID-MOC array, further questions arose regarding the underlying dynamics of the proposed monitoring strategy, and the timescale of observations needed to allow for a reliable MOC estimate. Here, I 'deploy' the proposed MOC monitoring array in numerical models to analyze different aspects of the array's performance. More specifically, five questions are investigated:

- Does a similar MOC monitoring array work at other - dynamically and geographically less special - latitudes in the North Atlantic?

- Can the intuition-based array design be improved by an optimized array design?

- Is the proposed 26°N MOC monitoring array able to reliably capture long-term changes in the MOC?

- Can changes in the MOC be detected faster with array measurements at 26°N or with repeated hydrographic transects?

- And, as a consecutive question to the preceding one: is it, based on the already existing measurements of density and related meridional transports at 26°N, possible to distinguish between natural variability and a real trend in the MOC strength?

The insights gained from this model-based observing array study are meant to guide future MOC monitoring. Here, I briefly describe the research interest in the questions posed above.

Previous observing array design did not - with the exception of Hackert et al. (1998) and Hirschi et al. (2003) - directly support instrument deployment. In contrast to Hirschi et al. (2003), here, I test the proposed MOC monitoring array at additional latitudes, and under a climate change scenario. Further, pre-deployment array design is conducted for the first time using formal optimization, *i.e.*, sequentially and globally optimized array design.

The results from the simulation of the proposed array under a climate change scenario are used to test the array's ability to detect changes in the MOC. Modifying the method of Santer et al. (1995) the detection of MOC changes is considered for a univariate MOC timeseries, accounting for the effects of observation errors, infrequent observations, and autocorrelated internal variability. To improve the detection times for changes in the MOC, a multivariate analysis is conducted subsequently, modifying the fingerprint method of Hasselmann (1979, 1993). The combination of a statistically rigorous detection algorithm and the requirement to rely solely on observable quantities enables the incorporation of real observations, allowing in turn a statement on whether MOC changes can be detected within the existing observations.

1.4 Outline of the Thesis

This thesis is a composite of four journal publications (chapters 2-5), of which one (chapter 3) is currently in preparation. This structure implies some recurrences as each chapter starts with its own abstract, followed by an introduction, and finishes with conclusions. The thesis is structured as follows.

In chapter 2, the proposed MOC monitoring array is tested at three different latitudes in the North Atlantic. The latitudes 26°N, 36°N, and 53°N differ in their dynamical and geographical setup, which allows one to draw fundamental conclusions about the force balance governing the MOC and the limitations of the applicability of the proposed MOC observing strategy. This chapter has been published in *Journal of Marine Research*[1]. A small subset of results stem from my Master's Thesis[2]; these results have also been published in Hirschi et al. (2003)[3].

Chapter 3 focuses on the more technical aspects of observing system design. In addition to the intuition-based array design applied in chapter 2, two different optimization techniques are applied to the proposed MOC observing array at 26°N, and 53°N. This chapter is in preparation for publication as a note in *Journal of Atmospheric and Oceanic Technology*[4].

In chapter 4, I first test whether the proposed MOC monitoring array at 26°N is able to capture long-term MOC changes in three simulations of the IPCC (Intergovernmental Panel on Climate Change) scenario A1B in a coupled climate model. Second, a statistically rigorous method for the detection of MOC changes is introduced including different magnitudes of observation error. Third, I test how long it would take to detect MOC changes when relying on array measurements versus repeated hydrographic transects. This chapter is in press with *Climatic Change*[5].

[1] Baehr, J., J. Hirschi, J.-O. Beismann, J. Marotzke (2004): Monitoring the meridional overturning circulation in the North Atlantic: A model-based array design study, *Journal of Marine Research*, **62 (3)**, 283-312.

[2] Baehr J., Monitoring meridional transports at 26°N in the Atlantic: A model-based design study, School of Ocean and Earth Science, Southampton (UK), 2002, 51pp.

[3] Hirschi, J., J. Baehr, J. Marotzke, J. Stark, S. Cunningham, J.-O. Beismann (2003): A monitoring design for the Atlantic meridional overturning circulation, *Geophysical Research Letters*, **30 (7)**, 1413, doi: 10.1029/2002GL016776.

[4] Baehr J., D. McInerney, K. Keller, J. Marotzke (2006): Optimizing a model-based observing system design for the North Atlantic meridional overturning circulation, in preparation.

[5] Baehr, J., K. Keller, J. Marotzke (2006): Detecting potential changes in the meridional overturning circulation at 26°N in the Atlantic, *Climatic Change*, in press.

Chapter 5 develops a multivariate detection method. The method is subsequently applied to simulated observations (in simulations of the scenario A1B) derived from the proposed MOC monitoring array at 26°N, and to the existing transport estimates based on hydrographic transects (Bryden et al., 2005). This chapter has been submitted to *Journal of Climate*[6].

In chapter 6 overall conclusions are presented, and possible future research directions are discussed.

[6] Baehr, J., H. Haak, S. Alderson, S. A. Cunningham, J. H. Jungclaus, J. Marotzke (2006): Timely detection of changes in the meridional overturning circulation at 26°N in the Atlantic, *Journal of Climate*, submitted.

2. MONITORING THE MOC IN THE NORTH ATLANTIC[1]

Abstract
A monitoring system for the meridional overturning circulation (MOC) is deployed into an 'eddy-permitting' numerical model (FLAME) at three different latitudes in the North Atlantic Ocean. The MOC is estimated by adding contributions related to Ekman transports to those associated with the zonally integrated vertical velocity shear. Ekman transports are inferred from surface wind stress, whereas the velocity shear is derived from continuous density 'observations', principally near the eastern and western boundaries, employing thermal wind balance. The objective is to test the method and array setups for possible real observation in the ocean at the chosen latitudes and to guide similar tests at different latitudes.

Different 'mooring placements' are tested, ranging from a minimal setup to the theoretical maximum number of 'measurements'. A relatively small number of vertical density profiles (about 10, the exact number depending on the latitude) can achieve a reconstruction of the MOC similar to one achieved by any larger number of profiles. However, the main characteristics of the MOC can only be reproduced at latitudes where bottom velocities are small, here at 26°N and 36°N. For high bottom velocities, in FLAME at 53°N, the array fails to reproduce the strength and variability of the MOC, because the depth-averaged flow cannot be reconstructed accurately. In FLAME, knowledge of the complete bottom velocity field could substitute for the knowledge of the depth-averaged velocity field.

[1] Baehr, J., J. Hirschi, J.-O. Beismann, J. Marotzke (2004): Monitoring the meridional overturning circulation in the North Atlantic: A model-based array design study,*Journal of Marine Research*, **62 (3)**, 283-312.

2.1 Introduction

The meridional overturning circulation (MOC) carries most of the oceanic heat transport in the Atlantic (Hall and Bryden, 1982). The effect of this northward heat transport of about 1 PW ($= 10^{15}$ W) is seen in the resulting relatively mild climate of Western Europe (Ganachaud and Wunsch, 2000). In the Atlantic the MOC comprises both a (dominating) buoyancy forced contribution, i.e. the thermohaline circulation (THC), and wind-driven meridional transports.

Although the mid-latitude MOC appears to be relatively steady over the last few decades (Macdonald and Wunsch, 1996), palaeoclimatic records suggest that the ocean circulation has undergone rapid changes in the past 120,000 years, since the Eemian interglacial period (Heinrich, 1988; Dansgaard et al., 1993; National Research Council, 2002; Alley et al., 2003). These abrupt changes corresponded to significant variations in temperature and climate over the North Atlantic and its adjacent regions. Changes in the Atlantic MOC are eminently associated with the proposed mechanisms of such abrupt climate change (Marotzke, 2000). A weakening or collapse of the Atlantic MOC might entail a reduction in the North Atlantic heat transport, which in turn would corresponded to significant variations in temperature and climate over the North Atlantic and its adjacent regions. The suggested mechanisms are of concern for both past and future changes. Predicting if a conceivable rapid change in the MOC is impending, is as important as detecting such an ongoing change.

Currently, ship based transoceanic sections yield the most reliable estimates of the MOC, but provide only snapshots of the MOC and the related meridional transports, e.g. Hall and Bryden (1982); Ganachaud and Wunsch (2000). Repeated hydrographic sections might allow decadal changes in the MOC to be detected (Keller et al., 2006a), but they are too expensive and personnel intensive to ensure a continuous observation of the MOC.

An alternative monitoring strategy, which is more cost-effective than ship-borne measurements, was suggested by Marotzke et al. (1999). Their conceptual starting point is the thermal wind relationship, which links density differences to the zonally averaged meridional flow. Marotzke (1997) and Marotzke and Klinger (2000) based a theory of a purely buoyancy-driven MOC on the ability to express the meridional streamfunction as a function of latitude and density difference between eastern and western sidewalls (and other, independent, parameters). In principle, only the systematic observation of density at eastern and western sidewalls would be required to monitor the MOC continuously (Marotzke et al., 1999).

Thus, Marotzke et al. (2002) suggested the implementation of a mooring array for continuous density observation to monitor the MOC at 26°N. The design of the observing array was tested in two eddy-permitting numerical ocean models (Hirschi et al., 2003), estimating the MOC from zonal density differences and wind information only. However, 26°N is unique in its geographical setup: the circulation is separated into a geographically detached western boundary current (in the Florida Strait), a confined western boundary current (the Antilles Current) and a basin-wide return flow. This study therefore aims to establish how generally valid the configuration at 26°N is and if this approach could be applied to other - less special - latitudes in the North Atlantic.

In the present study (as in Hirschi et al., 2003), the monitoring array is 'deployed' into a numerical model assuming that the implementation of the real field experiment could be improved considerably by 'monitoring' the MOC in a model. Efficient experiment design (or more specifically array design) has been argued to play a key role in obtaining the maximum information from available resources (McIntosh, 1987; Barth and Wunsch, 1990), since oceanographic measurements are costly and difficult to obtain. Simulating the performance of observing arrays in numerical models has been conducted based on two different intentions: A variety of design studies were performed to optimize a monitoring strategy, whereas other work addressed the fundamental principles of observing system design. Both types of array design studies can be classified based on the chosen criterion to measure the capability of the particular array (Hackert et al., 1998):

(i) The most intuitive approach might be to employ statistical techniques, e.g. error estimates, as a measure of the capability of the array: Bretherton et al. (1976) used the objective mapping approach - widely used in meteorology - to design a current meter array for the MODE program (Mid-Ocean Dynamics Experiment). Barth and Wunsch (1990) analyzed the design of acoustic tomographic arrays using simulated annealing for an idealized (two-dimensional) case. Drifter launch strategies, i.e. involving advection of the observing sites, based on Lagrangian templates were investigated by Poje et al. (2002), who aimed to establish a criterion requiring a minimal amount of a-priori information. Guinehut et al. (2002) applied the objective mapping approach to design an array of profiling floats in the North Atlantic, comparing Eulerian and Lagrangian arrays.

(*ii*) Alternatively, data assimilation techniques were used to quantify the information content of an array (McIntosh, 1987). Bennett (1985) used the variational inverse method of Bennett and McIntosh (1982) to assess the efficiency of arrays comprising pressure transducers and acoustic tomography units. Hackert et al. (1998) used a data assimilation scheme to optimize the location of a limited number of moorings for the proposed Pilot Research Moored Array in the Tropical Atlantic (PIRATA).

(*iii*) Sensitivity studies of a model can be used to derive a statement about the best observational strategy: Schröter and Wunsch (1986) calculated the sensitivity of their objective function to changes in the data; mapping the values of the used set of Lagrange multipliers allowed them to determine the regions of greatest sensitivity of the objective function to particular measurement types. Harrison et al. (1989) conducted a similar sensitivity study for the tropical Pacific Ocean. Although not specifically aligned to observing system design, this study was - together with Harrison (1989) - crucial in identifying the latitudinal extent of the Tropical-Atmosphere-Ocean (TAO) array wind measurements. Recently, adjoint sensitivity studies have been used to identify regions where (additional) observations should take place, explicitly not confined to near-surface observations and hydrographic sections only. Marotzke et al. (1999) studied adjoint sensitivities of the oceanic heat transport to dynamically link hydrographic measurements and heat transport estimates. Köhl and Stammer (2004) conducted an adjoint sensitivity study to determine an optimal observing array to monitor transport changes across the Greenland-Scotland ridge.

All the studies mentioned above regard array design as an optimization problem either by optimizing the array itself or by taking a general view towards the underlying principles of array design. Generally, model-based pre-deployment array design does not seem to have been used widely. A notable exception is Hackert et al. (1998), who conducted a series of observing system simulations, testing the ability of the respective sample array to resemble actual TOPEX/Poseidon data. In contrast, the present study seeks to test a monitoring strategy, primarily aiming to provide immediate support for a realizable observational campaign. Hirschi et al. (2003) provided support for an MOC monitoring strategy at 26°N. Here, we investigate whether other less geographically special latitudes are suitable for a similar strategy. For this, we analyze in detail the force balance of the MOC, and how it varies with latitude and geometry.

This paper is organized as follows. Section 2 provides a description of the employed method, and the numerical model used. The array design for the different latitudes, the results from different array setups and an analysis of the weaknesses of the

monitoring arrays are found in section 3. The ability of the array to estimate the heat transport variability is tested in section 4. Section 5 contains a discussion, and conclusions follow in section 6.

2.2 Method and Model

2.2.1 Method

The approach applied here is the same as used by Hirschi et al. (2003) and Hirschi and Marotzke (2006), who employed Lee and Marotzke's (1998) decomposition of the meridional velocity field. The MOC is described as the sum of contributions originating from two measurable quantities: the zonal density difference and the surface wind stress. Thermal wind balance is assumed to hold everywhere. For a rectangular basin, i.e. zonally uniform topography and vertical sidewalls, the zonal integration of thermal wind leads to

$$L_x \overline{\frac{\partial v(x,y,z)}{\partial z}} = -\frac{g}{\rho_0 f}\left(\rho(x_W,y,z) - \rho(x_E,y,z)\right), \tag{2.1}$$

where L_x is the zonal extent of the rectangular basin, $\rho(x_W,y,z)$ and $\rho(x_E,y,z)$ are the densities at the eastern and western sidewalls, respectively, and the overbar indicates the zonal average (Marotzke et al., 1999). Further, v is the meridional velocity, g the acceleration due to gravity, f the Coriolis parameter and ρ_0 a reference density. Under realistic circumstances, in particular in the presence of irregular topography, we expect that a number of density profiles is required, denoted n=1,2,...,N. Vertical integration of equation (2.1) yields an expression for the meridional velocity field between the two vertical profiles n and $n+1$ at a zonal distance $L(y,0)_{n+1} - L(y,0)_n$. A depth-dependent meridional velocity field $v_{g_n}(x,y,z)$ is defined as

$$v_{g_n}(x,y,z) = \begin{cases} -\frac{g}{\rho_0 f}\left[\int_{-D_{min}}^{z}\left(\frac{\rho(x_{n+1},y,z)-\rho(x_n,y,z)}{L(y,0)_{n+1}-L(y,0)_n}\right)dz\right] & \text{for } -D_{min} \le z < 0 \\ & \text{and } x_n \le x \le x_{n+1}, \\ 0 & \text{for } -D(x,y) \le z < -D_{min} \\ & \text{and } x_n \le x \le x_{n+1}, \\ 0 & \text{for } x < x_n \text{ or } x > x_{n+1}. \end{cases} \tag{2.2}$$

Here, $D(x,y)$ denotes a depth profile along the zonal section, and D_{min} is the minimum depth found between the two profiles (in the interval $x_n \le x \le x_{n+1}$). Figure 2.1 depicts the example for $N = 2$, the shaded square indicates, where thermal wind

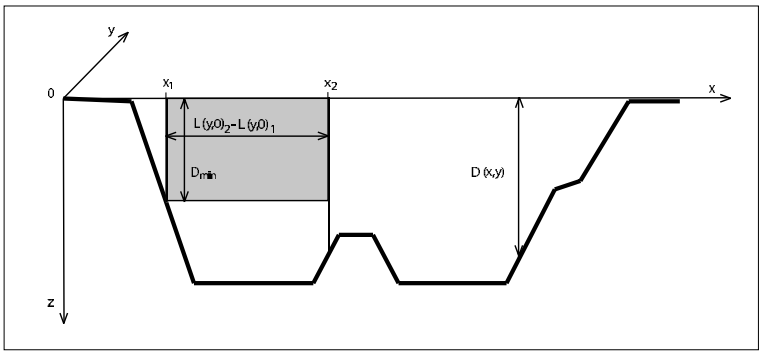

Fig. 2.1: Schematic of a zonal transect with two profiles ($n = 1$ and $n = 2$) at the locations x_1 and x_2, respectively. The distance between the two profiles is $L(y,0)_2 - L(y,0)_1$. $D(x,y)$ denotes a depth profile along the section. The shaded square indicates where thermal wind (according to equation 2.2) is described by the two profiles. The velocities outside this area are initially set to zero.

(equation 2.2) is described by the two profiles. Generally, equation (2.2) describes thermal wind in the area between the profiles n and $n+1$, with zero velocity everywhere else within the zonal transect. In the presence of zonally non-uniform topography, bottom triangles occur when the maximum depth of the area between the two profiles is larger than the maximum depth common to both profiles, or the minimum depth of the area between the two profiles is smaller than the maximum depth common to both profiles. Initially, the velocity is set to zero at depths greater than D_{min} and at longitudes smaller than $L(y,0)_n$ or larger than $L(y,0)_{n+1}$. A level of no motion is assumed to be at the bottom of the ocean. For an ocean basin covered by N vertical density profiles, the complete meridional velocity field is then the sum of the velocity fields between two adjacent profiles:

$$v_g(x,y,z) = \sum_{n=1}^{N-1} v_{g_n}(x,y,z). \tag{2.3}$$

Further zonal and vertical integration gives the density-driven contribution of the overturning streamfunction (Marotzke, 1997), which exists if no mass enters or leaves through the boundaries. To ensure zero net meridional mass transport, without distorting the local velocity shear, a spatially (but not temporally) constant correction is applied first (Hall and Bryden, 1982), yielding a corrected meridional velocity field $v_{g_{corr}}(x,y,z)$:

$$v_{g_{corr}}(x,y,z) = v_g(x,y,z) - \frac{\int_{-D(x,y)}^{0} \int_{0}^{L(y,z)} v_g(x,y,z)dxdz}{A}, \tag{2.4}$$

where A is the area of the cross-section. The resulting corrected meridional velocity field maintains mass balance and can thus be integrated vertically and zonally to yield the density-driven meridional overturning streamfunction as a function of latitude and depth.

The wind-driven part of the MOC can be calculated based on the Ekman volume transport,

$$v_{ek}(x,y,z) = -\frac{1}{\rho_0 f A_d}\int_0^{L(y,0)} \tau(x,y)dx, \tag{2.5}$$

where $\tau(x,y)$ is the x-component of the wind stress, assuming an Ekman depth d (covering the zonal area A_d) to which the Ekman transport is confined. Typically, d is 50-100 m, e.g. Chereskin et al. (1997). To ensure no net meridional mass transport related to the zonal wind stress, the flow through the Ekman layer is compensated by a depth-uniform return flow (Jayne and Marotzke, 2001). The corrected velocity field reads as follows:

$$v_{ek_{corr}(x,y,z)} = \begin{cases} v_{ek} - \frac{v_{ek}A_d}{A} & \text{for } -d \geq z \\ -\frac{v_{ek}A_d}{A} & \text{for } -d < z \end{cases}, \tag{2.6}$$

where A is the area of the zonal transect. Integrating the corrected Ekman velocities yields an overturning contribution, which is zero at the surface and at the bottom of the ocean, and has its maximum transport at the Ekman depth. Note that the zonal wind stress also generates a depth-dependent geostrophic flow as it affects the density gradients (McCreary and Lu, 1994), which is included in the reconstruction based on the density profiles.

The reconstructed overturning is the sum of the density- and wind-driven components based on the corrected velocities $v_{g_{corr}}(x,y,z)$ and $v_{ek_{corr}}(x,y,z)$ given in equations (2.4) and (2.6), respectively:

$$\Psi(y,z) = \int_{-D(x,y)}^{z}\int_0^{L(y,z)} v_{g_{corr}}(x,y,z)dxdz + \int_{-D(x,y)}^{z}\int_0^{L(y,z)} v_{ek_{corr}}(x,y,z)dxdz. \tag{2.7}$$

This MOC reconstruction could be based on real measurements, where $v_g(x,y,z)$ could be obtained from vertical density measurements (e.g. an array of full depth moorings measuring temperature and salinity) and $v_{ek}(x,y,z)$ could be obtained from satellites measuring near-surface wind speed and direction. Both $v_g(x,y,z)$

and $v_{ek}(x, y, z)$ need to be corrected to maintain mass balance (as described in equations (2.4) and (2.6)). Note that this MOC reconstruction is identical to a reconstruction in which the wind and the density velocity fields would be added prior to the correction ensuring mass balance. Correcting the two contributions separately greatly aids in their interpretation.

2.2.2 The FLAME Model

The model output used in this study stems from the 1/3° Atlantic Model of the FLAME group, a hierarchy of Atlantic Ocean models (Dengg et al., 1999; Beismann and Redler, 2003). The code is based on a refined configuration of the Geophysical Fluid Dynamics Laboratory's (GFDL) MOM, version 2.1 (Pacanowski, 1995). The model is so-called 'eddy-permitting', meaning that the horizontal grid resolution is high enough to allow the formation of oceanic eddies, without however properly resolving the deformation radius at all latitudes. The model domain extends from 70°S to 70°N, and from 100°W to 30°E. It has open boundaries across the Antarctic Circumpolar Current in the Drake Passage and south of Africa at 30°E. The northern boundary is closed with a restoring zone at 70°N. FLAME has a realistic bottom topography, and a rigid lid condition is applied at the surface. The horizontal resolution is 1/3° in longitude and 1/3° $\times \cos(\phi)$ in latitude (ϕ), similar to the DYNAMO intercomparison study (Willebrand et al., 2001). FLAME's deep water formation and meridional overturning are enhanced due to the implementation of a higher vertical resolution (45 non-equidistant levels), together with the adaptation of a bottom boundary layer scheme (Beckmann and Döscher, 1997) and lateral subgrid scale mixing along isopycnals (Redi, 1982; Cox, 1987).

The model integration starts at 01 January 1900. The atmospheric forcing is based on the ECMWF (European Centre for Medium Range Weather Forecast) re-analysis (Barnier et al., 1995) monthly means, but has superimposed wind and heat flux anomalies from NCEP-NCAR (National Centers for Environmental Prediction/ National Center for Atmospheric Research) re-analyses products (Kalnay et al., 1996) for the period from 1958 to 2001. This superposition of forcing components has been described in detail in Eden and Willebrand (2001). For the freshwater fluxes sea surface salinity is restored to a combination of the climatological values of Levitus et al. (1994) and Boyer and Levitus (1997) (see Beismann and Redler (2003) for details). For the analysis conducted here, the model output used starts at 01 January 1980 and has a total length of 20 years.

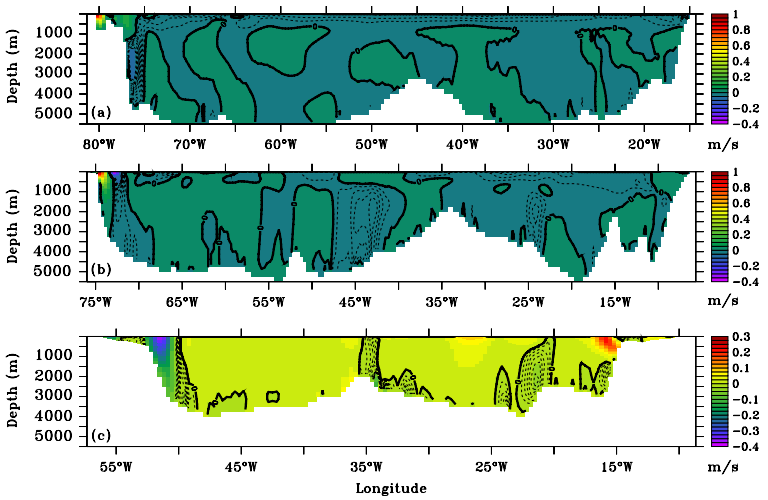

Fig. 2.2: Time mean meridional velocity field from FLAME for (a) 26°N, (b) 36°N and (c) 53°N (20 yr average). Note that the color scale is linear, but the contour lines are only plotted for velocities between -0.05 and 0.00 ms^{-1} (in intervals of 0.01 ms^{-1}) for all latitudes to enhance the visibility of the southward meridional velocities.

2.2.3 Data Set

A subset of three different latitudes is chosen from FLAME: 26°N, 36°N, and 53°N. The starting point is 26°N as used by Hirschi et al. (2003). The two additional latitudes are chosen to test if the employed method is reliable at places with a less special geographical and dynamical setup than 26°N. Hence, 36°N represents a subtropical latitude as does 26°N, with the significant difference that the western boundary current is no longer geographically confined to a shallow strait. As 36°N was subject to observations, e.g. Roemmich and Wunsch (1985), a comparison of model and data is possible. The latitude of 53°N, in contrast, is situated at the boundary to the subpolar gyre and exhibits much weaker stratification than the two subtropical latitudes. It was observed by different hydrographic sections Dobrolyubov et al. (2002); Talley (2003), but more important its western boundary was recently subject to intense observations (Fischer et al., 2003). This allows - together with an analysis of the dynamics of the subpolar gyre in FLAME (Scheinert, 2003) - a comparison of the model and the observed meridional velocity field. The geographical setup of the three latitudes (and the whole North Atlantic) is similar in that the Mid Atlantic Ridge (MAR) divides the basin. However, there are pronounced differences regarding the steepness of the slopes at the margins and the absolute depth of the basin at the specific latitude.

Figure 2.2 shows the topography and the time-mean meridional velocity field for the three different latitudes. All three sections exhibit a strong surface western boundary current, albeit differing in their vertical structures and their narrowness and mean flow direction. Note that at 36°N FLAME does exhibit a strong northward western boundary current, but the deep southward flow is not found at the western boundary (here, strong southward velocities are found at the surface). Instead, the highest deep southward meridional velocities occur along the western slope of the MAR (cf. figure 2.2). The section by Roemmich and Wunsch (1985), in contrast, suggests a western boundary current situated beneath the northward surface current with maximum velocities of 0.5 cm s^{-1}.

For all three investigated latitudes the basin is, apart from the boundaries, dominated by the return flow, which differs considerably between the latitudes in its (local) strength. The maximum overturning is 16 Sv at 26°N, 17 Sv at 36°N, and 14 Sv at 53°N. In FLAME the maximum overturning of about 18 Sv is found at 40°N at a depth of about 1000 m, which is largely in accordance with observations (Macdonald, 1998; Ganachaud and Wunsch, 2002). The mean Ekman transport is positive, i.e. northward, for 26°N (2 Sv), but negative for 36°N (-2 Sv) and 53°N (-3 Sv).

Time mean values of the meridional heat transport in FLAME are slightly lower than observations at the two subtropical latitudes. The 26°N value of 0.9 PW is notably smaller than the 1.2 PW estimate of Hall and Bryden (1982), Roemmich and Wunsch (1985) and Lavin et al. (1998) and the 1.3 PW estimate by Ganachaud and Wunsch (2000) and Talley (2003). The 36°N value of 0.8 PW is similar to the estimate by Roemmich and Wunsch (1985) and Talley (2003), but considerably smaller than the estimate of 1.2 PW by Sato and Rossby (2000). The 53°N value of 0.65 PW agrees with the 0.62 PW estimate of Talley (2003), which is based on a 1962 hydrographic section. The seasonal variability of the meridional heat transport is, however, in close agreement to the expectations (Böning et al., 2001). Generally, FLAME's meridional transports and their variability in the North Atlantic are - with all its inevitable limitations - comparable to observations (Willebrand et al., 2001; Böning et al., 2001).

2.3 Results

The MOC is reconstructed based on density differences and the surface wind stress, as described in section 2.2.1. The starting point is the array setup for 26°N as it was used by Hirschi et al. (2003). For the two additional latitudes, comparable array setups are investigated, adapting a (financially) feasible number of 'moorings' only. As in Hirschi et al. (2003) the criteria for the placement of these density profiles are a combination of experience and qualitative application of some sampling theorems: the profiles need to be placed particularly in areas of high meridional velocities, but the resulting array needs to cover as much of the basin area as possible in order to minimize remaining bottom triangles. The latter criterion is based on the assumption that the vertical structure of the MOC can only be reconstructed when the basinwide (weak) return flow is captured, too. Hence, this 'mooring' placement does rely on prior knowledge about the 'distribution' of the quantity (in this case the meridional velocity field) taken from the numerical model.

Thus, the placement of the profiles is initially based on physical intuition only. Similarly, most other studies rely on the trial-and-error adjustment of array configurations (Bretherton et al., 1976), sometimes stating that it is 'clearly impossible to test every possible array' (McIntosh, 1987); two notable exceptions are Barth and Wunsch (1990) and Barth (1992) who analyzed idealized cases. Here, no systematic attempt is made to optimize the 'mooring' placement. Rather, we want to demonstrate that our chosen design captures the quantity of interest, the MOC. However, the intuition-based array is later justified with a technical array design study.

2.3.1 The Standard Observing Array

A basic array is now designed; as argued before, we cannot currently optimize it rigorously. Instead, we follow the two physical criteria described above and the practical requirement of financial feasibility if the design is implemented. The westernmost part of the basin exhibits a strong western boundary current, hence the western margin of the basin needs dense coverage, which was initially set to four profiles: the first one covering the shallow part of the current, the second one located in the centre of the boundary current, the third one placed at the edge of the time-mean current and the fourth one just outside the western boundary current. Apart from the western margin the rest of the basin is dominated by the return flow; the eastern part of the basin is hence initially covered with three profiles, placed along the slope. To account for pressure differences on both sides of the MAR, two more profiles are placed on the eastern and western slope of the ridge. The basic array

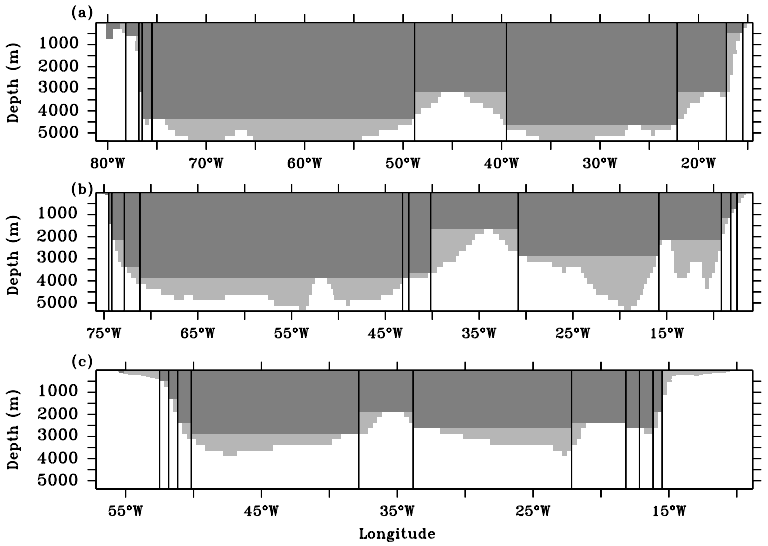

Fig. 2.3: Placement of profiles for the standard array: (a) 26°N, (b) 36°N and (c) 53°N.

consists of nine profiles, placed across the transect with higher coverage at the margins.

Taking into account the specific dynamical and geographical setup of each latitude this basic array is modified for each of the considered latitudes (26°N, 36°N and 53°N in the North Atlantic), to set up a standard array for each individual latitude. Figure 2.3 shows the placement of the profiles on each transect. The basic array as well as its local modifications are summarized in table 2.1.

At 26°N the western boundary current is geographically confined to the Florida Strait. In the real world this latitude is comparatively well-investigated as it is close to the latitude of four modern hydrographic sections (1957, 1981, 1992, 1998; cf. McTaggert et al. (1999) and e.g. Koltermann et al. (1999)). Furthermore, it offers a unique long-term timeseries of western boundary current observations as the mass transport across the Florida Strait has been monitored by cable measurements for

Tab. 2.1: Basic array and its modifications for the individual latitudes.

	W Boundary	**MAR**	**E Boundary**	**Total No. of Profiles**
26°N	4 + Florida Strait	2	3	9 + Florida Strait
36°N	4	2 + 2	3 + 1	12
53°N	4	2	3 + 2	11

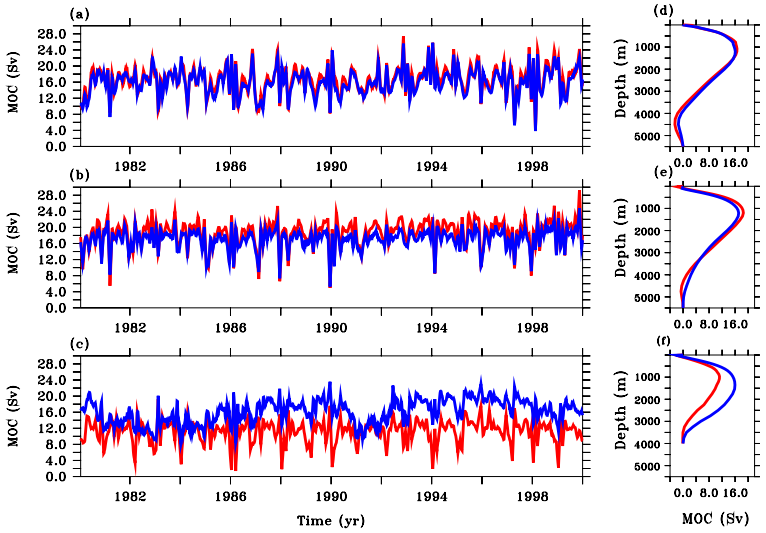

Fig. 2.4: MOC (red) and estimated transport (blue) on the basis of the standard arrays. The estimated transport is the sum of the thermal wind and Ekman contributions. Timeseries of the maximum transports are shown in figures (a) - (c), and a time mean vertical profile in figures (d) - (f); 26°N: (a) and (d), 36°N (b) and (e), 53°N: (c) and (f).

over 20 years (Larsen, 1985; Baringer and Larsen, 2001). To account for this, the basic array is extended by assuming the total mass transport at the longitudes of the Florida Strait to be known at all times. The velocity pattern is updated every three months; inaccuracies in the cable measurements are mimicked by added noise of 1 Sv standard deviation. This setup is identical to the one used in Hirschi et al. (2003).

Further north the western boundary current is no longer geographically confined. At 36°N a strong surface northward boundary current can be found at the western boundary in FLAME, but the deep southward flow (as pointed out in section 2.2.3) is found at the slope of the MAR. Whereas observations show a deep southward flow at the western boundary underneath the northward surface current (Roemmich and Wunsch, 1985), a similar velocity distribution as in FLAME has resulted from a CO_2 increase in a coupled GCM (Wood et al., 1999). Therefore such a distribution needs to be covered by the method (assuming prior knowledge of the velocity information for the placement of the profiles). Hence, the basic array for 36°N is extended by two profiles covering the deep southward flow along the western slope of the MAR. Secondly, the array is enhanced by one additional profile at the eastern margin to ensure coverage of the high velocities over the relatively gentle slope. Thus, the standard array for 36°N consists of 12 profiles, three profiles more than the basic array at 26°N.

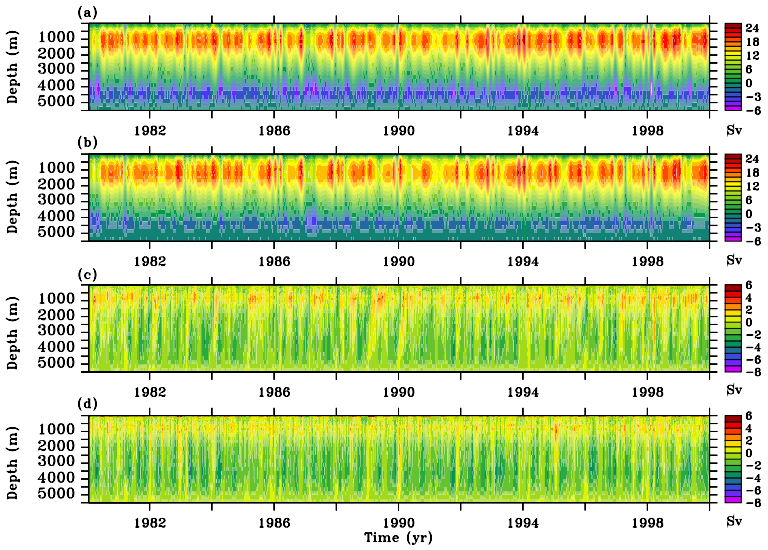

Fig. 2.5: Timeseries for 26°N: (a) MOC, (b) reconstruction based on the standard array, (c) MOC minus reconstruction based on the standard array, (d) MOC minus reconstruction based on a profile at every zonal grid cell. Note that the color scale in panel (a) and (b) is finer for negative transports.

The third and northernmost latitude, 53°N, does not show a northward western boundary current, but currents are stronger at the eastern and western boundary than in the rest of the basin. Furthermore, the eastern slope is relatively gentle, so the basic setup of three profiles is not sufficient to cover the strong currents here. The basic array is supplemented with two extra profiles.

The MOC is reconstructed based on the 'standard arrays' for the different latitudes, where the density is 'measured' at the locations of the profiles; knowledge about the surface wind stress is assumed for the zonal transect. Figure 2.4 shows the MOC calculated from the model velocities and the MOC reconstruction based on the standard arrays. It shows that for 26°N and 36°N, the mean value of the maximum overturning and its strong temporal variability are largely captured. For 36°N the mean value is underestimated by about 1 Sv; the variability of the reconstruction is slightly too weak (by about 3 Sv for the maximum amplitudes). The time-mean vertical profile reveals that for both latitudes the deep return flow is underestimated. For 53°N the quality of the reconstruction of the maximum varies with time: whereas in some years the mean value of the maximum is met precisely, the overturning is overestimated at most times. The time-mean vertical structure indicates that the maximum MOC is not reproduced in its magnitude nor in its position within the water column.

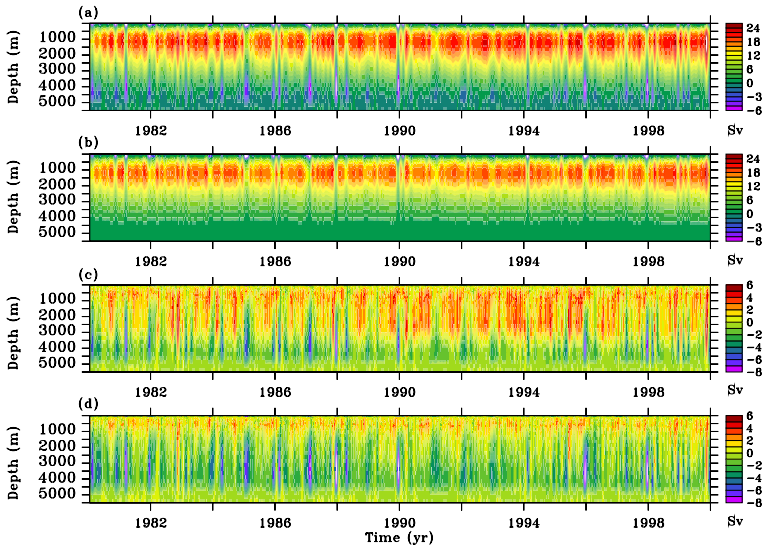

Fig. 2.6: Timeseries for 36°N: (a) MOC, (b) reconstruction based on the standard array, (c) MOC minus reconstruction based on the standard array, (d) MOC minus reconstruction based on a profile at every zonal grid cell. Note that the colour scale in panel (a) and (b) is finer for negative transports.

2.3.2 MOC Reconstruction based on the Standard Array

A more detailed picture is provided using Hovmoeller diagrams as they show the evolution of the full-depth overturning over time, rather than the time-mean vertical profiles (as in figure 2.4). Figures 2.5 (26°N), 2.6 (36°N) and 2.7 (53°N) show the model overturning (panel a) and its reconstruction based on the respective standard array (panel b). For the two subtropical latitudes the overturning is captured both in its temporally varying magnitude and its vertical extent. Temporal mis-estimates occur in the upper 3000 m (cf., panel c, figures 2.5 and 2.6), but the reconstruction of the deep southward flow is generally too weak by about 1.5 Sverdrups. At 53°N, in contrast, the overturning is overestimated. The structure of the deep southward flow is not captured, which might be pre-dominantly due to the overestimate of the maximum, since the model shows no distinctive deep southward current at 53°N. Overall, the MOC reconstruction based on the standard array follows the original MOC closely for 26°N and 36°N, whereas larger - temporally variable - differences occur at 53°N (about 1/3 of the total strength of the MOC there). Note that the reconstruction appears to be robust to small zonal variations in the placement of the standard array profiles, e.g. one or two grid cells.

The errors in the reconstruction could originate from the sparse resolution of the profiles or from conceptual limits of the method, or both. To analyze this, the

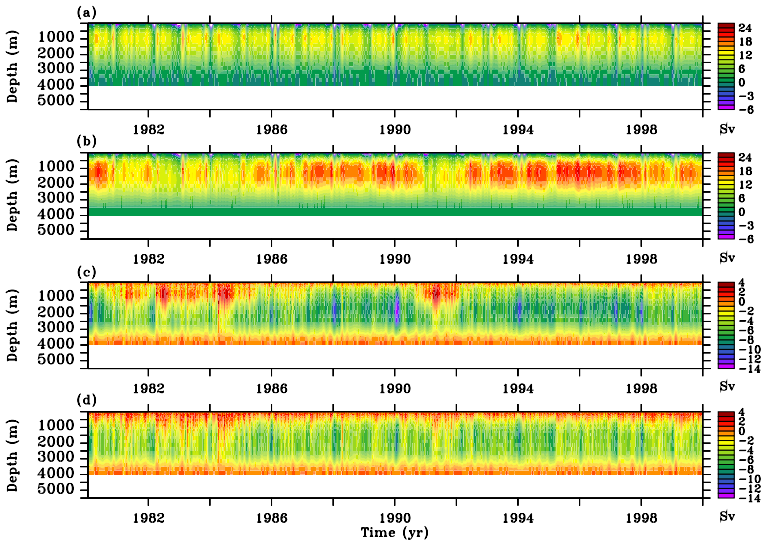

Fig. 2.7: Timeseries for 53°N: (a) MOC, (b) reconstruction based on the standard array, (c) MOC minus reconstruction based on the standard array, (d) MOC minus reconstruction based on a profile at every zonal grid cell. Note that the colour scale in panel (a) and (b) is finer for negative transports.

MOC is reconstructed based on the maximum amount of available information. In figures 2.5, 2.6 and 2.7 (panel d) the Hovmoeller diagrams for the differences between original and reconstruction are shown, relying on the (theoretical) maximum amount of measurements, i.e. a full-depth 'mooring' at every zonal non-land grid point. Comparing the reconstruction of the standard array and the one relying on maximum amount of density information shows that the quality of the reconstruction in the upper part of the water column improves for all latitudes, most notably for 53°N where the bias in the reconstruction is now nearly temporally constant (about 4 Sv). In all cases, the underestimate of the deep return flow is not due to the sparse basin-coverage of the array. Hence, both sources of errors are investigated: first, variations in the number of profiles and second, the dynamical limits of the method are analyzed.

2.3.3 Variations in the Number of Profiles

The robustness of the placement of the profiles employed in the standard array is tested, analyzing the results using fewer and larger numbers of profiles. Figure 2.8 summarizes the different setups and their respective results. The robustness of the placement of the profiles employed in the standard array is tested, analyzing the results using fewer and larger numbers of profiles. Figure 2.8 summarizes the different setups and their respective results. The number on top of the profile indicates its rank order in the setup, starting from a simple setup of two profiles, one each at

the eastern and western boundaries. Then, profile number 3 is added, then 4 and so on. The very last point represents the result using all available model density information. The quality of the reconstruction is quantified in terms of the correlation coefficient, the rms error of the timeseries of the maximum and the rms error of the time-mean vertical profile.

For 26°N the correlation coefficient shows little dependence on the number of profiles used. The reconstructed density-driven contribution does not vary with periods longer than about a year, but its absolute value is sensitive to the number of profiles used. Thus, the correlation coefficient is dominated by the short-term variability of the reconstruction, i.e., the estimated wind-driven contribution, which itself is independent of the number of density profiles used. The rms error is small as well, with the exception at five profiles, where the three profiles at the western margin cover the strength of the deep southward flow, but not yet (as with six profiles) the northward flow in its total strength. This is mirrored in the rms error of the vertical profile, which decreases strongly until six profiles are used and is saturated when nine profiles are placed.

36°N exhibits generally similar characteristics: The correlation coefficient does not vary significantly between the different setups, whereas the rms error for both the timeseries of the maximum and the time-mean vertical profile shows sensitivity to the different setups. Most distinctive is the decrease in the quality of the reconstruction (measured by the rms error) between 8 and 11 profiles, which is due to the combination of the underestimate of both the deep southward flow (on the western slope of the MAR) and the eastern boundary current. The rms errors are not constant until the array covers both the MAR and the shallow eastern slope (with a total of 12 profiles then).

In contrast to the two other latitudes, the correlation coefficient at 53°N is sensitive to the number of profiles used. The low-frequency part (with periods longer than about a year) of the thermal wind contribution varies with time, and the estimated variability of the thermal wind contribution varies with the number of profiles used. Note that the overturning itself has a temporally constant low-frequency contribution. For a rudimentary array of seven profiles or fewer the correlation coefficient of about 0.55 is due to a temporally non-varying estimate of the thermal wind contribution (and a correct estimate of the wind contribution). With 7 to 10 profiles the low-frequency part of the thermal wind is at certain times estimated correctly, whereas at others the reconstructions fail by as much as 10 Sv. Hence, the correlation coefficient is smaller than with a fewer number of profiles and the rms error is

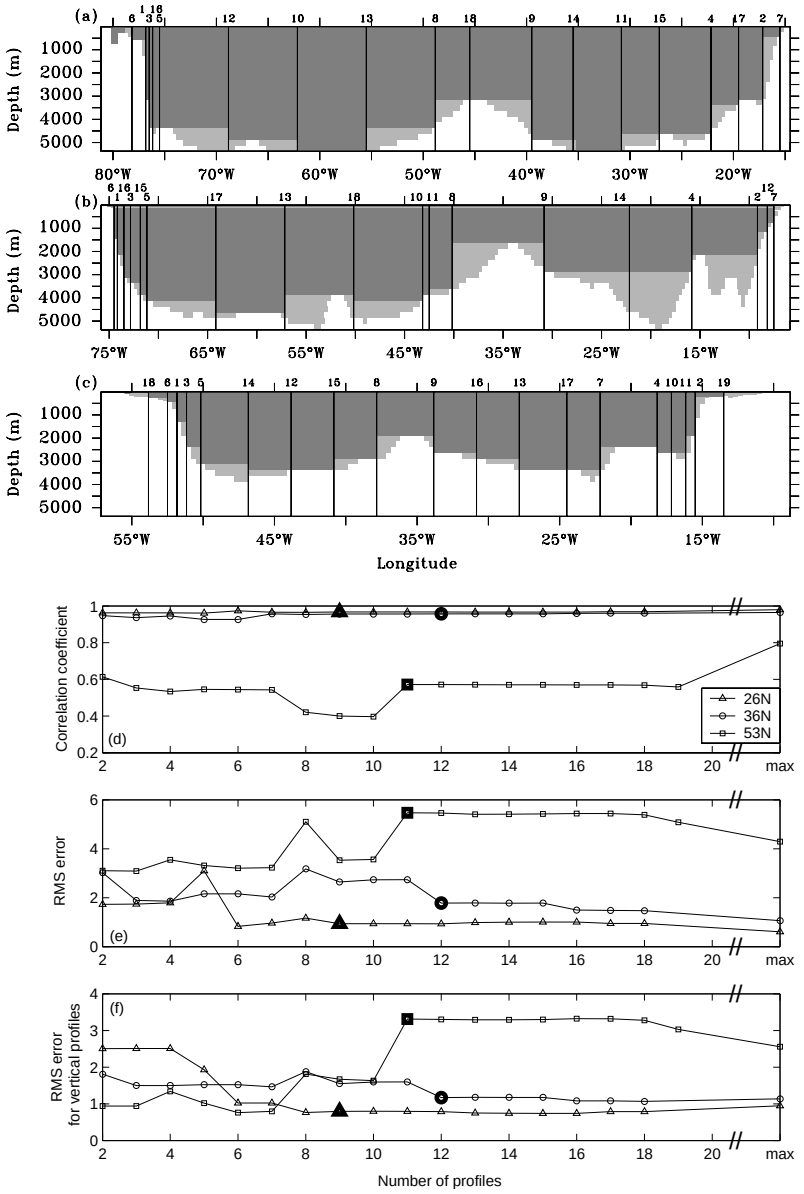

Fig. 2.8: Top: Placement of profiles, (a) 26°N, (b) 36°N and (c) 53°N. The number on top of the profile indicates its rank order in the setup. The standard setup (indicated by a bold marker) is derived from a simple setup of two profiles, adding first another profile each at the western and eastern boundary. Second, coverage at the western margin is intensified by two profiles; third, the two MAR profiles are included, and a (shallow) eastern profile plus the individual modifications for the latitudes complete the standard array setup. Additional profiles are placed in the middle of the remaining gaps (up to 18 profiles in total). Bottom: (d) correlation coefficient, (e) rms error for the timeseries of the maximum MOC, and (f) rms error for time-mean vertical profile based on different setups. The very last point represents the maximum amount of profiles, i.e. using all available model density information, which is 196 profiles for 26°N, 208 profiles for 36°N and 139 profiles for 53°N, respectively.

larger (for both the timeseries of the maximum and the vertical profile). Note that the reconstruction using all model information has a higher correlation coefficient than achieved with any number of profiles, and a (slightly) smaller rms error for the timeseries of the maximum and the time-mean of vertical profile than achieved with 11 profiles.

It is only seemingly paradoxical that at 53°N the reconstruction becomes worse when a higher number of profiles is used. One needs to distinguish between the quality of the reconstruction of the total MOC and the quality of the reconstruction of the thermal wind contribution. With more profiles, the thermal wind reconstruction gets closer to the thermal wind reconstruction that is based on the maximum number of profiles. However, this does not necessarily mean that the reconstruction of the total MOC improves. In particular, errors in the reconstruction arise if the assumption of small bottom velocities is invalid. One indication of this is that the low-frequency part of the thermal wind contribution at 53°N varies with time, but the low-frequency part of the MOC does not. Thus, a setup with 7 profiles or less does not capture the basic characteristics of the MOC for the right reasons, it merely benefits from the coincidental compensation of neglected factors.

In summary, at 26°N and 36°N the standard array is the minimal setup allowing a reliable estimate of the MOC, which cannot be significantly increased using a slightly higher number of profiles. For both 26°N and 36°N, the standard configuration and an array relying on the full model density information provide nearly the same quality for the resulting reconstruction. However, the quality of the reconstruction at 53°N is considerably less, with any numbers of profiles. To investigate this and the limited ability of the array to capture the deep return flow for the three considered latitudes, the force balance governing the MOC are analyzed.

2.3.4 Limits of the Method

To identify the dominating terms governing the MOC at the different latitudes we investigate which part of the velocity field is not captured by the array. A comparison of the estimated meridional velocities and the original meridional (model) velocities shows that errors in the mean velocity field are mainly caused by differences between the two depth-averaged fields rather than differences in the thermal wind shear or Ekman reconstruction.

A contribution by the depth-averaged velocity component to the MOC arises when (strong) currents hit sloping boundaries, i.e. in the presence of non-uniform topog-

raphy, and the external mode projects onto the meridional overturning (Lee and Marotzke, 1998). Its overturning contribution vanishes for zonally uniform topography. However, the link of the external mode to density differences is not straightforward as it is difficult to separate thermal wind and ageostrophic shear contributions in section integrations (Robbins and Toole, 1997; Lee and Marotzke, 1998). Note that the spatially uniform correction applied to ensure mass balance also generates a depth-independent component in the reconstructed velocities.

In order to analyze the ability of the array to capture the external mode, the overturning contribution by the external mode is calculated for both the original model velocities and the reconstructed velocities.

$$\Psi_{ext}(y,z) = \int_{-D(x,y)}^{z} \int_{0}^{L(y,z)} \tilde{v}(x,y,z)dxdz, \tag{2.8}$$

where $\tilde{v}(x,y,z)$ is the depth-averaged velocity $\overline{v}(x,y) = \frac{1}{D(x,y)} \int_{-D(x,y)}^{0} v(x,y,z)dz$, evenly distributed over the water column.

Figure 2.9 shows a timeseries of the maximum and a time-mean vertical profile for each latitude. For 26°N the external mode is reconstructed by the array, since the complete velocity pattern in the Florida Strait (where the strongest depth-averaged velocities occur) is included in the array. This is true for both the timeseries of the maximum and the vertical structure. The external mode has its maximum projection onto the MOC (of about 25 Sv) at 800 m, which coincides with the maximum depth of the Florida Strait. For 36°N a small (and apart from high frequency fluctuations temporally nearly constant) part of the external mode is not estimated by the array. The vertical structure is reproduced, apart from the underestimate of the maximum of about 3 Sv. At 53°N a considerable (and variable) part of the external mode is underestimated in its absolute value. In the time-mean vertical structure, the maximum value is missed by about 4 to 5 Sv.

Theoretically, the discrepancy between the original and reconstructed external mode can be added to the reconstructed overturning:

$$\Psi(y,z) = \Psi_{tw}(y,z) + \Psi_{ek}(y,z) + (\Psi_{ext_{model}}(y,z) - \Psi_{ext_{reconstr}}(y,z)), \tag{2.9}$$

where $\Psi_{ext_{model}}(y,z)$ is calculated based on the meridional velocity field from the model and $\Psi_{ext_{reconstr}}(y,z))$ computed using the corrected thermal wind velocity field $v_{g_{corr}}(x,y,z)$ (equation 2.4) substituted into equation (2.8). Little effect is

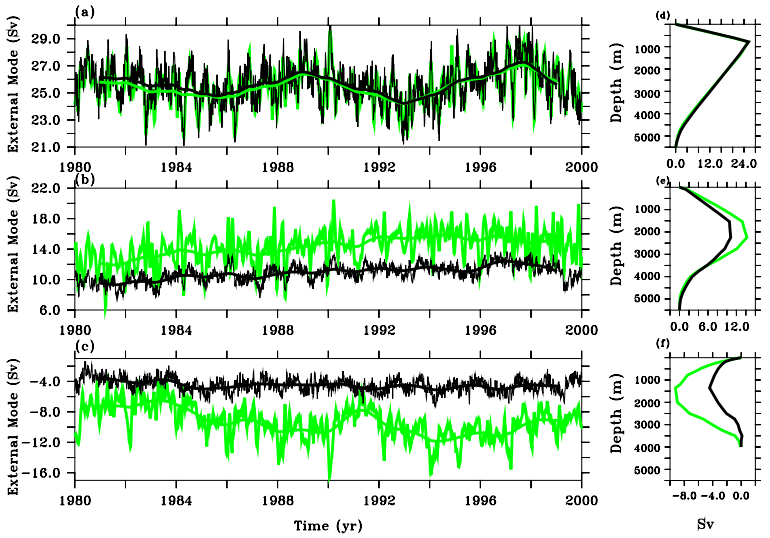

Fig. 2.9: External mode (model, green) and estimated external mode (black). Timeseries of maximum is shown in (a) - (c), and the time mean vertical profile in (d) - (f); 26°N: (a) and (d), 36°N (b) and (e), 53°N (c) and (f). Solid line in the timeseries of the maximum indicates 2 year running mean.

seen for 26°N, whereas for 36°N and 53°N the mean value of the maximum overturning is estimated correctly when the missing depth-averaged part is taken into account (figure not shown). Furthermore, for each of the three latitudes the deep branch of the vertical profile can be largely estimated. Thus, the overturning contribution originating from the difference between the original model and the estimated external mode does account for most of the bias in the reconstruction.

The depth-averaged velocity ($\overline{v}(x,y)$) field can presently not be measured. It is under idealized circumstances a sum of the velocities generated by the thermal wind and the surface wind stress plus the velocities at the bottom of the water column $v_b(x,y,z)$: $\overline{v}(x,y) = v_g(x,y,z) + v_{ek}(x,y,z) + v_b(x,y,z)$.

In this study so far, bottom velocities are assumed to be zero everywhere. The bottom of the basin was chosen as the reference level for the thermal wind calculations, i.e. integration starts at the bottom, where the geostrophic velocity is assumed to be zero. This assumption is clearly insufficient when high velocities occur at the bottom, e.g. when a deep boundary current hits a continental slope, where velocities can be as high as 10 cm s^{-1} (Lee et al., 1990, 1996). Analyzing both the bottom velocity field and the depth-averaged velocity field in FLAME shows that the strongest bottom and depth-averaged velocities occur for all three latitudes at the western boundary, where currents are strongest. The time-mean bottom veloci-

ties have absolute values of up to 3 cm s^{-1} for the subtropical latitudes, and values in the range of 5 to 20 cm s^{-1} for 53°N. The depth-averaged velocities exceed the bottom velocities by several tens of cm s^{-1} at the western boundary at 26°N and 36°N. At 53°N, where the stratification is weakest, the bottom and depth-averaged velocities tend to be of the same order of magnitude at the western boundary. Away from the western boundary, the depth-averaged velocities are weaker than the bottom velocities for all three latitudes.

Instead of assuming a level of no motion at the bottom of the basin, bottom velocities could be taken as the reference level for the calculation of the thermal wind velocities estimated by the standard array. Thus, the reconstruction is now tested assuming the bottom velocities to be known (at all bottom grid points):

$$\Psi(y,z) = \Psi_{tw}(y,z) + \Psi_{ek}(y,z) + \Psi_b(y,z), \tag{2.10}$$

where $\Psi_b(y,z)$ is the overturning contribution originated by the bottom velocities $v_b(x,y,z)$. Again, a correction ensuring mass balance is applied prior to the integration.

$$\Psi_b(y,z) = \int_{-D(x,y,)}^{z} \int_0^{L(y,z)} v_{b_{corr}}(x,y,z)dxdz, \tag{2.11}$$

in which $v_{b_{corr}}(x,y,z)$ is the corrected bottom velocity field:

$$v_{b_{corr}}(x,y,z) = v_b(x,y,z) - \frac{\int_{-D(x,y)}^{z} \int_0^{L(y,z)} v_b(x,y,z)dxdz}{A}. \tag{2.12}$$

Velocities at the bottom of the basin are replaced by its original model value. The overturning contribution due to the bottom velocities is corrected and integrated separately to give an estimate of its relative contribution. The same result would be achieved if the bottom velocities would be included into equation (2.4) and $\Psi_{tw}(y,z)$ re-computed accordingly.

The time mean vertical profile of $\Psi_b(y,z)$ shows a distinctive negative extreme for all three latitudes, differing considerably in its vertical placement and relative importance (figure not shown). The time mean maximum for 26°N is -1.2 Sv and situated at a depth of about 4700 m. 36°N exhibits a comparable negative maximum at a slightly shallower depth of about 4200 m. In addition, 36°N shows a positive maximum of 1.6 Sv at depths ranging from 1500 m to 3000 m, where the northward boundary current hits the western slope of the basin. The time mean vertical profile

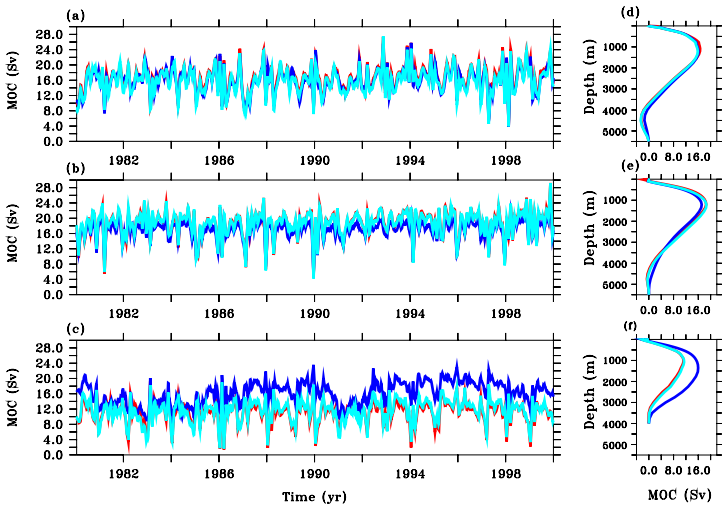

Fig. 2.10: MOC (red), estimated transport (blue) on the basis of the standard arrays, and estimated transport on the basis of the standard arrays plus bottom velocity contribution (light blue). The estimated transport is the sum of the thermal wind and Ekman contributions. The bottom velocity contribution is based on the knowledge of the bottom velocities at every zonal grid cell. Timeseries of the maximum transports are shown in figures (a) - (c), and a time mean vertical profile in figures (d) - (f); 26°N: (a) and (d), 36°N (b) and (e), 53°N: (c) and (f).

for 53°N has its maximum of -5.8 Sv at a depth of about 2000 m, corresponding to the strong northward boundary current hitting the western slope at this depth.

The resulting reconstruction based on the knowledge of the complete bottom velocities added to the thermal wind and Ekman reconstruction based on the standard array is shown in figure 2.10. Again, the timeseries of the maximum and the time-mean vertical profile are shown for both the original and reconstructed overturning. The reconstruction follows the original overturning in both its mean value and its complete temporal variability closely for all three latitudes. The time-mean vertical profile (including the deep return flow) is reconstructed well for the three different transects.

In an attempt to reduce the amount of required information, the reconstruction is tested based on bottom velocity measurements at the locations of the profiles only. The resulting $\Psi_b(y,z)$ is very different from the one based on the complete bottom velocity field. The changes in the resulting time mean vertical profiles range from a reduction in magnitude by a factor 0.2, a displacement of the maximum in the vertical by 500 m to a change of sign for the maximum value, depending on latitude and profile placement. A reconstruction based on enhanced knowledge of bottom velocities at the western boundary shows similar behavior.

Generally, in the presence of strong bottom velocities the MOC cannot be reliably estimated based on density and wind measurements alone. Here, the MOC could be reconstructed based on the standard arrays for the individual latitudes plus additionally known bottom velocities at every zonal grid point. Currently, this is clearly an unrealistic condition, but it points to an observational requirement for the future.

2.4 Meridional Heat Transport

The MOC is responsible for a net northward heat transport in the Atlantic of about 1 PW at 25°N (Hall and Bryden, 1982), which accounts for approximately half of the total northward heat transport in the North Atlantic region, where the atmosphere provides the remaining half (Trenberth and Solomon, 1994). As variations in the ocean heat transport are expected to arise predominately from fluctuations in the velocity field (Jayne and Marotzke, 2001), the reconstructed velocity field should allow an estimate of the meridional heat transport, too. The meridional heat transport across each latitude is calculated from the reconstructed velocities and a temporally constant temperature section taken at the beginning of the 'deployment period', assuming that changes in the velocity fields are rapid compared to the variations of the temperature field (Jayne and Marotzke, 2001).

Figure 2.11 shows the meridional heat transport based on the standard array for the three latitudes. For both 26°N and 36°N there is a good agreement between the estimated and modeled meridional heat transport. The mean value is reproduced well, whereas the variability is generally slightly underestimated. For 53°N the reconstruction fails temporally by up to ± 0.3 PW, these temporal over- and underestimates compensate each other resulting in a coincidentally correct reconstruction of the 20 yr time-mean value of 0.6 PW.

A decomposition of the meridional heat transport into its overturning and gyre contribution (Böning and Bryan, 1996; Bryden and Imawaki, 2001) shows that the overturning contribution is reconstructed correctly in its mean value and variability for the three latitudes. The gyre component is covered for 26°N (-0.1 PW) and 36°N (0.05 PW) only. At 53°N, in contrast, the mean value (about 0.45 PW) and the temporal variability of the gyre component are missed. The relatively large gyre component at 53°N originates from strong horizontal temperature gradients, maintaining a weak stratification. The latter, in turn, allows for strong depth-independent velocities, i.e. a strong influence of the bottom topography on the

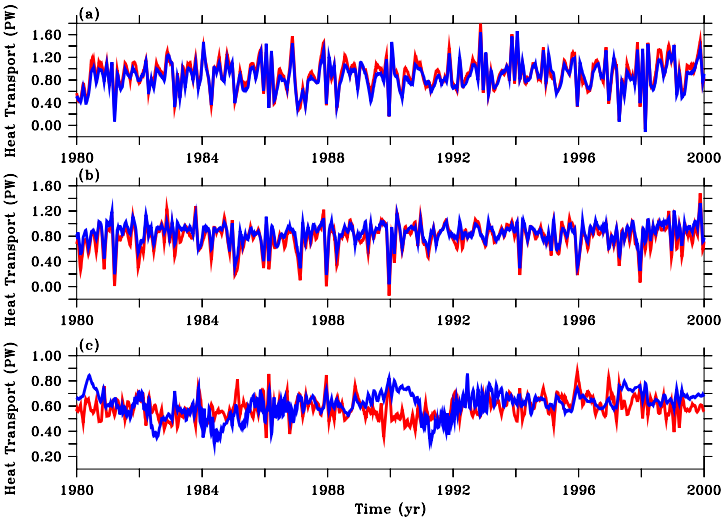

Fig. 2.11: Meridional heat transport taken from FLAME (red) and its reconstruction (blue). The reconstruction is based on the standard array (incl Ekman velocities), combined with an initial temperature section (kept constant after first timestep). 26°N: (a), 36°N (b), and 53°N: (c).

velocity field, which is equivalent to a large external mode. Again, a reconstruction based on known bottom velocities captures both the mean value and the temporal variability.

2.5 Discussion

To assume complete knowledge of the bottom velocities is possible in a model study, but not (yet) feasible in the real ocean. Bottom velocities can be obtained from direct measurements or bottom pressure recorders (e.g. Meinen et al. (2004)) as they are planned to be deployed within the UK RAPID array (Natural Environment Research Council, 2003). The resolution of these measurements, however, is much coarser than the one assumed here. Generally, bottom velocities could be inferred from the seafloor pressure gradients obtained through the satellite measurements, implying geostrophy (Wahr et al., 1998). Such satellite measurements with an adequate resolution of bottom pressure measurements might become available in the near future (Wahr et al., 2002; Losch et al., 2002). Whether those satellite based bottom pressure measurements would be sufficient as a reference level for the thermal wind integration demands profound testing. Simulating the effect of these bottom pressure measurements is beyond the scope of this paper, since it would require disproportionate effort to derive the bottom pressure timeseries as FLAME is run with a rigid lid surface. Nevertheless, the use of bottom pressure measurements needs to be tested, possibly with a numerical model, and if applicable the required

resolution and accuracy needs to be established.

Generally, an inevitable limitation to the transferability of this model-based array design study is the restricted ability of the employed model to represent the ocean circulation in its full complexity. First, despite its vigorous overturning, FLAME's representation of the deep 'western' boundary current is limited, both in its respective geographical position and absolute strength: at 26°N the core of the deep western boundary current is situated above the depth of the crest of the MAR, which is not in accordance with observations, e.g. Lee et al. (1996). At 36°N the strongest southward flow is found at the surface in the western part of the basin and a deep southward flow is found at the western slope of the MAR. Although observational evidence is limited, the results show a deep western boundary current situated beneath the northward boundary current, e.g. Roemmich and Wunsch (1985) and Rintoul and Wunsch (1991).

Second, limited spatial resolution plays a role: Although FLAME is an 'eddy-permitting' model, it does not resolve eddies, and the eddy kinetic energy is still underestimated significantly (Stammer et al., 1996). This should be taken into consideration for the analysis of the return flow, since the model may underestimate the variability as well as the strength of the boundary currents. Further, the spatial resolution restricts the placement of the density profiles. The total width of the western boundary current based on observations is given for 26°N as about 80 km (Lee et al., 1996). In contrast, FLAME's grid cell spacing at 26°N is about 33 km. Hence, to cover the westernmost margin sufficiently some of the profiles are placed at adjacent grid cells. Thus, because of the model's constraints in describing the real world, some of the specific results generated by the model cannot directly be applied to the real world.

Returning to the broader perspective of observing system design, fundamentally, one wishes to determine the array configuration yielding the most comprehensive information from the observational data within the given constraints (e.g. instrumentation cost). In principle, the required objective function needs to map the dynamics of the unknown field, and the available resources adequately. To our knowledge this optimization problem has been systematically addressed for only two idealized examples, neither directed at realistic observing system design: Barth and Wunsch (1990) used two horizontal dimensions for a time-independent experiment and Barth (1992) used a 4 x 4 box model. Whereas it does not seem feasible to conduct a comprehensive array design study with the the current computational resources, this might be possible in the future. However, it remains to be established

if idealized, i.e. not dependent on any prior observations, optimization techniques perform better than heuristic array design based on physical intuition, taking into account our - albeit limited, but still significant - knowledge of the ocean dynamics.

Here, we test an observational method, relying on a feasible, i.e. financially realistic, experimental setup only. Whether an arbitrary latitude is suitable for potential observation requires knowledge about the real meridional velocity field (e.g. a hydrographic section). Most importantly, the magnitude of the bottom velocities and the capability of the array to capture the external mode at this latitude needs to be ensured. Further, when assessing a chosen latitude for observation, adequate placement of the profiles requires knowledge to what extent the model velocity field and the velocity field expected in the real ocean are congruent.

Simulating an array at a chosen latitude requires first the definition of a set of available resources (including potential preexisting continuous observations). Second, the profiles should be placed according to the two criteria described in the beginning of section 2.3: (*i*) the profiles need to be placed especially in areas of high meridional velocities, and (*ii*) maximum spatial coverage of the basin should be ensured by the resulting array. Third, the MOC reconstruction can be computed according to equation (2.7).

Comparing the three investigated latitudes for potential observation in the real ocean suggests that 26°N is superior to 36°N and 53°N. At 26°N the MOC in FLAME can be reconstructed based on the thermal wind contribution, the Ekman contribution and continuous 'measurements' of the Florida Strait transport. The bottom velocities are small and the sidewalls are steep, and the depth averaged velocities therefore account (outside the Florida Strait) for a negligible overturning contribution only. A variety of practical reasons further supports the recommendation of 26°N. First, this latitude has been occupied four times with hydrographic transects (see section 2.3.1). Second, the geographically confined western boundary current has been monitored by cable measurements for more than 20 years (Larsen, 1985; Baringer and Larsen, 2001). Third, 26°N is close to the heat transport maximum in the Atlantic and in turn the heat transport is dominated by the MOC, i.e. the gyre component is small (Hall and Bryden, 1982).

Ultimately, one would want to extend the analysis of the force balances governing the MOC to all latitudes of the North Atlantic. In a detailed analysis of the force balances in a hierarchy of ocean models Hirschi and Marotzke (2006) suggest that

this method has the potential to provide valuable information about the full meridional overturning cell. However, their analysis is not directed at observing system design and therefore does not assess which latitude would be most suitable for observation. In principle, the ratio of the overturning contribution of the external mode to the MOC could provide some measure for this. However, the required calculation would be extremely demanding for FLAME and is left for future study.

2.6 Conclusions

Based on our analysis of FLAME, we conclude:

1. A small number of profiles (about 10) is sufficient to capture the main characteristics of the MOC for a single latitude in the North Atlantic as long as bottom velocities are small, here, at 26°N and 36°N.

2. In case of high bottom velocities the depth-averaged velocity field is not captured by the array. Thus, the MOC cannot be reliably estimated based on an array 'measuring' density and surface wind stress only, here, at 53°N.

3. An array that additionally incorporates the complete bottom velocity field, reproduces the MOC in its temporal and vertical structure.

4. Effectively, we confirm that the thermal wind and the Ekman contributions are the dominant terms in the force balance governing the MOC, with sometimes significant but generally smaller contributions from other terms.

5. Of the three latitudes analysed here, 26°N is the one most suitable for observation in the real ocean: it allows comparison with historical data, the western boundary current has been monitored continuously, and the depth-averaged velocity field is - in FLAME - largely captured by the array.

Acknowledgements We wish to thank Harry Bryden for stimulating discussions and Johann Jungclaus for helpful comments on the manuscript. We are indebted to the two reviewers for their thorough reviews. This work was supported by the Natural Environment Research Council (NERC), the University of Southampton and the Max Planck Society.

2.7 Appendix

This Appendix has not been published in Baehr et al. (2004). I find it, however, useful to include figure 2.12 here, as it depicts a more coherent visualization of the results presented in chapter 2. In this Taylor Diagram (Taylor, 2001), the quality of the MOC reconstruction is measured by the distance of the marker representing the chosen setup to the corresponding marker on the abscissa (figure 2.12). For 26°N and 36°N, the 'standard' array shows both a high correlation and a small root mean square error (rmse) with the original MOC timeseries, whereas for 53°N the correlation is low and the rmse is large. The reconstruction including bottom velocities shows correlation coefficients of above 0.95, and rmse of less than 1 Sv for all three latitudes. Note that the rmse in figure 2.12 does not mirror a difference in the mean value, which is indicated by the shading of the respective marker.

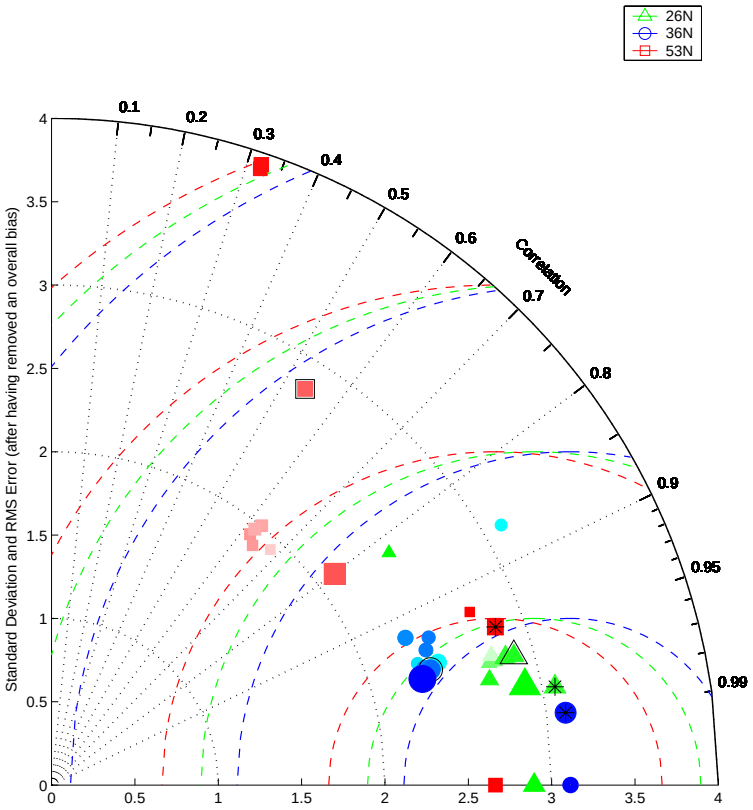

Fig. 2.12: Taylor Diagram (Taylor, 2001): The variability of the model MOC timeseries is shown on the abscissa - 26°N (green), 36°N (blue), 53°N (red). The concentric circles around the respective marker indicate lines of constant root mean square error. The markers for the reconstructed maximum MOC vary in size: the smaller the marker the fewer density profiles are used (from 2 profiles up to about 10 profiles; the largest marker representing the maximum number of profiles). The shading visualizes the overall bias relative to the model MOC: the darker the marker, the smaller the bias. The marker outlined marker represents the 'standard' setup introduced in chapter 2.3.1. The marker with an asterisks on top is based on the additional use of the bottom velocity field.

3. OPTIMIZING A MODEL-BASED OBSERVING SYSTEM DESIGN[1]

Abstract
Three methods are analyzed for the design of ocean observing systems to monitor the meridional overturning circulation (MOC) in the North Atlantic. Specifically, a continuous monitoring array is 'deployed' into a numerical model. We compare array design methods guided by (*i*) physical intuition (heuristic array design), (*ii*) sequential optimization, and (*iii*) global optimization. It is found that global optimization can recover the true global solution for the analyzed array design. Both global optimization and heuristic array design yield considerably improved results over sequential array design. Global optimization always outperforms the heuristic array design in terms of minimizing the root mean square error. However, whether the results are physically meaningful is not guaranteed; the apparent success might merely represent an optimal solution in which misfits compensate each other accidentally. Testing the solution gained from global optimization in an independent data set can provide crucial information about the solution's robustness.

3.1 Introduction

The design of efficient observing systems plays a key role in oceanography as measurements are difficult and costly to obtain. A variety of studies have simulated observing arrays in numerical models to assess the observing system's performance or to address the fundamental principles of observing system design (see *e.g.* Baehr et al. (2004) for an overview). Most of these studies used trial-and-error adjustment of their array configurations (*e.g.*, Bretherton et al., 1976; McIntosh, 1987). Notable exceptions are Barth and Wunsch (1990) and Barth (1992), who analyzed the optimization of idealized cases. Few studies have been specifically directed at pre-deployment array design (Hackert et al., 1998; Hirschi et al., 2003; Baehr et al.,

[1] Baehr J., D. McInerney, K. Keller, J. Marotzke (2006): Optimizing a model-based observing system design for the North Atlantic meridional overturning circulation, in preparation as a note for *Journal of Atmospheric and Oceanic Technology.*

2004); their array design methods relied on physical intuition. In contrast to earlier studies, the present study combines array design directed at providing immediate support for a realizable campaign with a formal optimization of the simulated array. We compare three array design methods: array design guided by physical intuition (heuristic array design), sequential optimization, and global optimization.

This note is organized as follows: Section 2 introduces the analyzed data set, the simulated monitoring array, and the global optimization method. The results for three different array design methods are presented in section 3, and are discussed in section 4. Conclusions are given in section 5.

3.2 Data and Methods

3.2.1 Data Set

We analyze model output of the 1/3° Atlantic Model of the FLAME group, a hierarchy of Atlantic Ocean models (Dengg et al., 1999; Beismann and Redler, 2003). The horizontal resolution is 1/3° in longitude and $1/3° \times cos(\phi)$ in latitude (ϕ). The model setup and the analyzed output are identical to the configuration and data used in Baehr et al. (2004). The analyzed timeseries span 20 years, starting at the model time 01 January 1980. The temporal resolution of the employed model output is 5 days.

3.2.2 Simulated Observing System

The simulated observing system is designed to allow continuous monitoring of the oceanic meridional overturning circulation (MOC) at a specific latitude. It is based on the monitoring strategy proposed by Marotzke et al. (1999): Thermal wind and Ekman contributions to the MOC are measured separately, and the resulting meridional transports are corrected to ensure closed mass balance over the longitudinal transect (Hirschi et al., 2003). Köhl (2005) and Hirschi and Marotzke (2006) showed that the thermal wind part and the Ekman transport are indeed the dominant contributions to the MOC in the North Atlantic. The recently deployed RAPID-MOC 26°N array is based on this monitoring strategy (Marotzke et al., 2002; Schiermeier, 2004), with the additional use of continuous measurements of the western boundary current in the Florida Strait (Baringer and Larsen, 2001).

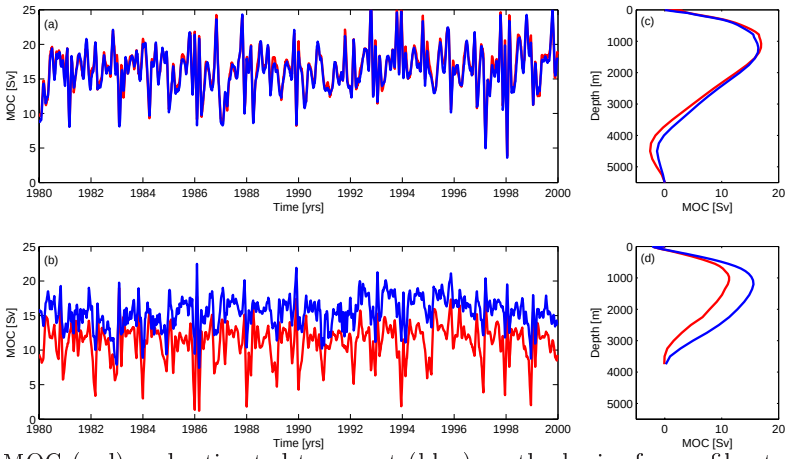

Fig. 3.1: MOC (red) and estimated transport (blue) on the basis of a profile at every grid point ($n = n_{max}$). The estimated transport is a sum of two constituents: thermal wind and Ekman contribution. (a) 26°N, (b) 53°N. Time-mean vertical profile: (c) 26°N, (d) 53°N.

The observing strategy was tested at different latitudes (Baehr et al., 2004), suggesting that this monitoring strategy would be able to capture the main features of the time-mean and the variability of the MOC at 26°N, but not at 53°N. Figure 3.1 shows the resulting MOC reconstructions compared to the original (model) MOC at 1000 m for both latitudes, based on a simulated measurement at every grid cell, *i.e.* the maximum number of profiles ($n = n_{max}$; $n_{max} \approx 200$ for 26°N, and $n_{max} \approx 140$ for 53°N). Each profile simulates a full depth mooring, measuring temperature, salinity and pressure at discrete depths.

3.2.3 Differential Evolution (DE)

Identifying a spatial array design with a minimal root mean square error (rmse) poses a global optimization problem with integer constraints. The key challenge in global optimization is to reliably identify the best (global) optimum within feasible computation times. Currently available global optimization algorithms differ considerably in their convergence speed and the quality of the identified solution (Athias et al., 2000; Moles et al., 2004; Ali et al., 2005). Previous studies analyzing the spatial design of ocean observing systems used simulated annealing or evolutionary strategies (Barth and Wunsch, 1990; Barth, 1992; Hernandez et al., 1995). Here we adapt the differential evolution algorithm (Storn and Price, 1997). The original algorithm is relatively robust in achieving the true global solution with feasible computational requirements (Moles et al., 2003, 2004; Storn and Price, 1997). We demonstrate the skill of the new algorithm to reliably identify the global optimum for a range of test-problems.

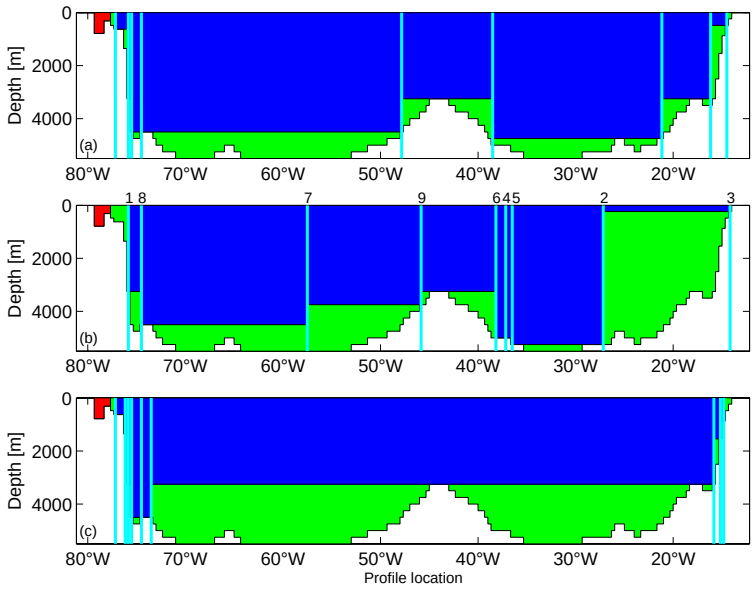

Fig. 3.2: 26°N: Profile locations for different array design methods: (a) heuristic array design, (b) sequential optimization, (c) global optimization; for $n = 9$. Blue shading indicates where profiles provide estimate of velocity shear. Green shading indicates bottom triangles, *i.e.*, areas where adjacent profiles are not able to provide estimate of velocity shear. Red shading indicates region of western boundary observation (Florida Strait). Light blue lines indicate longitude of profile. In panel (b), the number above the profile indicates its rank order in the sequential design.

Evolutionary optimization methods adopt the sequence of mutation and selection steps observed in nature (Goldberg, 1989). The algorithms start by producing a random initial set of possible solutions (typically referred to as population). In our example, population members are feasible array designs. The population members are evaluated using an objective function to determine their fitness. We define fitness as the negative root mean squared error as we are interested in a minimal root mean squared error. A subset of well-performing population members are then used to produce a new population with a superimposed random variation. The random variability is akin to the mutation process in natural evolution. This sequence is iterated until the algorithm has converged. The original differential evolution algorithm is designed for an unconstrained problem with continuous variables. We impose two constraints such that moorings are located in the model domain and are unique by adding a penalty function. We round the continuous variables in the algorithm to the nearest integer to represent the integer grid locations in this model analysis. We assess convergence by repeating the optimization step with different random initial conditions similar to McInerney and Keller (2006).

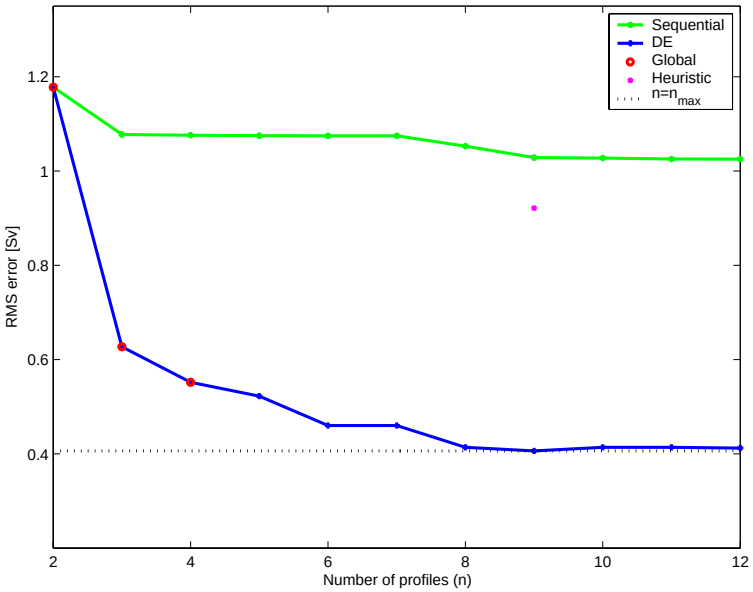

Fig. 3.3: 26°N: Root mean square error (rmse) for different array design methods: green: sequential optimization, blue: global optimization (DE), red: true global solution, magenta: heuristic design.

3.3 Array Design

Here, we optimize the suggested array to monitor the MOC at 1000 m using different array design methods: Initially, we briefly recapitulate on intuition based array design; subsequently, both sequentially optimized array design and globally optimized array design methods are tested. Although we test different numbers of profiles (starting at $n = n_{max}$), the overall aim is to evaluate the locations of profiles for a feasible amount of profiles, and we therefore restrict the analysis to about 10 profiles. We test the observing strategy both at 26°N and 53°N. Of the available model output of 20 years (*cf.*, figure 3.1), we use initially 10 years (section 3.3.1 - 3.3.5), and test subsequently if the obtained results are robust for the second decade (section 3.3.6).

3.3.1 26°N: Heuristic Design

The heuristic array design, *i.e.* intuition-based placement of the profiles, was used in Hirschi et al. (2003) and Baehr et al. (2004). For the present analysis, we use the 'standard' setup as derived in Baehr et al. (2004). The design of this setup was guided by two criteria: (*i*) the profiles should be placed preferentially in areas where the meridional velocities are assumed to be high, and (*ii*) the resulting array should cover as much of the section area as possible, *i.e.*, minimizing the remaining bottom triangles (Baehr et al., 2004). The resulting array setup consisted of nine profiles:

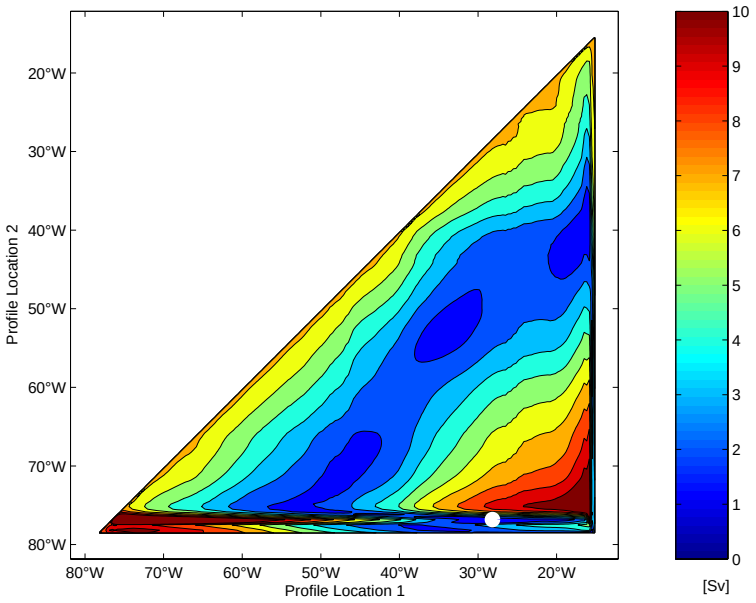

Fig. 3.4: Root mean square error (rmse) for all combinations of two profiles at 26°N. White marker indicates profile combination with smallest rmse.

four profiles at the western margin to ensure a dense coverage of the steep slope, a profile at each side of the Mid Atlantic Ridge (MAR) to ensure the coverage of the deep sub-basins west and east of the MAR, and three profiles at the eastern margin to ensure coverage of the gentle slope at this side of the basin (figure 3.2a). The root mean square error between the model MOC and the reconstructed MOC based on the above described setup is about 0.95 Sv (figure 3.3).

3.3.2 26°N: Sequential Optimization

Several studies have used an incremental approach for the design of observing systems (*e.g.*, Rayner et al., 1996; Gloor et al., 2000; Patra and Maksyutov, 2002). This approach has the advantage of being computationally efficient, and is arguably a useful framework if the locations of an existing observing system are constrained. Aiming to achieve an optimal design, we start with a sequential optimization, *i.e.*, finding the optimal placement for one profile at a time, in addition to an existing setup. The starting point is an extensive search for two profiles. The smallest rmse between the model MOC and the reconstructed MOC of about 1.2 Sv is found when one profiles is placed close to the western boundary, and the second one in the middle of the basin east of the MAR (figure 3.4). Profiles are added sequentially to this setup, finding at each iteration the location with the minimum rmse (figure 3.2b). The setup for $n = 9$ uses profiles evenly distributed over the transect, with the ex-

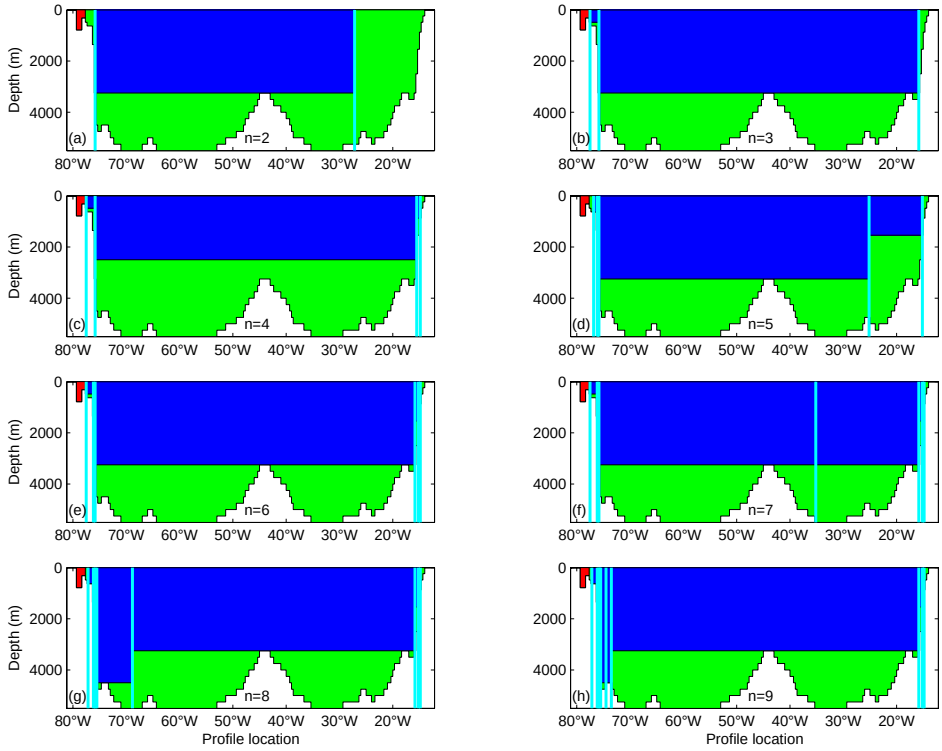

Fig. 3.5: 26°N: profile locations for global optimization using differential evolution for $n = 2, ..., 9$. Blue shading indicates where profiles provide estimate of velocity shear. Green shading indicates bottom triangles, *i.e.*, areas where adjacent profiles are not able to provide estimate of velocity shear. Red shading indicates region of western boundary observation (Florida Strait). Light blue lines indicate longitude of profile.

ception of the deep eastern boundary (figure 3.2b). The resulting rmse decreases for a higher number of profiles, but even for nine profiles it is above the rmse reached for the heuristic design (figure 3.3).

3.3.3 26°N: Global Optimization

The underlying optimization problem is nonconvex (*cf.*, figure 3.4), which requires the use of a global optimization technique. First, we test the differential evolution (DE) algorithm against the true global solution. The DE algorithm does recover the global optimum for $n = 2,3,4$ (figure 3.3), *i.e.*, the cases where it is computationally feasible to test this.

For the global optimization, the rmse decreases with higher numbers of profiles, and converges to the solution with the maximum number of profiles ($n = n_{max}$) with an rmse of about 0.4 Sv at $n = 8$ (figure 3.3). In contrast to the sequential optimization,

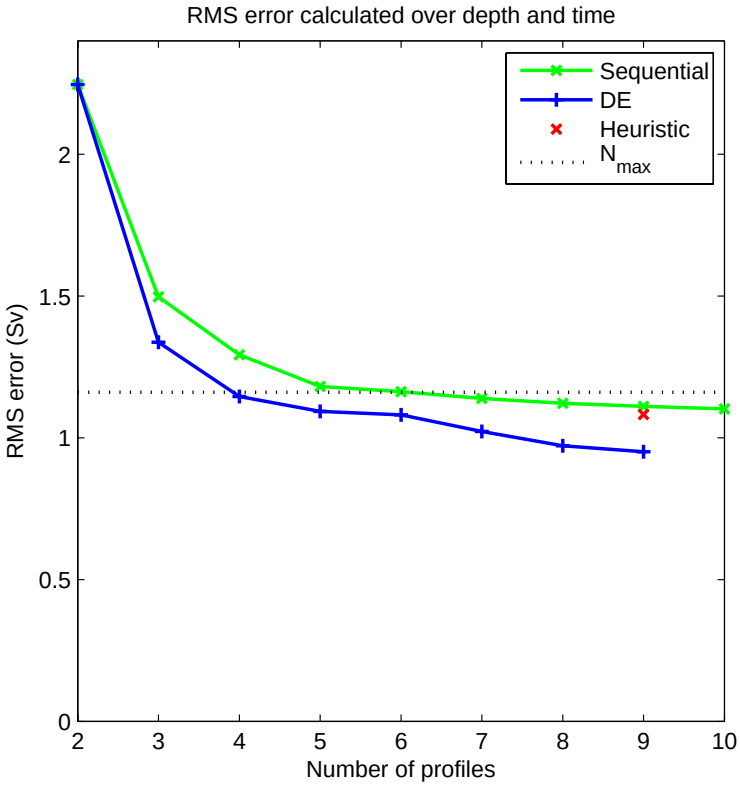

Fig. 3.6: 26°N: Root mean square error (rmse) for different array design methods over full depth: green: sequential optimization, blue: global optimization (DE), red: heuristic design, black: $n = n_{max}$.

the DE method favors profiles at the boundaries, particularly the western boundary (figure 3.2c), at the expense of profiles close to the MAR. All solutions n = 3,...,9 include the shallow part of the western boundary (figure 3.5), which is entirely missed by the sequential array design.

3.3.4 26°N: Vertical Profiles

So far, only the rmse between the model MOC and the reconstructed MOC at 1000 m depth are considered; showing that the mean value and variability can be captured, depending on the specific array design. The deep return flow is, however, for most of the setups, entirely missed, *i.e.* the time mean vertical profile shows no local minimum. For the global optimization, higher number of profiles ($n > 7$) show a weak return flow of about 1 Sv [not shown]. The heuristic design underestimates the return flow by about 2 Sv. However, all methods do - in the vertical - at some point better than the $n = n_{max}$ setup (figure 3.6), since the $n = n_{max}$ setup underestimates both the mean strength of the northward and the southward flow. While the global

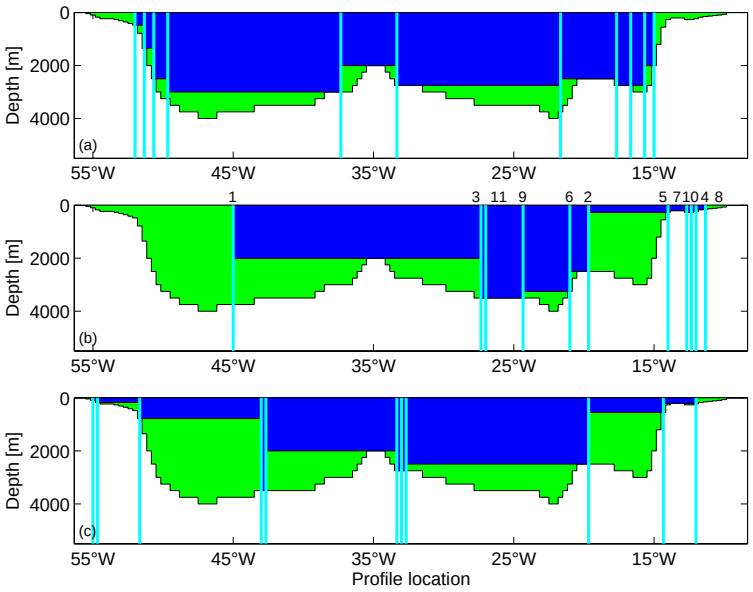

Fig. 3.7: 53°N: location of profiles for different array design methods: (a) heuristic array design, (b) sequential optimization, (c) global optimization (DE); for $n = 9$. Blue shading indicates, where profiles provide estimate of velocity shear. Green shading indicates bottom triangles, *i.e.*, areas where adjacent profiles are not able to provide estimate of velocity shear. Light blue lines indicate longitude of profile. In panel (b), the number above the profile indicates its rank order in the sequential design.

optimization finds setups in which the bias in the northward flow is reduced by chance, the heuristic design finds setups in which the bias in the southward flow is reduced by observing the western boundary more intensively. The reconstruction for both setups relies in part, *i.e.*, for about 2 Sv in the northward or southward flow, on a fortuitous overestimate of the flow, gained from an incidental imbalance delivered by the chosen subset of profiles.

3.3.5 Array Design at 53°N

We repeat the application of the three array design methods at 53°N, a latitude where the method in its basic setup generally not succeeded in capturing the mean value and variability of the MOC (Baehr et al., 2004). Again, the heuristic array design aimed to cover most of the meridional velocities as well as most of the transect area (figure 3.7a). The rmse of the resulting setup is about 4 Sv (figure 3.8). Both the sequential and the global optimization array design approach result in considerably smaller rmse (figure 3.8). The sequential array design does not take into account the western boundary (figure 3.7b), where the highest southward velocities occur (*cf.*, figure 2c in Baehr et al. (2004)). The DE based array design includes the the

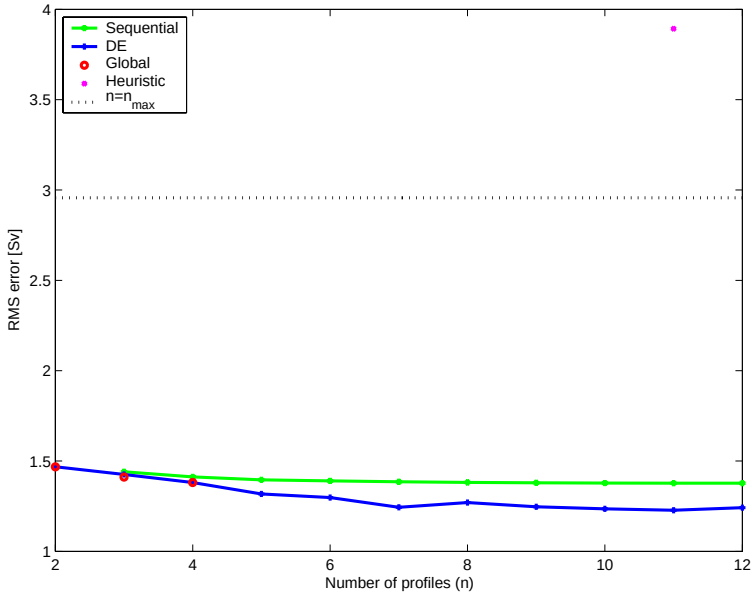

Fig. 3.8: 53°N: Root mean square error (rmse) for different array design methods: green: sequential optimization, blue: global optimization (DE), red: true global solution, magenta: heuristic design.

entire transect, but large bottom triangles are left out (figure 3.7c). Note that the sequential and the global optimization result in a considerably smaller rmse than the setup for $n = n_{max}$ (figure 3.8), which is due to an coincidental balance of overestimates and underestimates in the meridional transports, *i.e.* not representing the full dynamics of the meridional velocity field.

3.3.6 Analysis of a Second Decade

Having analyzed the first decade of the employed data set, we test whether the obtained results are robust for the second decade. For both latitudes, we take the profile locations of the three different array design methods and compute the resulting rmse. At 26°N, the rmse for between the model MOC and the reconstructed MOC at 1000 m depth are similar for the first and the second decades. The rmse for the DE based array design, and the heuristic array design are nearly identical, while the rmse for the sequential array design increases by about 0.2 Sv. At 53°N, in contrast, the rmse for the optimal and the sequential array design nearly doubles, but is still lower than the rmse for $n = n_{max}$. For the sequential array design, the rmse in the second decade is lower for $n = 2$ than for $n \geq 3$. For the heuristic array design, the rmse increases from about 5 Sv in the first decade to about 6.5 Sv in the second decade, both values are above the respective rmse for $n = n_{max}$.

3.4 Discussion

We test three different array design methods for a suggested monitoring strategy of the MOC. Testing the profile locations derived from analyzing the first decade within the second decade, allows to test whether the suggested array setup is robust with respect to its physical meaning. The results suggest that both the results from the global optimization and the sequential array design are robust at 26°N, but not for 53°N. The results at 53°N are therefore of limited use, as are the physical insights to be gained from the analysis of the results. The results gained from analyzing 53°N do, however, allow the immediate conclusion that the monitoring strategy itself has to be applied with great care. In contrast, the results of the heuristic array design are robust for both latitudes, and for 53° physical insight is needed to interpret the result.

The results of the global optimization and the heuristic array design at 26°N are similar for a feasible number of profiles (*e.g.*, $n = 9$) (figure 3.2), but not identical. They mainly differ with respect to placement of profiles close to the MAR. While the global optimization favors profiles at the western boundary, the heuristic array design includes two profiles at each side of the MAR to monitor the sub-basins to the east and the west separately, ensuring to cover a potential pressure drop across the ridge. Although it is known that these two profiles close to the MAR have little influence on the model reconstruction (Marotzke et al., 2002), they were included for dynamical reasons. The model's ability to accurately reproduce real ocean dynamics is limited at this point: in FLAME, the core of the deep western boundary current lies above the depth of the crest of the MAR, while observations show that the core of the deep western boundary current reaches down to greater depths (*e.g.*, Lee et al., 1996). Therefore, the results of the heuristic design ($n = 9$) should be compared to the results of the global optimization for $n = 7$ (figure 3.5f). While the rmse for the timeseries at 1000 m is still significantly smaller for the global optimization (figure 3.3), however, the rmse of the full vertical structure is of comparable magnitude (figure 3.6).

We find that the rmse achievable by observing at the upper limit (every grid point, $n = n_{max}$) at 26°N is about 0.4 Sv (figure 3.3). The quality of the reconstruction for $n = n_{max}$ is closely approximated by the globally optimized array design with less than 10 profiles. However, the rmse for the full vertical structure is for $n \geq 4$ smaller than the rmse for $n = n_{max}$ (figure 3.6). The results of the global optimization should be treated with caution, as it can identify array designs with reconstruction errors below the values achieved by $n = n_{max}$. This property points

to problems introduced by purely optimizing a signal-to-noise ratio, an approach used in optimal detection studies. Here, the velocity field gained from the global optimization does not represent a dynamically meaningful subset of the full velocity field, and in turn, results derived from this subset are not representative of the full dynamics.

Note that the heuristic array design (for $n = 9$) achieves an rmse in the vertical that is smaller than the rmse for $n = n_{max}$. The same is true for the globally optimized array design. While the global optimization array design misses most of the southward flow and captures the variability at 1000 m nearly correctly, the heuristic array design captures about half of the southward flow and captures the variability less well than the global optimization (for $n = 9$). Although it would be desirable to constrain the global optimization to include the mean value and variability of the southward flow, *i.e.* the rmse between the original and reconstructed southward flow, such an optimization would be of limited physical meaning, since all methods do already better than what is achieved with $n = n_{max}$. An additional constraint in the optimization would result in a decreased rmse, which would be even more not representative of the full velocity field, but a subsample incidentally compensating contributions.

Whether the results of a global optimization approach are applicable to a real observing array, depends as much on the setup of the optimization as its subsequent physical interpretation. We show here that global optimization is feasible, and can - for the specific question at hand - immediately yield valuable information on profile placement. The global optimization provides no substitute for an in-depth understanding of the physical mechanisms behind a proposed monitoring array, but can considerably facilitate the process of pre-deployment array design and point to potential methodological problems.

3.5 Conclusions

Based on our analysis of a simulated MOC observing system at 26°N and 53°N in the FLAME model, we conclude:

1. Sequential optimization does not improve on heuristic array design.

2. Global optimization can recover the true global solution for the analyzed array design.

3. At locations where the proposed monitoring strategy does not have the ability to reproduce the MOC at 1000 m, *e.g.*, at 53°N, global optimization finds profiles with lower root mean square errors than the heuristic design, but the suggested setup is not physically meaningful.

4. At locations where the proposed monitoring strategy has the ability to reproduce the MOC at 1000 m, *i.e.* 26°N, global optimization has the potential to yield results of comparable quality as heuristic array design. However, whether the results make physical sense is not guaranteed; the apparent success might merely represent an optimal solution in which misfits compensate each other accidentally.

5. The solution gained from global optimization should be verified in an independent data set, *e.g.* by dividing the data set, to ensure the solution's robustness.

Acknowledgements We wish to thank Joël Hirschi for stimulating discussions. We thank the FLAME group for providing output from their model, and Jens-Olaf Beismann and Lars Czeschel for their help with the model output. This work was supported by the Max Planck Society (JB, JM).

4. DETECTING POTENTIAL MOC CHANGES[1]

Abstract

We analyze the ability of an oceanic monitoring array to detect potential changes in the North Atlantic meridional overturning circulation (MOC). The observing array is 'deployed' into a numerical model (ECHAM5/ MPI-OM), and simulates the measurements of density and wind stress at 26°N in the Atlantic. The simulated array mimics the continuous monitoring system deployed in the framework of the UK Rapid Climate Change program. We analyze a set of three realizations of a climate change scenario (IPCC A1B), in which - within the considered time-horizon of 200 years - the MOC weakens, but does not collapse. For the detection analysis, we assume that the natural variability of the MOC is known from an independent source, the control run. Our detection approach accounts for the effects of observation errors, infrequent observations, autocorrelated internal variability, and uncertainty in the initial conditions. Continuous observation with the simulated array for approximately 60 years yields a statistically significant ($p < 0.05$) detection with 95 percent reliability assuming a random observation error of 1 Sv (1 Sv = 10^6 m^3 s^{-1}). Observing continuously with an observation error of 3 Sv yields a detection time of about 90 years (with 95 percent reliability). Repeated hydrographic transects every 5 years/ 20 years result in a detection time of about 90 years/ 120 years, with 95 percent reliability and an assumed observation error of 3 Sv. An observation error of 3 Sv (one standard deviation) is a plausible estimate of the observation error associated with the RAPID UK 26°N array.

[1] Baehr, J., K. Keller, J. Marotzke (2006): Detecting potential changes in the meridional overturning circulation at 26°N in the Atlantic, *Climatic Change*, in press.

4.1 Introduction

Changes in the Atlantic meridional overturning circulation (MOC) are one of the proposed mechanisms associated with past and future abrupt climate change (*e.g.*, Marotzke, 2000; National Research Council, 2002). Palaeoclimatic records suggest that the ocean circulation has undergone rapid changes in the past 120,000 years, since the Eemian interglacial period (Heinrich, 1988; Dansgaard et al., 1993; National Research Council, 2002; Alley et al., 2003; McManus et al., 2004). Modeling studies have found different responses to anthropogenic climate change, and several model results have suggested that the MOC is potentially sensitive to anthropogenic climate change (*e.g.*, Mikolajewicz and Voss, 2000; Thorpe et al., 2001; Gregory et al., 2005). A weakening or collapse of the Atlantic MOC would entail a reduction in the North Atlantic heat transport, which in turn might lead to significant cooling over the North Atlantic and its adjacent regions (Manabe and Stouffer, 1994; Vellinga and Wood, 2002). The timely detection of MOC changes, and ultimately, timely MOC prediction have the potential to inform the design of climate risk management strategies and decision-making (Keller et al., 2004, 2006b).

The MOC is a function of both latitude and depth. In a numerical model the maximum of the MOC across all latitudes is readily derived from the meridional velocity field, but observations yield information only at the latitude of observation. In the Atlantic, the MOC comprises both a (dominating) buoyancy driven contribution, *i.e.* the thermohaline circulation (THC), and a wind-driven contribution. An observing system is not able to distinguish between these two components, but will be measuring the entire meridional circulation, the MOC.

Observations, commonly hydrographic transects, deliver snapshots of the MOC and the related heat transport at certain latitudes (Hall and Bryden, 1982; Ganachaud and Wunsch, 2000; Bryden et al., 2005). A strategy to monitor the MOC continuously was suggested by Marotzke et al. (1999), using endpoint measurements of the density at the eastern and western boundary of a zonal transect. Two model-based array design studies (Hirschi et al., 2003; Baehr et al., 2004) suggested that this monitoring array is indeed able to capture both the temporal variability and the mean value of the MOC at 26°N in the Atlantic. These studies focused on the main characteristics of the MOC and its short-term variability. Here, we analyze the proposed MOC monitoring strategy with respect to its capability to detect potential long-term MOC changes at 26°N. The simulated array is kept as close as possible to previous studies. It uses the same observing strategy as Hirschi et al. (2003) and Baehr et al. (2004), and mimics the monitoring system deployed in the

framework of the UK Rapid Climate Change program (Marotzke et al., 2002). We restrict our analysis to the 26°N setup, assuming that knowing the MOC at 26°N would provide crucial information about the North Atlantic MOC, its variability and potential changes.

Essentially, we reduce the information delivered by the observing array to a one-dimensional timeseries to simplify the detection task. This approach expands on the study of Santer et al. (1995), who also reduced the dimensionality of the multivariate problem to a few characteristic integral quantities of the ocean circulation. Banks and Wood (2002) used a numerical model to explore the question of where to look for anthropogenic changes in the ocean. Guided by an optimization of the signal-to-noise ratio, they concluded that the MOC or its associated heat transport are unlikely to be useful for the detection of anthropogenic climate change, since this would require a continuous timeseries. Similarly, Vellinga and Wood (2004) used an optimal fingerprint based on a maximization of the signal-to-noise ratio to identify locations for potentially useful ocean hydrographic observations, complementing MOC observations at 26°N in the Atlantic. Two dynamical studies (Hu et al., 2004; Latif et al., 2004) used numerical models to identify simple measures allowing to detect changes in the MOC. All these studies employed numerical models to investigate the mechanisms or general nature of detecting changes in the MOC in the Atlantic, but were not directed at realistic observing systems. In contrast, Keller et al. (2006a) considered the effects of observation error and infrequent observations, analyzing the required frequency of hydrographic transects in the North Atlantic to detect changes in the MOC. In the present study, we simulate a realistic observing system, which was deployed recently (Marotzke et al., 2002; Schiermeier, 2004). The dynamical background of this observing system has been intensively analyzed (Marotzke et al., 1999; Hirschi et al., 2003; Baehr et al., 2004; Hirschi and Marotzke, 2006). We investigate the capability of the observing system to detect changes in the MOC at 26°N. For the detection analysis, one key improvement over previous work is the joint consideration of the effects of observation errors, autocorrelated variability, uncertainty in the model initial conditions, and the reliability of the observing system.

This paper is organized as follows: section 2 provides the details of the numerical model, data set and method used to simulate the MOC observing array. In section 3 two different detection approaches and their results are described. Section 4 discusses these results, and conclusions follow in section 5.

4.2 Model and Method

4.2.1 Model

We use model output from the ocean component of the coupled ECHAM5/MPI-OM general circulation model (Roeckner et al., 2003; Marsland et al., 2003). This coupled model does not require flux adjustments. In the ocean model, the horizontal discretization is realized on an orthogonal curvilinear C-grid (Marsland et al., 2003). The average horizontal resolution is 1.5°. The vertical discretization is on z-levels with 40 non-equidistant levels.

The coupled model's mean state was described in Jungclaus et al. (2006b), using results from an unperturbed control simulation, forced with preindustrial greenhouse gas concentrations. The North Atlantic MOC reaches its maximum of 18.5 Sv (1 Sv $= 10^6$ m^3 s^{-1}) at about 40°N at 1000 m depth, which is comparable to observations (Macdonald, 1998; Ganachaud and Wunsch, 2000). The time averaged Atlantic meridional heat transport has its maximum of 1.15 PW near 20°N. This is within the uncertainty range indicated by Trenberth and Solomon (1994), but smaller than the estimates by Ganachaud and Wunsch (2000) and Talley (2003).

4.2.2 Data

The present analysis is conducted for an unperturbed control simulation and an ensemble of three realizations forced by the the same climate change scenario using the coupled ECHAM5/MPI-OM model. The simulations start from the same spin-up of the model. The control simulation is forced with preindustrial greenhouse gas concentrations, and has a length of 470 years. The climate change experiments are part of a suite of experiments performed for the IPCC Fourth Assessment Report. Starting from different years of the control run, *i.e.*, three different initial conditions, the experiments are all forced with transient greenhouse gas concentrations and aerosol forcing from preindustrial to present day values for the years 1860 to 2000. Subsequently, the IPCC SRES emission scenario A1B (Nakicenovic and Swart, 2000) is used to force the model from 2001 to 2100. In the A1B scenario, the CO_2 concentrations rise from 380 ppmv in the year 2001 to 700 ppmv in the year 2100. The simulations are extended for another 100 years with greenhouse gas concentrations fixed at the levels of the year 2100. Note that this forcing scenario assumes considerable reduction in anthropogenic CO_2 emissions after 2100, compared to many estimates of the business-as-usual scenario. The analyzed timeseries contain 340 years each. The coupled ECHAM5/MPI-OM model shows an increase

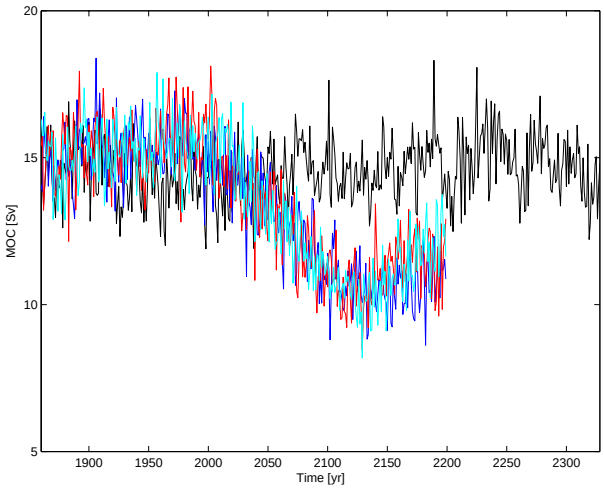

Fig. 4.1: ECHAM5/MPI-OM MOC timeseries at 26°N (1000 m), annual mean values; black: control simulation, blue, red, cyan: IPCC scenario A1B. The time axis indicates the years for the forced runs. The time steps of the control run are not associated with realistic years, although the same time axis is used to display the data.

in global mean temperature of 3.8 K by the year 2100, relative to 1961-1990. The North Atlantic MOC at 30°N weakens for the A1B scenario from 18.5 Sv to about 11 Sv by the year 2100.

At 26°N, the time mean MOC at 1000 m depth is about 15 Sv (Figure 4.1). In the forced runs, the MOC weakens to about 11 Sv starting around the year 2000 (Figure 4.1), but does not collapse within the considered time-horizon of 200 years. Note that the forcing scenario stabilizes the CO_2 concentrations at 700 ppmv in the year 2100. Many simulations show an MOC collapse beyond the 700 ppmv level (Manabe and Stouffer, 1994; Stocker and Schmittner, 1997). The simulations analyzed in this study are silent on the question of how the MOC might respond beyond the considered time scale and forcing scenario.

4.2.3 Simulated MOC Measurements

Our conceptual starting point is the thermal wind relationship, which links zonal density differences to the zonally averaged meridional flow. The stream function of a purely buoyancy-driven MOC can be expressed as a function of latitude and density difference between eastern and western sidewalls and other, independent, parameters (Marotzke, 1997; Marotzke and Klinger, 2000). Marotzke et al. (1999) suggested that, in principle, only the systematic observation of density at eastern and western sidewalls would be required to monitor the MOC continuously. In addition to the

thermal wind component, the full MOC comprises a wind-driven component and a depth-independent component (Lee and Marotzke, 1997). Concerning the MOC in the North Atlantic, the thermal wind and the Ekman contributions are the dominant contributions (Köhl, 2005; Hirschi and Marotzke, 2006). These two contributions are measurable; the thermal wind contribution can be derived from the zonal density difference, and the Ekman contribution can be derived from the surface wind stress. The simulated MOC measurements of Hirschi et al. (2003) and Baehr et al. (2004) employed this decomposition of the MOC, and in addition, the mass balance is closed with a spatially, but not temporally, constant correction (Hall and Bryden, 1982).

Similar to Hirschi et al. (2003) and Baehr et al. (2004) we 'deploy' an MOC observing array into a numerical model at 26°N. The placement of density profiles resembles the existing RAPID UK array with dense coverage of the western and eastern boundary (*cf.* Marotzke et al., 2002). In reality, the meridional transport through the Florida Strait is expected to be measured directly (Larsen, 1985, 1992; Baringer and Larsen, 2001). However, the model resolution does not allow for a representation of the Florida Strait current and the western boundary current separately. To mimic this additional information we extend the region where the meridional transport is assumed to be known over the complete western boundary region. The knowledge of this transport is updated every three months and random, independent, and normally distributed observation errors with a standard deviation of 1 Sv are added; the level of no motion is placed at the bottom of the zonal section (*cf.* Hirschi et al., 2003; Baehr et al., 2004).

All simulated observations are assumed to be taken as monthly means, but except where indicated, annual means are formed, and only these are analyzed. The simulated array is capable of reconstructing the low-frequency, as well as the high-frequency, variability of the MOC, in both the control run (Figure 4.2a) and the forced runs (Figure 4.2b-d). The mean value of the reconstructed MOC is biased by about 4 Sv for both the control run and the forced runs. This offset is nearly constant in time. In the analyzed 340 years it decreases in the forced runs by about 0.5 Sv, whereas no change is apparent in the control simulation.

For the detection analysis, we use normalized timeseries from which the time mean is subtracted. For the control run, the time mean over the complete 470 years of the timeseries is subtracted. For the forced run, the time mean over the first 140 years of the timeseries is subtracted. This approximation seems reasonable, as the detection analysis considers temporal trends, and the temporal variability of the

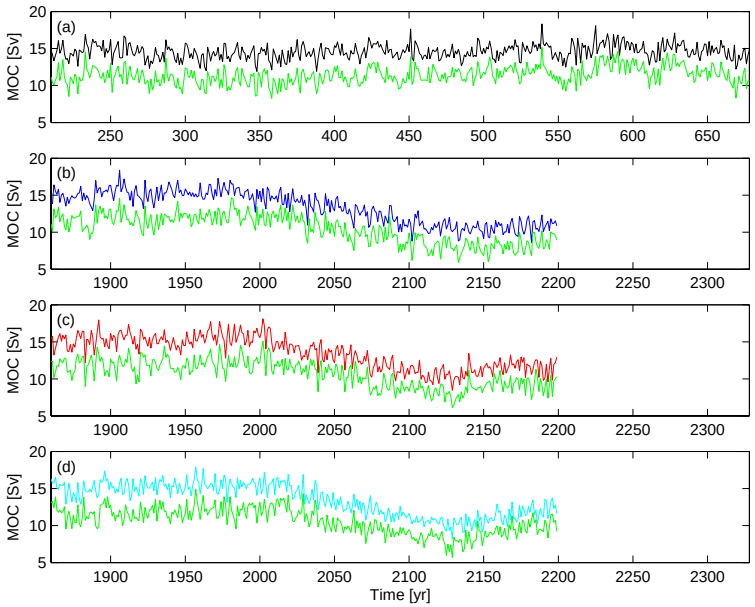

Fig. 4.2: ECHAM5/MPI-OM MOC timeseries at 26°N (1000 m), annual mean values; black: model MOC, green: reconstructed MOC based on the simulated 26°N array. (a) control, (b)-(d) three different realizations of the IPCC scenario A1B.

MOC is reconstructed by the array. In reality, occasional hydrographic sections could be used for calibration.

4.3 Detection Analysis

Initially, we use a continuous timeseries of annual mean values representing the MOC observations at 26°N with no observation error. This timeseries represents an ideal situation for a detection analysis, as it neglects the effects of infrequent observations and observation error (we relax these simplifying assumptions in section 4.3.2.2). The timeseries are analyzed both qualitatively, employing a simple approach, and quantitatively, employing a more refined statistical approach. The two approaches differ mainly in the way the timeseries is handled. The simple approach analyzes a series of individual observations, and tests for at each considered time for a potential change. The quantitative approach analyses a sequence of observations and tests for a linear trend. Both methods come to broadly consistent results for the considered case. We discuss both methods to demonstrate that the statistical analysis largely quantifies what is visible by eye. For the quantitative approach, we will further analyze how observation error, shorter timeseries, and limited observation frequency affect the detection time of MOC changes at 26°N.

4.3.1 Simple Approach

4.3.1.1 Method

One very simple approach to the detection problem analyses a series of observations, representing an unforced system, and additional independent observations, representing a forced system, and asks whether the forced system is outside the range of natural variability given by the unforced system. The lower and upper bounds characterizing the natural variability of the unforced system, the critical values, can be derived in several different ways. For simplicity, we focus here on three possible definitions of these critical values. Other choices of critical values are possible.

The control run is used to provide the natural variability, *i.e.*, the 'observations' of the unforced system. First (*i*), the strictest criterion would be to set the critical value to the lowest value 'observed' in the past, given by the natural range of variability. Second (*ii*), a milder criterion would be to assume that anything lower/higher than two standard deviations of the values 'observed' in the past is critical. Third (*iii*), we assume that anything lower/higher than the lowest/highest 2.5 percent of the values 'observed' in the past is critical. If the considered timeseries were independent draws from a single normal distribution, the critical values (*ii*) and (*iii*) would be virtually identical. Both would approximate the lower and upper bounds of the 95 percent confidence interval of the underlying distribution of the unforced timeseries. The control run, however, violates the assumption of independent draws, we will return to this issue below.

4.3.1.2 Results

For this simple detection approach, the control simulation is used to provide an indication of the natural range of variability of the MOC. The critical values discussed above are derived for both the unforced model MOC and the unforced reconstructed MOC from the simulated array (Figure 4.3). The times at which the respective forced run (shown for one realization only) leaves the lower bound of the given range of natural variability, *i.e.*, detection times, are indicated by the dots above the abscissa in Figure 4.3. For the model MOC, detection occurs around the year 2030 for the critical values (*ii*) and (*iii*), whereas for the critical value (*i*) detection occurs around the year 2060 (Figure 4.3a). Detection prior to the year 2030 is predominantly the result of type-I errors in statistical hypothesis testing, *i.e.*, falsely rejecting the null hypothesis of no change. Adopting the typically used p-value of 0.05 implies a type-I error frequency of 5 percent. More specifically, allowing 5 percent of the values to be outside the critical values results in 5 percent false alarms.

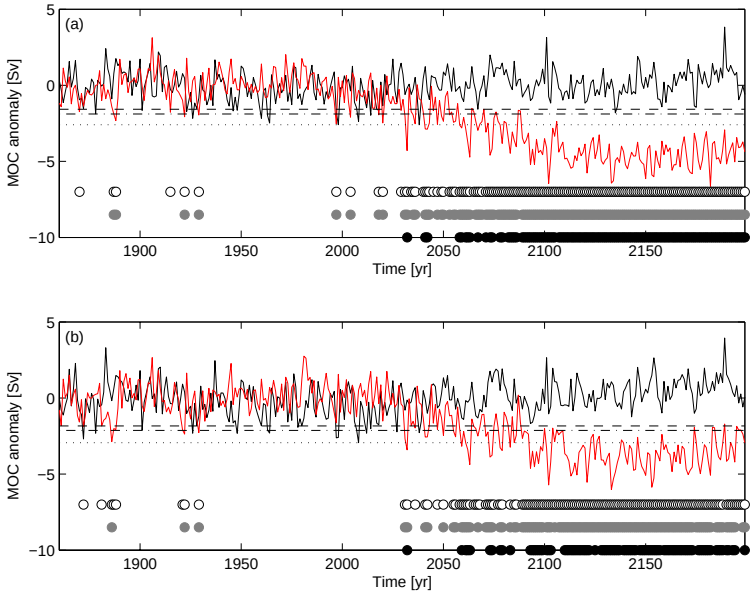

Fig. 4.3: MOC timeseries at 26°N at 1000 m, annual mean values. The horizontal lines indicate different critical values, each derived from the variability of the control timeseries (see text for details). Dots indicate times at which the forced MOC falls below the respective critical value. Three different critical values are shown: (*I*) minimum of the control timeseries (dotted line, black dots), (*II*) lower bound 95 percent confidence level (dash-dotted line, grey dots), (*III*) the lowest/highest 2.5 percent of the values of the entire control timeseries (dashed line, open circle). (a) ECHAM5/MPI-OM, (b) Array reconstruction.

For the reconstructed MOC from the simulated array, detection for the critical value (*i*) occurs around year 2060 (Figure 4.3b), as for the model MOC. For the moderate critical values (*ii*) and (*iii*), detection occurs around year 2035 (Figure 4.3a), which is somewhat later than for the model MOC. The same is found for the two other realizations of the forced run (not shown). The times at which the model MOC and the reconstructed MOC from the simulated array fall below the respective critical value are similar, but in some cases detection occurs for the simulated array up to 10 years later than for the model MOC.

To summarize, the detection times derived from the model MOC and the reconstructed MOC from the simulated array are similar. However, this qualitative analysis does not allow us to make formal statistical statements about the detection capability.

4.3.2 Quantitative Approach

4.3.2.1 Method

We now derive a detection approach that allows us to quantify the detection time of a specific observing system, and therefore allows us to characterize the relationships between detection time, observation error, observation frequency, and the length of observations. First, we use the control simulation to estimate the natural variability of the MOC at 26°N. Second, we test when the forced simulation leaves this range of natural variability.

To estimate the natural variability of the MOC at 26°N, the control run is randomly sampled for a specific length of observation period. Similar to the approach of Santer et al. (1995), the linear trend is estimated for each of these lengths of observation periods, using least squares linear trend estimates. We use overlapping lengths of observation periods with random starting points. We use 10^4 samples for every length of observation period, to yield a numerically stable estimate of the linear trends in the control run. For a given length of observation period, the pdf (probability density function) derived from the linear trends represents the variability of the unforced system. We expand on the method of Santer et al. (1995) by repeating this procedure for a variety of lengths of observation periods, which yields the upper and lower confidence limits of the natural variability, depending on the length of the simulated observations (Figure 4.4). To analyze when the forced simulation leaves the range of natural variability, we estimate the linear trend of the forced simulation, starting in year 2005. Using a single realization of the forced simulation, the linear trends depend only on the length of the simulated observations (Figure 4.4, solid line).

Detection time is a random variable as it depends on random realizations of the observation errors and the internal variability (Keller et al., 2006a). To account for observation error, we add random observation error (identically, independently and normally distributed) of different magnitudes (*e.g.*, standard deviation of 1 Sv) to the simulated observations, and estimate the linear trend of each of the resulting timeseries. Here, random observation errors are added 10^4 times to the timeseries, to yield numerically stable results. We add random observation error to both the unforced and the forced timeseries, assuming that the two timeseries are observations with an inherent observation error, derived from different sources. For simplicity, we assume the same magnitude of observation error for the unforced and forced timeseries.

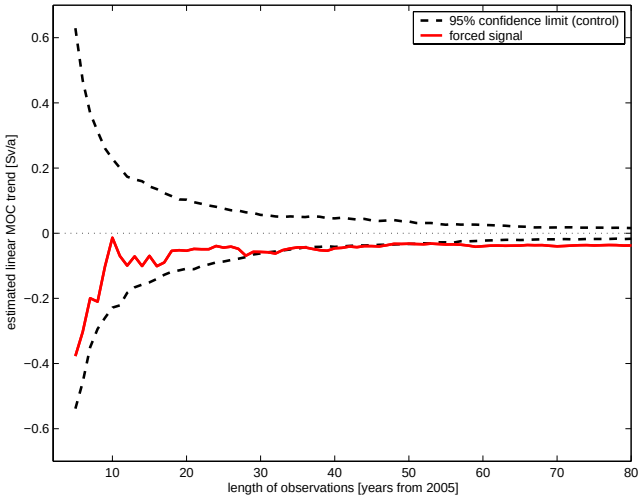

Fig. 4.4: Upper and lower 95 percent confidence limit of the linear trends derived from bootstrap analysis of the control run (dashed line; random starting points), and one realization of the forced run (red line; starting at the year 2005). Both timeseries are annual means with no added observation error. The arrow denotes the time at which the statistically significant trend in the forced run is first detected.

For the unforced timeseries, the upper bound confidence limit derived from analyzing the tail area of the pdf of the linear trends, yields the estimate of the natural variability (depending on the length of observation period and observation error). For the forced timeseries, the linear trends are compared to these confidence limits derived from the unforced run (for the respective length of observation period and observation error): the times at which the linear trend of the forced timeseries with added observation error is outside the confidence limits provided by the unforced timeseries yield an empirical cdf (cumulative distribution function) over a range of lengths of the observation periods, depending on the observation error (Figure 4.5). The upper bound confidence limit derived from analyzing the tail area of this empirical cdf yields the length of observation period at which the forced simulation has left the range of natural variability with $p < 0.05$ (Table 4.1). Following Santer et al. (1995), we refer to this time as the 'detection time'. Note that the median detection time, *i.e.*, detecting with a 50 percent reliability (Table 4.1), is considerably lower than the estimated detection time based on the upper bound 95 percent confidence limit.

Applying this detection method to the control simulation itself, yields a detection frequency of approximately 5 percent. This recovers the value that was used to design the approach, *i.e.*, the type-I error frequency.

Tab. 4.1: Detection times for continuous observations from the model MOC and reconstructed MOC from the simulated array and as a function of the reliability of the detection system. The three numbers represent the three realizations of the forced run.

Observation error	1 Sv	3 Sv	6 Sv	8 Sv
median detection time (50 percent reliability)				
model	34, 10, 27	47, 34, 37	56, 50, 50	53, 52, 50
simulated array	41, 19, 30	47, 43, 39	54, 51, 53	52, 51, 52
upper 95 percent confidence limit detection time (95 percent reliability)				
model	59, 40, 47	99, 92, 81	136, 124, 128	142, 135, 135
simulated array	58, 66, 50	101, 97, 90	136, 130, 130	141, 137, 137

4.3.2.2 Results

MOC Analyzing the forced simulation of the model MOC for an observation error of 1 Sv results in detection times with 95 percent reliability between ∼40 and ∼60 years, depending on the realization (Figure 4.5 a, c and Table 4.1). The median detection time for the equivalent systems is about 30 years smaller than the detection time derived from the upper 95 percent confidence limit (Table 4.1). An increase in the observation error to 3 Sv results in increased detection times of about ∼80 to ∼100 years (95 percent reliability), and between ∼30 and ∼50 years (50 percent reliability). An analysis of the reconstructed MOC timeseries from the simulated array yields similar results: detection with 95 percent reliability for an observation error of 1 Sv yields detection times of about ∼50 to ∼70 years, and for an observation error of 3 Sv yields detection times of about ∼90 to ∼100 years (Figure 4.5 b, d). Larger observation errors of 6 and 8 Sv increase the detection times (with 95 percent reliability) for both the model MOC and the reconstructed MOC from the simulated array to about 135 years (Table 4.1).

The median detection times for small observation errors derived from the quantitative analysis are similar to the detection times derived for the simple analysis (*cf.* Figure 4.3). These median detection times are furthermore comparable to the time at which a single realization assuming no observation error leaves the range of natural variability for the first time (at about 30 years of simulated observations, cf. Figure 4.4). In addition, the detection times derived from the upper 95 percent confidence limit using the quantitative method for small observation errors are similar to the detection time when the single realization assuming no observation error shows a sustained leave of the range of natural variability (at about 60 years of simulated observations, *cf.* Figure 4.4). The results of the two detection approaches differ, because the simple detection approach considers the observations in isolation, whereas the quantitative approach analyses a trend in a sequence of observations.

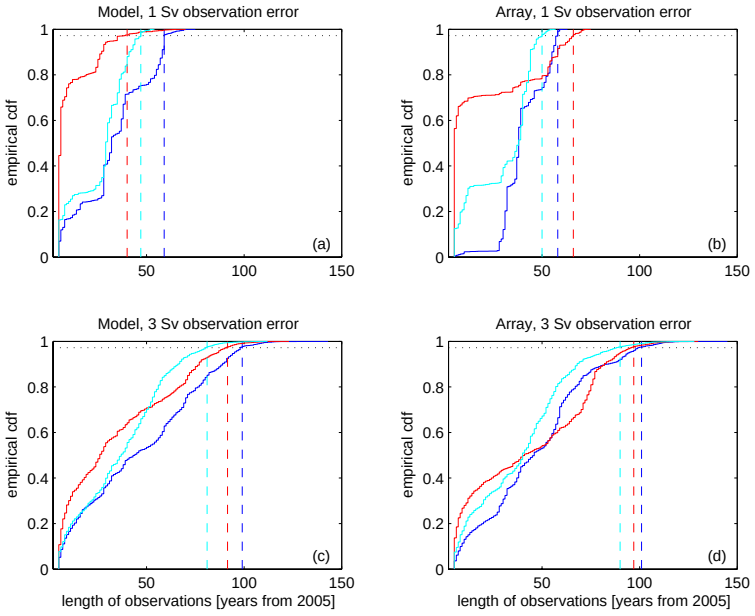

Fig. 4.5: Empirical cumulative distribution function (cdf; that is, the cumulative sum of the probability density function) of the detection times for different observing systems. The three realizations of the forced run are indicated by the different colors. Dashed lines indicate upper 95 percent confidence limit of the detection time. (a) model, observation error 1 Sv, (b) simulated array, observation error 1 Sv, (c) model, observation error 3 Sv, (d) simulated array, observation error 3 Sv.

Previous analysis typically considered a single realization of a model run (*e.g.*, Santer et al., 1995; Vellinga and Wood, 2004; Keller et al., 2006a). Analyzing a single realization neglects the uncertainty due to the initial conditions. As shown in Figure 4.5 and Table 4.1, the effects of different initial conditions on the detection time can be noticeable, on the order of a decade in our example.

Infrequent MOC Observations So far, we only consider continuous observations, using a complete timeseries of annual mean values. Now, we analyze how lowering the observation frequency would influence the detection time. The timeseries of monthly means is subsampled at fixed intervals in years, but the month of the specific year is randomly chosen each time; the resulting timeseries is analyzed in the same way as the timeseries based on continuous observations. To mimic hydrographic transects accurately, we use the timeseries of monthly mean values of the MOC of which the short-term, *i.e.* monthly, variability of the wind-driven circulation is subtracted, but the annual mean of the wind-driven part is kept. The monthly mean MOC at 26°N in ECHAM5/MPI-OM model shows a peak to peak

Tab. 4.2: Detection time (95 percent upper confidence limit) for model MOC, using infrequent observations. The three numbers represent the three realizations of the forced run.

Observation	Observation error			
frequency	1 Sv	3 Sv	6 Sv	8 Sv
continuous	59, 40, 47	99, 92, 81	136, 124, 128	142, 135, 135
every yr	63, 39, 43	95, 87, 76	131, 119, 126	139, 133, 135
every 2 yrs	61, 35, 43	93, 83, 77	119, 113, 115	129, 123, 125
every 5 yrs	61, 61, 66	91, 86, 86	106, 101, 101	111, 106, 106
every 10 yrs	81, 71, 71	91, 91, 91	101, 101, 101	101, 111, 111
every 20 yrs	81, 81, 101	121, 101, 121	121, 121, 121	121, 121, 121

variability of 16 Sv, of which about 6 Sv are purely wind-driven. Subtracting the short-term wind-driven variability is in accordance with procedures analyzing observations, where hydrographic transects are combined with annual mean values of the wind field (*e.g.*, Bryden et al., 2005).

A reduction from continuous observations to frequent hydrographic transects every year or every two years has little effect on the detection time (Table 4.2). Depending on the realization, the detection time increases or decreases by up to about 5 years. One reason for the decrease in detection time is the failure to properly resolve the high-frequency variability with infrequent observations. Reducing the frequency of observations to 10 or 20 years, a frequency which would arguably be feasible with hydrographic observations, yields considerably longer detection times (Table 4.2). Observing with an observation error of 3 Sv every 20 years nearly doubles the detection time compared to continuous observations to about 120 years. Two factors influence this increase in detection time. First, the sparse resolution of the timeseries derived from infrequent sampling is too coarse to yield accurate MOC trend estimates. Second, the annual cycle of the density-driven part of the MOC changes, but hydrographic transects neither resolve the annual cycle of the density-driven part of the MOC nor capture its change. These detection times are even larger when observation errors of 6 Sv or 8 Sv are assumed (Table 4.2): about 120 years assuming a hydrographic transect every 20 years. The estimated detection for the three considered scenarios are not a monotonically increasing function of decreasing observation frequency (Table 4.2). This is not unexpected, due to the stochastic nature of the problem. Observation frequencies of 1 or 2 years are dominated by the short-term variability, whereas observation frequencies like 10 or 20 years capture mainly the long-term trend. Note that this detection analysis assumes a known natural variability, and a start of the simulated observations close to the begin of an MOC weakening. Both assumptions are not necessarily valid for real MOC observing

systems.

Meridional Heat Transport The velocity field derived from the 26°N monitoring array is capable of delivering information beyond a MOC timeseries. The meridional heat transport is arguably one of the key quantities of interest, as the MOC carries most of the oceanic heat transport in the Atlantic (Hall and Bryden, 1982; Ganachaud and Wunsch, 2000). The effect of this northward heat transport of about 1 PW (= 10^{15} W; Ganachaud and Wunsch, 2000) is seen in the resulting relatively mild climate of Western Europe.

The meridional heat transport can be measured, if in addition to the array, a hydrographic transect is undertaken to measure the temperature field. The additional hydrographic transect is necessary to ensure improved spatial coverage of the small scale structure in the temperature field, providing a reliable heat content estimate. Here, we keep the initially 'measured' temperature field constant until new 'observations' are provided, since short term changes in the meridional heat transport are governed by fluctuations in the velocity field rather than the temperature field (Jayne and Marotzke, 2001). Assuming a hydrographic transect every 5 years, and accounting for an observation error of 0.2 PW (*cf.* Ganachaud and Wunsch, 2000) results in a detection time of about 120 years for both the original model heat transport as well as the heat transport derived from the simulated array at 26°N. Lower frequencies of the hydrographic transects (*e.g.*, 10 or 20 years) do not notably increase this detection time in ECHAM5/MPI-OM. However, this insensitivity of the detection time on the frequency of temperature section should be interpreted with caution, since it is likely dependent on the employed model, and its respective resolution. Higher observation errors, up to about 0.5 PW, delay the detection by up to 10 years. The notably larger detection times for the heat transport compared to the MOC arise from the additional influence of the variability in the temperature field combined with the strong internal variability of the ECHAM5/MPI-OM control simulation. Note that this affects the detection time of both the reconstructed heat transport from the simulated array and the model heat transport similarly.

4.4 Discussion

In the present study, we test whether a timeseries derived from simulated measurements of the MOC at 26°N is capable of detecting changes in the MOC. Currently, the detection of MOC changes is based on a very limited amount of information: *e.g.*, snapshots of the MOC at certain latitudes (*e.g.*, Bryden et al., 1996, 2003,

2005), results from data assimilation for about a decade (*e.g.*, Stammer et al., 2003; Wunsch and Heimbach, 2006), or hindcats estimates (*e.g.*, Marsh et al., 2005). However, a statistically rigorous method would have to be based on more information than is available from current observing systems, since robust detection depends on the additional knowledge of the natural variability of the system (*e.g.*, Santer et al., 1995). This challenge is inherent to all climate change detection studies, and a refined analysis of the historic observations of the MOC at 26°N (Longworth et al., 2005), or more generally the palaeo-record (*e.g.*, Keigwin and Boyle, 2000), might be a promising step towards this goal (Keller et al., 2006b).

In our analysis, we estimate the detection time for a range of observation errors. It is difficult to assess, which of these chosen observation errors would be a reasonable approximation to real observations. Ganachaud (2003) estimated the observation error for integrated transports derived from hydrographic transects as approximately 3 Sv (one standard deviation), similar to the error assumed here. Ganachaud (2003) attributed this error mainly to uncertainties due to unknown temporal variability. The observation error of MOC estimates based on the RAPID UK 26°N array is not yet known. The temporal resolution of the array data should, however, allow us to reduce the uncertainties due to the unknown temporal variability of the MOC. A careful assessment of errors in the observed MOC (and associated properties) is crucial for the tasks of MOC change detection, prediction, and the design of observation systems.

An inherent limitation to the transferability of our results is the dependence on the particular model employed. In ECHAM5/MPI-OM, the annual mean MOC at 26°N exhibits a variability from peak to peak of about 4 Sv. This is comparable to results given by other coupled models (Gregory et al., 2005). We use three realizations and find that the results are robust across these three realizations. The actual variability of the MOC is, at this time, uncertain due to the sparse spatiotemporal nature of the available observations.

We have tested our approach with monthly values instead of annual means. Note that in the ECHAM5/MPI-OM model the MOC without short-term wind-driven variability exhibits a peak to peak variability of about 10 Sv arising from fluctuations in the density field. This results in a small signal-to-noise ratio, especially in combination with the weak decline in the ECHAM5/MPI-OM solution. If unsmoothed monthly mean data are used, no detection occurs within the considered time horizon of 200 years, for either the model MOC or the reconstructed MOC from the simulated array (results not shown). Evidently, this changes considerably

if the monthly mean timeseries is smoothed or averaged. However, both techniques require a continuous timeseries, with a high temporal resolution.

The array simulated in the present study assumes continuous observations. Similar to Keller et al. (2006a) we also analyze how less frequent hydrographic sections influence the detection time. Keller et al. (2006a) found that an observing system consisting of a hydrographic transect every 5 years and an observation error of about 3 Sv results in a median detection time of approximately 70 years. Our results are broadly consistent with the findings of Keller et al. (2006a), who use a different model run (Manabe and Stouffer, 1994) and a different statistical detection method. For an observation error of 3 Sv, the median detection time of continuous or infrequent observations (up to observing every 10 years) is within a century in our analysis. But we find, in addition, that observing continuously with an observation error of 1 Sv reduces the 95 percent reliability detection time considerably, in our model to about 40 to 60 years.

The analysis, so far, indicates that establishing a continuous MOC observing system at 26°N lasting for decades has the potential to reduce the currently large uncertainty about the MOC response to anthropogenic forcing. One might ask whether the necessary investments would pass an economic cost-benefit test, as hypothesized by Adams et al. (2000). Previous economic analysis showed that reducing key uncertainties about the impacts of anthropogenic greenhouse gas emissions may allow for economically more efficient strategies of climate risk management and have hence the potential for a positive expected economic value of information (Yohe, 1991; Peck and Teisberg, 1996; Yohe, 1996; Nordhaus and Popp, 1997; Keller et al., 2006a). Keller et al. (2006a) showed that the expected economic value of information of an MOC observing system that would deliver an actionable early warning sign of MOC changes within the next few decades can far exceed the necessary costs.

It is important to recognize, however, that estimates of the economic value of information are an area of active research and hinge on a range of simplifying assumptions. Keller et al. (2006a), for example, approximated the decision problem as a binary system. Specifically, the MOC is either insensitive to anthropogenic forcing or sensitive. In addition, the decision-maker chooses between two options: no control of CO_2 emissions or reducing CO_2 emissions such that an MOC collapse is avoided in the sensitive case. In this situation, detecting an MOC change is equivalent to predicting the binary MOC response. In addition, Keller et al. (2006a) adopted a simple decision-criterion (expected cost-minimization) and published estimates of the economic impacts of MOC collapse. These assumptions may be reasonable first-order

descriptions of the decision-making process, but ignore the effects of (*i*) structural model uncertainty, (*ii*) a more refined sampling of the parametric uncertainty, and (*iii*) alternative decision criteria (Lempert, 2002).

Given these caveats, the investments into a decadal-scale and continuous MOC observation array at 26°N has the potential to pass a very simple economic cost-benefit test: the costs of the array are on the scale of 1 million US dollars per year and tens of millions over decades, compared to an expected economic value of information on the order of billions US dollars. The 26°N array has smaller costs than the ones considered in Keller et al. (2006a). In addition, the 26°N array provides MOC observations with higher temporal resolution and higher expected accuracy than hydrographic sections, the observing system analyzed in Keller et al. (2006a).

The observations provided by the RAPID UK 26°N array deliver a two dimensional picture of the zonal transect at 26°N, which contains more information than just a one-dimensional timeseries. Applying multivariate fingerprint analysis (Santer et al., 1995; Hasselmann, 1998) has the potential to result in shorter detection times. The focus of the present study is to demonstrate, as a first step, the ability of the 26°N array to detect changes in a single timeseries, the MOC at 26°N, if the unforced variability is known. A multivariate analysis is left for future study.

4.5 Conclusions

Based on our analysis of a simulated MOC observing array in the particular solutions of ECHAM5/MPI-OM, and our univariate analysis assuming, most notably, that we have independent knowledge of the variability of the unforced system, we conclude:

1. Observation periods of less than 20 years carry a high probability to result in false alarms, *i.e.*, detection times similar to the type-I error frequency used in designing the method.

2. Detecting MOC changes at 26°N with a reliability of 95 percent requires decades to a century of continuous observations, depending on the observation error.

3. For an observation error of 1 Sv, continuous observations result in a detection time of approximately 60 years (with 95 percent reliability). For an observation error of 6 Sv, the 95 percent reliability detection time exceeds a century.

4. Continuous observations, hydrographic sections every 5 years, and hydrographic sections every 20 years result in detection times of about 100 years, 90 years, and 120 years, respectively, for an observation error of 3 Sv, and for a 95 percent reliability.

5. Changes in the meridional heat transport at 26°N can be detected with a detection time of about 120 years (95 percent reliability), assuming an observation error of about 0.2 PW, and additionally assuming a hydrographic transect every 5 years.

6. For a given desired reliability in detecting MOC changes at 26°N, a continuous observing system is less expensive than repeat hydrographic sections.

Acknowledgements We thank Michael Botzet and Johann Jungclaus for help with the ECHAM5/MPI-OM output and Joël Hirschi for stimulating discussions. Robin Smith, Carl Wunsch and the two reviewers provided valuable comments on the manuscript. This work was supported by the Max Planck Society (J.B., J.M.) and the National Science Foundation (SES # 0345925, K.K.). Any opinions, findings, and conclusions or recommendations expressed in this material are those of the authors and do not necessarily reflect the views of the funding agencies.

5. TIMELY DETECTION OF MOC CHANGES[1]

Abstract

It is investigated how changes in the North Atlantic meridional overturning circulation (MOC) might be reliably detected within a few decades using the observations provided by the RAPID-MOC 26°N array. Previously, the investigation of detectability of MOC changes had been based on a single integrated transport time-series, exhibiting strong internal variability which would prohibit the detection of MOC changes within a few decades. Here, the observed variability of water mass properties along the transatlantic section at 26°N is first compared to a control climate simulation of the coupled ECHAM5/MPI-OM global model. The observed differences in temperature and salinity found between the 1957 and the 2004 occupations of the section are similar to the anomaly patterns found in the model when regressing temperature and salinity against the strength of the MOC. Most notably, the lower North Atlantic Deep Water is cooler and fresher with weaker MOC, while intermediate and thermocline waters are more saline. The results suggest that the observed changes in temperature and salinity between 1957 and 2004, can be associated with variations of the MOC of several Sverdrups, which are within the range of the model's natural variability. For the detection analysis, three realizations of the IPCC (Intergovernmental Panel on Climate Change) scenario A1B are analyzed, in which the MOC weakens by approximately 25 percent in the 21st century. In these simulations, the zonal mean temperature at 26°N is dominated by the global warming signal, and salinity at 26°N increases. Short-term changes in the MOC are, in contrast, associated with changes in the zonal density gradient. A fixed spatial pattern of natural variability is derived from the observations and used to investigate at which time the zonal density gradient in the climate change scenario departs from the given range of natural variability. For a random observation error of 0.01 kg m^{-3}, and only using zonal density gradients between 1700 m and 3100 m depth, statistically significant detection occurs with 95 percent reliability after about 30

[1] Baehr, J., H. Haak, S. Alderson, S. A. Cunningham, J. H. Jungclaus, J. Marotzke (2006): Timely detection of changes in the meridional overturning circulation at 26°N in the Atlantic, *Journal of Climate*, submitted.

years. Compared to using a single MOC timeseries as detection variable, continuous observations of zonal density gradients reduce the detection time by 50 percent.

5.1 Introduction

Numerous studies have analyzed the problem of detecting anthropogenic climate change (*e.g.*, The International Ad Hoc Detection and Attribution Group, 2005). Most of these efforts have focused on air temperature observations, predominantly surface air temperature, but some studies have analyzed the vertical structure of temperature in the atmosphere. In contrast, a rigorous detection analysis of oceanic quantities has found considerably less attention. Notable exceptions are Santer et al. (1995), who conducted a univariate and multivariate detection study for several - integrated - ocean variables, Barnett et al. (2001) and Reichert et al. (2002), who analyzed global ocean heat content, and Banks and Bindoff (2003), who analyzed temperature and salinity changes in the Indo-Pacific.

One of the quantities eminently associated with past and future climate change is the oceanic meridional overturning circulation (MOC) (National Research Council, 2002), the zonally and vertically integrated meridional flow as a function of latitude and depth. Several modeling studies suggest that the MOC is potentially sensitive to anthropogenic climate change (Manabe and Stouffer, 1994; Mikolajewicz and Voss, 2000; Thorpe et al., 2001; Gregory et al., 2005). A weakening or collapse of the Atlantic MOC is expected to entail a reduction in the North Atlantic heat transport, leading to a significant cooling over the North Atlantic and its adjacent regions (Manabe and Stouffer, 1994; Vellinga and Wood, 2002).

Ship-based transoceanic sections yield the most reliable observational estimates of the MOC (*e.g.*, Hall and Bryden, 1982; Ganachaud and Wunsch, 2000; Bryden et al., 2005), but deliver snapshots only. Recently, an observing array to monitor the MOC at 26°N in the Atlantic was deployed (Marotzke et al., 2002; Schiermeier, 2004). This RAPID-MOC array is based on the Marotzke et al. (1999) conceptual study, suggesting that the MOC could be continuously monitored using endpoint measurements of the density at the eastern and western boundaries of a zonal transect. Prior to deployment, the array was tested in two numerical models (Hirschi et al., 2003; Baehr et al., 2004), showing that such an array could be capable of capturing both the mean value of the MOC as well as the short-term variability. Whether the RAPID-MOC array is capable of detecting long-term trends was studied by Baehr et al. (2006), suggesting that it takes several decades to detect a MOC change based on a single MOC timeseries.

More generally, potential MOC changes were considered in the framework of a rigorous detection analysis: Vellinga and Wood (2004) used an optimized fingerprint to identify suitable locations for supplementing the 26°N RAPID-MOC array to improve the detection times for MOC changes. Keller et al. (2006a) used a formal detection algorithm to detect changes in the maximum MOC in the Atlantic. Baehr et al. (2006) analyzed a univariate MOC timeseries, simulating observations delivered by the RAPID-MOC array. Further, Brennan et al. (2006) used a hydrographic tracer (oxygen) to improve the MOC's signal-to-noise ratio. Santer et al. (1995), Banks and Wood (2002), Vellinga and Wood (2004), and Baehr et al. (2006) found that the detection times on a univariate MOC timeseries are on the order of several decades to a century. Thus, Santer et al. (1995), Barnett et al. (2001), and Banks and Wood (2002) suggested that the (multivariate) analysis of sub-surface structures generally have the potential to deliver shorter detection times.

Several (observable) quantities have been proposed to deliver information about MOC changes with a higher signal to noise ratio than the actual meridional transports (*e.g.*, Hu et al., 2004; Latif et al., 2004; Levermann et al., 2005; Lohmann et al., 2006). These studies - as the present one - shared the difficulty of having to disentangle the change in a certain property and MOC changes. They did not consider the observation of transport series, but the observation of the chosen property, thus relying for the link between MOC changes and the change in a certain property on a numerical model.

Here, we present a detection variable for the MOC at 26°N, which (*i*) is solely based on observable quantities, *i.e.*, the zonal density gradient at 26°N, and (*ii*) provides timely detection of MOC changes, *i.e.*, faster detection than when relying on an MOC timeseries alone. More specifically, we simulate observations, as a substitute for ongoing and future observational efforts, to test whether the 26°N RAPID-MOC observing array has the potential to deliver timely information about future MOC changes. In contrast to earlier studies (*e.g.*, Santer et al., 1995; Baehr et al., 2006), we use a detection variable that takes the spatial structure of the simulated observations into account. The derivation of a suitable detection variable follows to a large extent the methodology established by Hasselmann (1979, 1993) and Hegerl et al. (1996), although we deviate from it: we project (simulated) observations onto an observable pattern (model-based, but confirmed against observations) that represents natural variability, in contrast to projecting observations on a model-based pattern that represents an assumed future change. The formal estimation of the detection time follows the approach of Santer et al. (1995), with the modifications used by Baehr et al. (2006).

This paper is organized as follows: In section 2, we describe the observations and model output used in the present study. Section 3 focuses on the comparison of hydrographic observations and model output. Section 4 describes the detection method and the resulting detection times. In section 5, we discuss the results, and conclusions are given in section 6.

5.2 Data

5.2.1 Observations

The 24.5°N transatlantic section has been occupied five times in 1957, 1981, 1992, 1998, and 2004 (Fuglister, 1960; Roemmich and Wunsch, 1985; Parrilla et al., 1994; McTaggert et al., 1999; Cunningham, 2005). For these five occupations, we calculate the detection variables, following the same procedure as for the model output. Further, we compare directly the 1957 and 2004 occupations. The five occupations were closed at different latitudes (*cf.*, Cunningham and Alderson, 2006). For the analysis of the 2004 occupation, additional long-term current meter measurements of the Deep Western Boundary Current (DWBC) were available (Lee et al., 1990, 1996; Fillenbaum et al., 1997; Bryden et al., 2006).

The 1957 data were obtained from discrete water samples at approximately 25 depths, while from 1981 onward temperature and salinity profiles were obtained from conductivity-temperature-depth (CTD) stations with discrete salinity samples being measured against standard seawater, and used for calibration of the CTD salinities. The 1957 salinities are between 0.004 and 0.006 higher than the salinities in the subsequent years (Bryden et al., 1996; Arbic and Owens, 2001). This systematic salinity error makes comparisons of the 1957 salinities to other salinities unreliable below 2000 dbar (Arbic and Owens, 2001), but the qualitative characteristics of intermediate and thermocline waters are unaffected.

5.2.2 Model Description and Analyzed Output

In the present study, we use model output from the coupled ECHAM5/MPI-OM global climate model (Roeckner et al., 2003; Marsland et al., 2003). The atmospheric component ECHAM5 is coupled to the ocean component MPI-OM, and no flux adjustments are applied. ECHAM5 is realized at T63 resolution with 31 vertical levels. MPI-OM is realized on an orthogonal curvilinear C-grid (Marsland et al.,

2003). The northern grid pole is shifted to Greenland, avoiding the singularity at the geographical North Pole. MPI-OM's average horizontal resolution is about 1.5°, varying between 12 km close to Greenland and 180 km in the tropical Pacific. The vertical resolution is realized on 40 non-equidistant z-levels, of which 20 are distributed over the top 700 m. The bottom topography is resolved by partial grid cells. Jungclaus et al. (2006b) described the coupled model's ocean mean state, based on an unperturbed control simulation and forced with preindustrial greenhouse gas concentrations.

We analyze model output of ECHAM5/MPI-OM's ocean component from a control simulation and an ensemble of three realizations forced by the same climate change greenhouse gas scenario. The unperturbed control simulation has a length of 460 years, and applies preindustrial greenhouse gas concentrations. The climate change experiments are part of a suite of experiments performed for the IPCC (Intergovernmental Panel on Climate Change) Fourth Assessment Report. The three realizations start from from different years of the control run, and have a length of 340 years each. For the years 1860 to 2000, the simulations are forced with observed greenhouse gas concentrations and aerosol concentrations from preindustrial to present-day values. For the years 2001 to 2100, the simulations are forced with greenhouse gas concentrations based on the IPCC SRES emission scenario A1B (Nakicenovic and Swart, 2000); CO_2 concentrations rise from 380 ppmv in the year 2001 to 700 ppmv in the year 2100. Over the same period, global mean surface temperature rises by 3.8 K by the year 2100, relative to 1961-1990. The North Atlantic MOC at 30°N weakens in the A1B scenario from 18.5 Sv to about 11 Sv by the year 2100 (Jungclaus et al., 2006a). For the years 2101 to 2199, the simulations apply greenhouse concentrations fixed at the levels of the year 2100.

5.2.3 Simulation of Monitoring Array

We 'deploy' an oceanic monitoring system into the numerical model ECHAM5/MPI-OM, allowing us to test various characteristics of the simulated observations. The observing system simulated here resembles the existing RAPID-MOC array at 26°N in the Atlantic (Marotzke et al., 2002). We simulate the continuous measurement of density, with intensified coverage of the eastern and western boundaries (Rayner, 2005). The resulting density gradients are used to infer meridional transports (Hirschi et al., 2003; Baehr et al., 2004). The dynamical background of the observing array has been extensively analyzed in Marotzke et al. (1999); Hirschi et al. (2003); Baehr et al. (2004); Hirschi and Marotzke (2006). The setup employed in the present study is identical to the one used in Baehr et al. (2006). All simulated

measurements are assumed to be taken as monthly means, but annual means are formed, and only these are analyzed.

5.3 Results from Data - Model Comparison

Comparing hydrographic observations and model simulations, we derive a fixed spatial pattern of natural variability, form in turn a range of natural variability is derived. Subsequently, we use this range of natural variability to determine when a significant change in the simulated observations of a climate change scenario can be detected.

5.3.1 Observations vs Model

First, we compare directly the 1957 and 2004 hydrographic observations of the 26°N transect, similarly to Cunningham and Alderson (2006). Specifically, we compare the differences in potential temperature and salinity between the two occupations (2004 - 1957) for the eastern and western boundaries, and the zonal mean (figure 5.1). Most notably, intermediate and thermocline waters become warmer and more saline, while the lower North Atlantic Deep Water (NADW) cools and freshens. These changes are more pronounced at the western boundary. The difference in meridional transports associated with this temperature and salinity difference is a decrease of the northward transport shallower than 1000 m by about 8 Sv, and a decrease in the southward transport between 3000 m and 5000 m depth of about 8 Sv (Bryden et al., 2005).

A regression analysis of the temperature and salinity fields in the ECHAM5/MPI-OM control simulation versus the strength of the MOC at 1000 m depth in the same ECHAM5/MPI-OM control simulation reveals similar anomaly patterns (figure 5.2). Here, we multiply the anomaly patterns of the regression analysis by -8 Sv, *i.e.*, the transport variability inferred from the observed temperature and salinity fields (Bryden et al., 2005). The standard deviation of the MOC in the control simulation is about 1 Sv (for annual mean values).

In both the observed and modeled temperature anomalies a weakening of the MOC is associated with a warming of the intermediate waters, mostly at the western but also at the eastern boundary (figures 5.1 and 5.2). Similarly, intermediate waters become significantly saltier at the western boundary, and - to a lesser extent - at the eastern boundary. The upper North Atlantic Deep Water (NADW) becomes

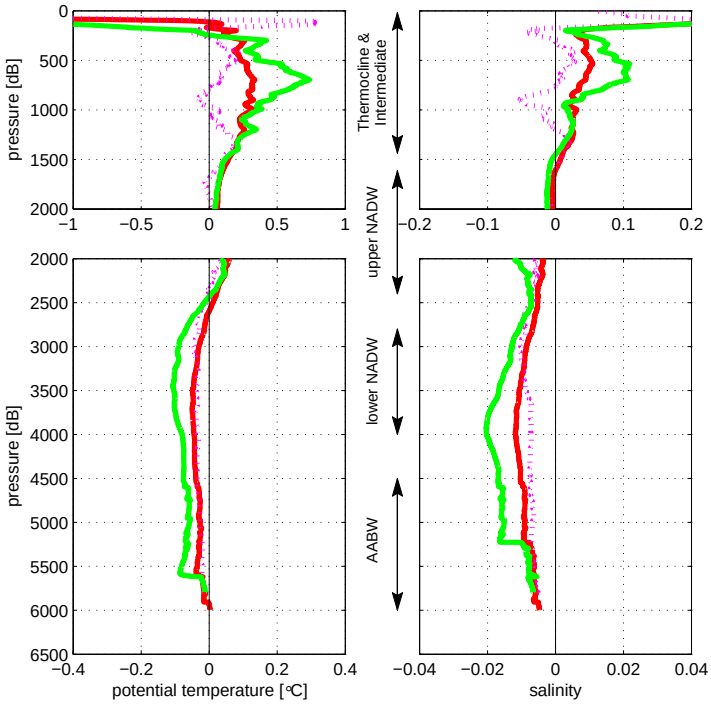

Fig. 5.1: Observed potential temperature (left) and salinity (right) difference between the 2004 and the 1957 occupations. The western boundary extends from 65°W to 75°W (green), the eastern boundary from 25°W to 35°W (red), and the zonal average from 15°W to 100°W (magenta, dotted).

slightly warmer, while the lower NADW cools and freshens. Note that in the model, the NADW starts at a shallower depth, and upper and lower NADW are not readily distinguished. In the model, an MOC decrease is associated with higher temperature and salinity below 2500 m depth, while the observed anomalies indicate cooling and freshening. At the surface, the profiles based on the regression do not seem to be very reliable due to the high variability of the surface waters, and the fact that the regression is done versus the strength of the MOC at 1000 m depth. Although the modelled and observed temperature and salinity fields differ in the deeper ocean, the differences have somewhat compensating effects on density. In summary, comparing the temperature and salinity patterns associated with MOC variability in both the observations and ECHAM5/MPI-OM's control simulation shows similar anomaly patterns. The results suggest that the observed changes in temperature and salinity can be associated with variations in the MOC, which are within the model's range of natural variability. We therefore use the temperature and salinity fields resulting from a regression with the MOC in the control simulation to describe the range of natural variability.

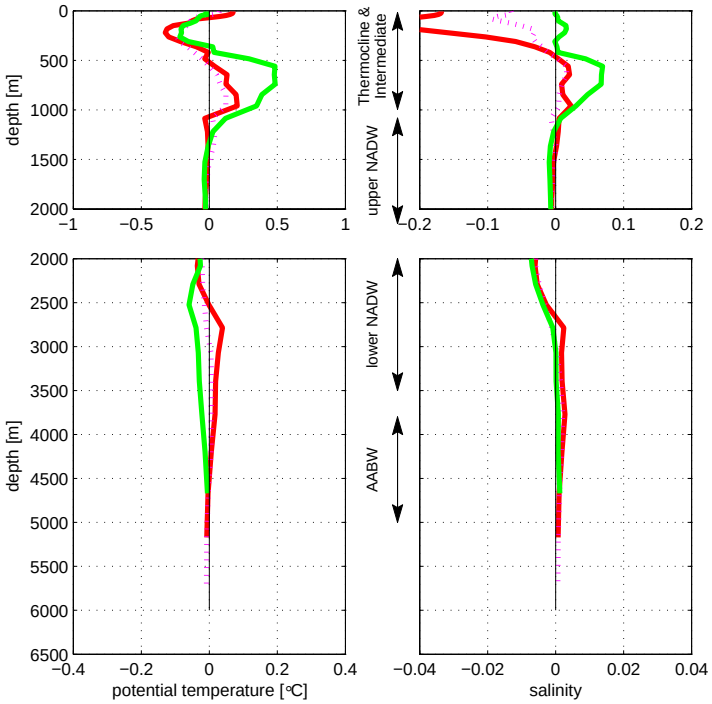

Fig. 5.2: Modeled potential temperature (left) and salinity (right) anomaly patterns of regression against MOC in the ECHAM5/MPI-OM control simulation, multiplied by -8 Sv, *i.e.*, the transport variability inferred from the observed temperature and salinity fields (Bryden et al., 2005). The western boundary extends from 70°W to 80°W (green), the eastern boundary from 26°W to 36°W (red), and the zonal average from 15°W to 80°W (magenta, dotted).

5.3.2 Selection of a Suitable Quantity for Detection

Having analyzed MOC variability and its relation to temperature and salinity variations in the control simulation, we investigate how this relation behaves under a climate change scenario, aiming to identify a suitable variable for the detection of MOC changes at 26°N.

Under the employed climate change scenario, temperature and salinity characteristics at the eastern and western boundaries change considerably (figure 5.3). At the western boundary, thermocline and intermediate waters become warmer and more saline (figure 5.3a), while at the eastern boundary, thermocline and intermediate waters become warmer, but not generally more saline (figure 5.3b). Changes are less pronounced in the deep ocean. Overall, analyzing the eastern and western boundaries independently of each other yields predominantly the global warming signal (for both the eastern and the western boundary, and for temperature as well as salinity, *i.e.*, the water becomes more saline). Changes in the zonally average tem-

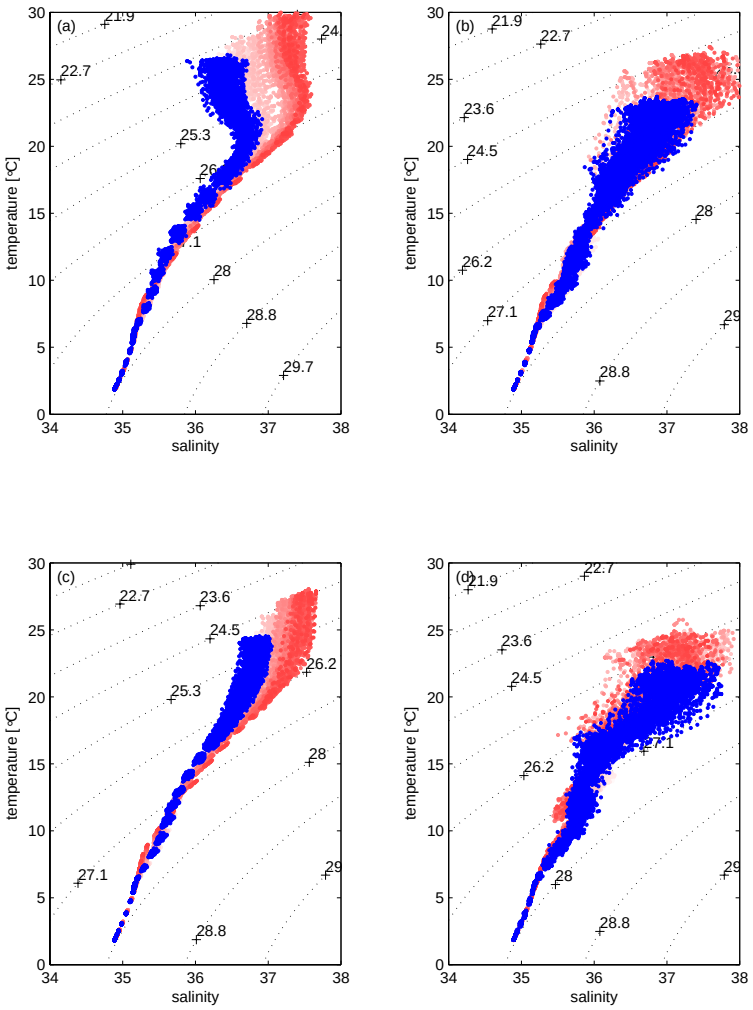

Fig. 5.3: T-S Diagrams for control simulation (blue) and global warming simulation (red): (a) western boundary, (b) eastern boundary, (c) zonal mean, (d) eastern boundary minus western boundary plus vertical profile of time-mean difference. Shading of red markers indicates time, the darker the shading the later the timestep. The western boundary extends from 70°W to 80°W, the eastern boundary from 26°W to 36°W, and the zonal average from 15°W to 80°W.

perature and salinity fields are dominated by the influence of the western boundary; thermocline and intermediate waters become warmer and more saline, which is again the global warming signal (figure 5.3c).

Detecting changes in the MOC requires a careful differentiation between density changes related to an MOC change, and unrelated density changes. Aiming to identify a suitable variable for the detection of MOC changes, we analyze the zonal density difference (figure 5.3d), changes in which are intimately linked to changes in the MOC. If the flow is everywhere in thermal wind balance, *e.g.* in the presence

of vertical sidewalls, the vertical structure of the MOC is proportional to the east-west density difference. Based on this relationship, Marotzke (1997) and Marotzke and Klinger (2000) developed the theory of a purely buoyancy-driven flow. The presence of wind forcing and irregular bottom topography, *i.e.* more realistic circumstances, leads to a time-varying Ekman contribution (Lee and Marotzke, 1998; Jayne and Marotzke, 2001) and the external mode (Robbins and Toole, 1997; Lee and Marotzke, 1998), respectively, neither of which is in thermal wind balance. However, Köhl (2005) and Hirschi and Marotzke (2006) showed that the thermal wind and the Ekman contribution are the dominant contributions to the MOC in the North Atlantic. Density anomalies influence the meridional transports, once the anomalies reach the boundaries of the basin (Marotzke et al., 1999), suggesting that the density changes close to the ocean margin are sufficient to capture the basin-wide velocity shear (Hirschi and Marotzke, 2006). Further, the zonal density difference is less influenced by the direct global warming signal: changes in the zonal density difference occur throughout the watercolumn (figure 5.3d). In the following, we will therefore use the zonal density difference as a measure of the strength of the MOC.

5.4 Detection Analysis

The RAPID-MOC array provides continuous measurements of density gradients and related meridional transports. It has not been established whether these measurements allow for a timely detection of MOC changes: an analysis based on a univariate MOC timeseries suggests that detection times might be in the order of several decades to a century, depending on the observation error (Baehr et al., 2006). Note that - following Santer et al. (1995) - 'detection time' indicates the earliest time at which an anthropogenic change can be detected with statistical significance ($p < 0.05$).

5.4.1 Detection Method

In contrast to the univariate analysis of Baehr et al. (2006), a multivariate analysis that includes the two-dimensional spatial information provided by the RAPID-MOC array, has the potential to result in earlier detection. A multivariate analysis requires, first, the derivation of a univariate detection variable and, second, to quantify the detection time. We derive a detection variable following Hasselmann (1979, 1993) and subsequently perform a formal detection analysis following Santer et al. (1995), as modified by Baehr et al. (2006).

5.4.1.1 Detection Variable

Hasselmann (1979) proposed to project a multi-dimensional detection space onto a smaller number of variables by forming a scalar product with fixed spatial patterns. Hasselmann (1979, 1993) discussed the multi-fingerprint case, whereas Hegerl et al. (1996) discussed a simplified version of Hasselmann's technique for a single fingerprint. The climate change signal, a space-time-dependent variable, is considered as the climate vector $\mathbf{\Psi}$ in the detection space. In the notation of Hegerl et al. (1996), the single scalar-detection variable d is a result of projecting $\mathbf{\Psi}$ onto a suitably chosen fingerprint $\mathbf{f}$: $d = \mathbf{f}^{\mathrm{T}}\mathbf{\Psi}$, with the fingerprint $\mathbf{f}$ representing the expected pattern of climate change. In contrast to Hasselmann (1979, 1993), Barnett (1991) and Hegerl et al. (1996), we project the selected variable of the climate vector $\mathbf{\Psi}$ (denoted $\mathbf{\Psi_f}$ to indicate the forced simulation) onto an - observable - fixed spatial pattern of natural variability $\tilde{\mathbf{N}}$, yielding the detection variable d_f for the forced simulation:

$$d_f(t) = \tilde{\mathbf{N}}^{\mathrm{T}}(x,z)\mathbf{\Psi_f}(t,x,z). \tag{5.1}$$

$\mathbf{\Psi_f}(t,x,z)$ consists of the values of a selected variable depending on time (t), the longitude (x), and the vertical (z) dimension. If the resulting $d_f(t)$ exhibits no trend, the observed climate signal is within the given range of natural variability, whereas a trend in $d_f(t)$ indicates a deviation of the observed climate signal from the natural variability.

In the present study, the climate vector $\mathbf{\Psi_f}(t,x,z)$ is represented as the density field $\rho_f(t,x,z)$, measured by the RAPID-MOC monitoring array along the zonal transect at 26°N: $\mathbf{\Psi_f}(t,x,z) = \rho_f(t,x,z)$. We use an uncentered signal with respect to the spatial signature, *i.e.*, without subtracting the spatial mean, but we subtract the time-mean of the control simulation.

5.4.1.2 Fixed Spatial Pattern of Natural Variability

The fixed spatial pattern of natural variability $\tilde{\mathbf{N}}$ is represented by a regression between the simulated density measurements, $\rho_c(t,x,z)$, and the strength of the MOC, $MOC_c(t)$, both within the control simulation with n_t timesteps, where the overbar marks the time-average:

$$r(x,z) = \frac{\sum_{t=1}^{n_t}\left[MOC_c(t) - \overline{MOC_c}\right]\left[\rho_c(t,x,z) - \overline{\rho_c(x,z)}\right]}{n_t \cdot \mathrm{var}(MOC_c)}. \tag{5.2}$$

The resulting regression coefficient $r(x,z)$ is multiplied by the standard deviation of the MOC, σ_{MOC_c}:

$$\tilde{\mathbf{N}}(x,z) = r(x,z) \cdot \sigma_{MOC_c}, \tag{5.3}$$

yielding the estimated fixed spatial pattern of natural variability $\tilde{\mathbf{N}}(x,z)$, *i.e.*, the part of the density field related to MOC variability. Note that we normalize the fixed spatial pattern of natural variability $\tilde{\mathbf{N}}$ to unity before computing the detection variable. For the employed model, $\tilde{\mathbf{N}}$ was shown to be comparable to observations (section 5.3.1).

5.4.1.3 Bounds of Natural Variability

Similarly to the forced simulation, the time-dependent behavior of the detection variable d_c is estimated for the control simulation, projecting the selected variable of the climate vector $\mathbf{\Psi_c}$ onto $\tilde{\mathbf{N}}$:

$$d_c(t) = \tilde{\mathbf{N}}^{\mathrm{T}}(x,z)\mathbf{\Psi_c}(t,x,z). \tag{5.4}$$

We use $d_c(t)$ to derive the upper and lower bounds of the natural variability, which are subsequently used to determine the detection time for $d_f(t)$. Again, the fixed spatial pattern of natural variability is normalized before computing the detection variable, and temporal - but not spatial - anomalies are used. To avoid a bias in the statistics of the detection variable d_c, we use independent data to estimate the fixed spatial pattern of natural variability $\tilde{\mathbf{N}}$ and the climate vector $\mathbf{\Psi_c}$. The control simulation is divided into two simulations of 230 years length, each, using the first half to estimate $\tilde{\mathbf{N}}$, and the second half to estimate $\mathbf{\Psi_c}$.

To derive the upper and lower bounds of the natural variability, a bootstrap analysis is conducted for the detection variable $d_c(t)$. Generally, $d_c(t)$ can be treated similarly to the univariate timeseries analyzed in Baehr et al. (2006). However, some differences arise in adding observational uncertainty to the simulated measurements. Aiming to present a self-consistent description of the method here, we provide the full detection algorithm. To the components forming the control detection variable, random observation error ε_ρ is added for n_b realizations before the intrinsic bootstrap analysis is performed:

$$d_c(t,n_b) = \tilde{\mathbf{N}}^{\mathrm{T}}(x,z)\left[\mathbf{\Psi_c}(t,x,z) + \varepsilon_\rho(t,n_b,x,z)\right], \tag{5.5}$$

and the bootstrap analysis is conducted for a range of length of observation periods l, each starting at a different random starting point t^*, yielding a detection variable $d_c^*(l, n_b)$, depending on l and n_b:

$$d_c^*(l, n_b) = d_c(t^* : t^* + l, n_b). \tag{5.6}$$

This detection variable can subsequently be treated like a univariate timeseries: linear trends $p^*(l, n_b)$ are estimated by a least squares fit for each of these bootstrap samples. For each length of observation period, the upper and lower bound confidence limits are estimated ($\alpha = 0.05$). The natural variability is described by an interval of linear trends $[c_{lower}(l), c_{upper}(l)]$.

5.4.1.4 Changes in the Forced Run

Similarly to the control simulation, we estimate trends in the forced simulation, which can be used to test whether the forced run has left the range of natural variability given by the control simulation. To include observational uncertainty into the detection variable $d_f(t)$, we again add random observation error to equation (5.1):

$$d_f(t, n_b) = \tilde{\mathbf{N}}^{\mathrm{T}}(x, z) \left[\mathbf{\Psi_f}(t, x, z) + \varepsilon_\rho(t, n_b, x, z) \right], \tag{5.7}$$

and conduct a bootstrap analysis for a range of length of observation periods, which all start at the same fixed starting point t_{start}:

$$d^*(l, n_b) = d\left[t = t_{start} : (t = t_{start}) + l \right]. \tag{5.8}$$

Linear trends $p_f^*(l, n_b)$ are estimated by least squares fit for each length of observation period, and for all bootstrap samples.

5.4.1.5 Detection Time

To estimate the detection time, we first derive the times, t_{det}, where the forced run has left the given range of natural variability with $1 - \frac{\alpha}{2}$ reliability:

$$t_{det}(t) = \begin{cases} t_{start} + l & \text{, if } \dfrac{\sum_{i=1}^{n_b} I\left[(p_f^*(l,i) < c_{lower}(l)\right]}{n_b} \geq 1 - \frac{\alpha}{2} \\ t_{start} + l & \text{, if } \dfrac{\sum_{i=1}^{n_b} I\left[(p_f^*(l,i) > c_{upper}(l)\right]}{n_b} \geq 1 - \frac{\alpha}{2} \\ 0 & \text{, otherwise} \end{cases} , \tag{5.9}$$

where I is the indicator function with argument a, which is equal to 1 if its argument is true, and zero otherwise:

$$I(a) = \begin{cases} 1 & \text{, if } \quad a = \text{true} \\ 0 & \text{, if } \quad a = \text{false} \end{cases} . \tag{5.10}$$

We denote as detection time, t_D, the minimum (> 0) of t_{det}:

$$t_D = min\left\{t_{det}\right\}, \tag{5.11}$$

i.e., the first time at which the forced run has left the range of natural variability, given by the control run, with 95 percent reliability.

5.4.2 Results of the Detection Analysis

We simulate the continuous observations of density with the RAPID-MOC array at 26°N, as described in section 5.2.3. Initially, we consider an observing system without observation error. The detection variables for the forced simulation ($d_f(t)$), and the control simulation ($d_c(t)$) are calculated following equations 5.1 and 5.4, respectively (figure 5.4). We average $\tilde{\mathbf{N}}$ and the climate vector $\mathbf{\Psi_f}$ or $\mathbf{\Psi_c}$, respectively, over the eastern and western boundaries (as used in figures 5.2 and 5.4), and subtract the resulting profiles from each other, before computing the detection variables.

Depending on the depth over which the detection variable for the forced simulation is computed, the signal-to-noise ratio varies significantly. If the full water column

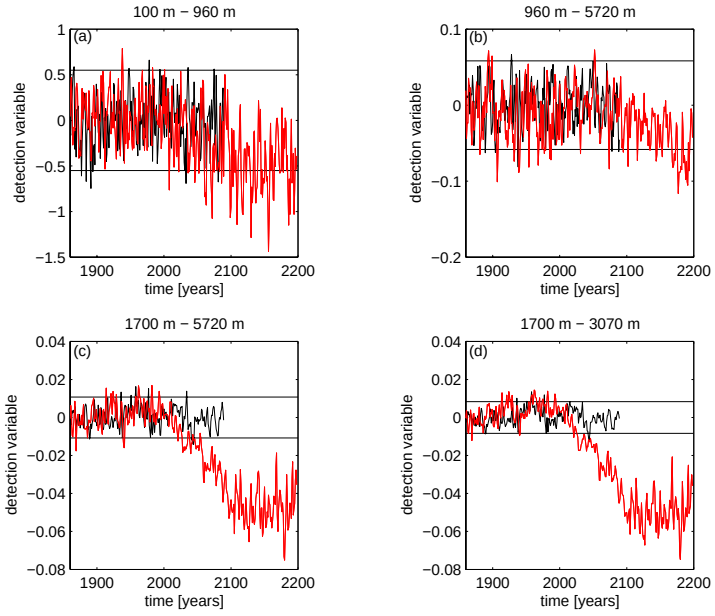

Fig. 5.4: Detection variables for the forced simulation (red) and control simulation (black) over different depths: (a) 100 m to 960 m, (b) 1000 m to bottom (5720 m), (c) 1700 m to bottom, (d) 1700 m to 3100 m. The indicated upper and lower limits of the control detection variable (horizontal black lines) correspond to $\pm$ 1.96 standard deviations of d_c. The detection variable is based on zonal density differences, eastern boundary minus western boundary. The boundaries extend from 70°W to 80°W (western boundary) and 26°W to 36°W (eastern boundary).

(over the full transect) is considered, no trend is visible [not shown]. A weak trend is apparent if the strongly varying top 100 m of the water column are left out (figure 5.4a). Note that constraining the analysis to the top 1000 m of the water column or considering the full depth (below 100 m) does not significantly change the shape of the detection variable. Between 500 m and 1000 m, waters warm and freshen significantly, with compensating effects on the density difference (*cf.*, figure 5.3d). Considering the water column between 1000 m and the bottom does not enhance the signal (figure 5.4b), whereas the zonal density difference shows a strong decrease at depths between 1700 m and the bottom (figure 5.4c). Most of this signal is found between 1700 m and 3100 m (figure 5.4d). While the zonal difference in salinity decreases with time throughout the water column, temperature differences are mainly constrained to the top 2000 m. The detection variable computed in figure 5.4d is therefore dominated by haline changes in the zonal density difference. However, neither the detection variable derived from zonal salinity difference nor temperature difference alone provides a reliable estimate of the zonal density difference. These detection variables allow for a visual estimate of the respective detection time, but they do not allow to derive a formal statistical statement about the respective detection time.

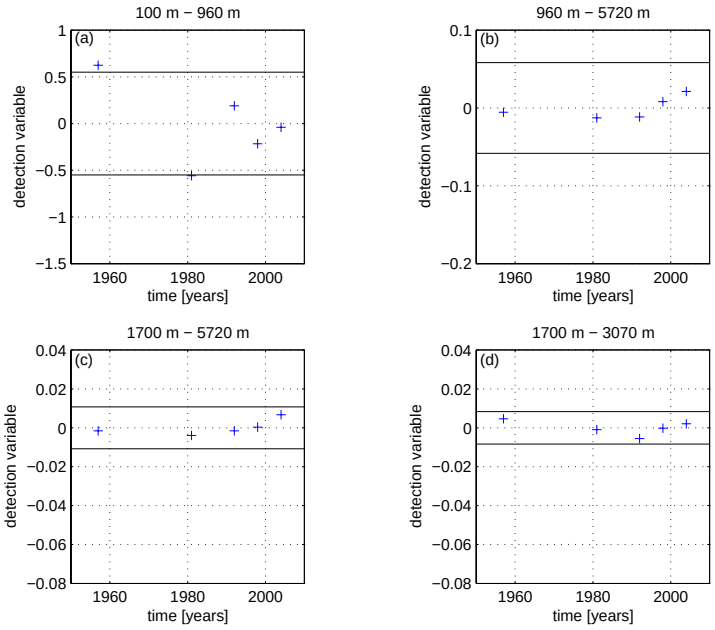

Fig. 5.5: Detection variables for hydrographic occupations of 26°N over different depth ranges: (a) 100 m to 960 m, (b) 1000 m to bottom (5720 m), (c) 1700 m to bottom, (d) 1700 m to 3100 m. The indicated upper and lower limits of the control detection variable (horizontal black lines) correspond to ± 1.96 standard deviations of d_c; identical to the confidence limits shown in figure 5.4. The detection variable is based on zonal density differences, eastern boundary minus western boundary. The boundaries extend from 65°W to 75°W (western boundary), 25°W to 35°W (eastern boundary).

For comparison with the modelling results, the corresponding detection variable based on the five hydrographic occupations of the 26°N transect are calculated (figure 5.5). The observed detection variable is the result of projecting the observed zonal density difference onto the fixed spatial pattern of natural variability provided by the control simulation of the model ($\tilde{\mathbf{N}}$), equation (5.3). Note that again, we compute the detection variable based on anomalies by subtracting the time-mean over all observations from the individual observations. Comparing the same depth ranges as used in figure 5.4, we find that none of the analyzed depth ranges shows a significant trend between 1957 and 2004 (figure 5.5), implying no MOC trend over the past 50 years.

To conduct a formal detection analysis, the detection algorithm described in section 5.4.1.5 is applied. We add observation error to the detection variable derived from the simulated observations. For both $d_c^*(l, n_b)$ and $d^*(l, n_b)$, we use $n_b = 10^3$ realizations of the respective observation uncertainty (identically, independently and

Tab. 5.1: Detection time (95 percent upper confidence limit; in years) for different observation errors and zonal density differences over different depths. The three numbers represent the three realizations of the forced run.

Depth range	Observation error		
	$\varepsilon_\rho = 0.005$ kg m^{-3}	$\varepsilon_\rho = 0.01$ kg m^{-3}	$\varepsilon_\rho = 0.015$ kg m^{-3}
100 m - 960 m	59, 36, 11	60, 36, 11	60, 37, 11
100 m - 5720 m	60, 45, 11	59, 48, 11	60, 51, 11
960 m - 5720 m	75, 46, 57	92, 52, 61	93, 58, 61
1700 m - 5720 m	30, 36, 31	47, 36, 37	59, 36, 42
1700 m - 3070 m	25, 10, 30	29, 11, 30	39, 12, 35

normally distributed random noise) of different magnitudes. We use identical magnitudes for $\varepsilon_\rho(n_b)$ in the control and forced simulations, *e.g.*, 0.005 kg m^{-3} (standard deviation). The detection times, computed following equation (5.11), differ considerably between the different depth ranges (table 5.1). Considering the full water column with only leaving out the top 100 m results in a detection time (95 percent reliability) of around 60 years. This detection time is reduced by about 50 percent if the analysis concentrates on the range between 1700 m and 3100 m. Different magnitudes of observation error have little influence on the detection times (table 5.1).

5.5 Discussion

To derive a detection variable for anthropogenic MOC changes, we use - in deviation of Hasselmann (1979, 1993) and Hegerl et al. (1996) - a fixed spatial pattern of natural variability onto which we project the (simulated) observations. Therefore, we do not make any assumption about the anticipated long-term change in the underlying pattern. The employed fixed spatial pattern of natural variability is sought to be available from real observations (though not yet at present), whereas the selection of a suitable guess pattern (as in *e.g.*, Hegerl et al. (1996)) is inherently dependent on the quality of the chosen model. Note that our fixed spatial pattern of natural variability $\tilde{\mathbf{N}}$ (as described by equation 5.3) does not represent the full climate noise; the truncation level is not derived from a formal statistical algorithm, but follows physical arguments. In further deviation from Hegerl et al. (1996), we do not use linear trends to represent the time dependence of the climate signal in the detection variable. We do, however, approximate the climate signal with linear trends over varying lengths of time intervals, when computing the detection time, following Santer et al. (1995) and Baehr et al. (2006).

The employed fixed spatial pattern of natural variability is model-based, but it has been confirmed against observations (section 5.3.1). This time-independent, fixed spatial description of the natural variability, derived from the model's control simulation, can therefore be used to test independently whether the forced model simulation or the observations have left this given range of natural variability, *i.e.*, whether an MOC change is detected in the respective (simulated) observations or not. Analyzing the forced model simulation suggests that the detection variable is sensitive to anthropogenic forcing (figure 5.4), and anthropogenic changes in the MOC can be detected within a couple of decades (table 5.1). Repeating the analysis for the existing observations (Bryden et al., 2005) suggests that the observed variations in the density field and its associated meridional transports are within the model's natural variability (figure 5.5).

The classical approach for a multivariate analysis was established by Hasselmann (1979, 1993) and Hegerl et al. (1996). With such an optimal fingerprint method anthropogenic changes in the temperature field at the depth-longitude transect at 26°N would be detected within the first two decades after 2000 [not shown]. This detection time does, however, not distinguish between temperature changes related to an MOC change, and temperature changes unrelated to an MOC change. Using the meridional transport field yields detection times of about 70 years, *i.e.* no improvement over the univariate analysis of an MOC timeseries. For the relatively small extent of a single zonal transect (that is not an ocean basin average) the optimal fingerprint technique is of limited use: the number of empirical orthogonal functions (EOFs) needed to yield a stable estimate of the noise covariance matrix - whose inverse is used to rotate the guess pattern, yielding the optimal fingerprint - is too large to allow for a sufficiently large space for optimizing the fingerprint. An optimal fingerprint based on such a limited rotation does not provide an improved detection time compared to that delivered by the original guess pattern.

Instead of considering a different quantity than the MOC, we have initially investigated including additional information at several depths, *i.e.* the vertically unintegrated meridional transports. Both an optimal fingerprint following *e.g.*, Hegerl et al. (1996), and the method introduced in section 5.4.1, detect changes in the MOC after about 70 years (in the given climate change scenario; not shown), whereas the univariate analysis results in detection times of about 60 years Baehr et al. (2006). Detection times improve when the vertical integral of the meridional transports, *i.e.*, the MOC is derived. Correlations between the zonally integrated transports at different depths are very low. Vertical integration results in higher correlation coefficients between adjacent depths and imply a higher signal-to-noise ratio; this

in turn, yields smaller detection times for a single MOC timeseries than a suite of meridional transport timeseries.

We show that the detection times depend largely on the chosen depth range, rather than the chosen observation error added to the zonal density gradient (table 5.1). We have, however, not included any observational uncertainty in the estimate of the fixed spatial pattern of natural variability. While it would be desirable to include uncertainty in the MOC estimate, it would result in multiplying two random numbers (equation 5.7), which in turn would result in a detection variable that is not normally distributed. Including observational uncertainty to the MOC estimate alone, and not to the simulated density measurements, results in somewhat increased detection times [not shown].

Although we use three simulations of a climate change scenario, and find the results to be robust across these realizations, the conclusions are still dependent on the particular model employed; especially with respect to the reliable separation of the global warming signal and MOC changes. However, the estimate of the fixed spatial pattern of natural variability is based on physical reasoning (*cf.*, section 5.3.2), and in addition, we find the pattern to be consistent with observations (*cf.*, section 5.3.1).

A further question is whether additional observations allow for a faster detection. In part, Vellinga and Wood (2004) addressed this question using optimal fingerprints. In a next step, Vellinga and Wood's (2004) findings could be combined with the results of the present study, *i.e.*, testing whether the addition of another latitude improve detection times. However, to apply the resulting conclusions to the real ocean, further knowledge about the dynamics of potential MOC changes is needed in addition to the formal detection analysis. This investigation of the propagation of the MOC signal, and the coherence of the MOC cell are beyond the scope of this paper, and the assessment of additional observations to improve the detection time is therefore left for future study.

5.6 Conclusions

Based on our analysis of the five hydrographic occupations of the 26°N transect, and our simulated MOC and density observations in the particular solutions of ECHAM5/MPI-OM, we conclude:

1. The changes in existing density observations and related meridional transports at 26°N (Bryden et al., 2005) are within the model's range of natural variability.

2. Using a realizable set of observations, a reliable detection variable for anthropogenic MOC change can be derived by projecting (simulated) observations onto a suitably chosen observed representation of the natural variability, displaying a fixed spatial pattern.

3. Zonal density gradients at 26°N yield a reliable detection variable for MOC changes at 26°N. Observations limited to the eastern or the western boundary, or either the salinity or the temperature field alone, are not capable of delivering this information.

4. For zonal density gradients between 1700 m and 3100 m at 26°N, with an assumed observation error of 0.01 kg m^{-3}, the detection time (95 percent reliability) is about 30 years; a reduction by about 50 percent, compared to using a univariate MOC timeseries.

Acknowledgements We thank Reiner Schnur for stimulating discussions. This work was supported by the Max Planck Society (JB, HH, JJ, JM). The computer simulations were performed at the DKRZ (Deutsches Klimarechenzentrum) in Hamburg, Germany. The 2004 transatlantic hydrographic section along 25°N was supported by the Natural Environment Research Council as part of the Core Strategic Research Programme 'Ocean Variability and Climate' at Southampton Oceanography Centre. Analysis of the five sections along 25°N was also supported by NERC as part of the RAPID Programme.

6. CONCLUSIONS AND OUTLOOK

6.1 Conclusions

I conclude this thesis by means of the questions posed in the introduction (chapter 1.3), based on the results of 'deploying' an MOC monitoring array in different numerical models.

6.1.1 Does a similar MOC monitoring array work at other - dynamically and geographically less special - latitudes in the North Atlantic?

Monitoring arrays with profiles at about 10 locations, similar to the feasible setup for 26°N (9 profiles), were tested at two different latitudes, namely at 36°N, and 53°N. 36°N represents a subtropical latitude with a western boundary current that is not confined to a shallow strait. If this western boundary current is to be reconstructed from density profiles alone, a qualitatively similar reconstruction to that achieved at 26°N requires 12 profiles in total (chapter 2.3.2). 53°N is at the boundary to the subpolar gyre and exhibits much weaker stratification than the two subtropical latitudes. At this transect, the tested array is not able to capture the main characteristics of the MOC (chapter 2.3.2). However, with the additional use of bottom velocities, a reconstruction that is qualitatively similar to that found at 26°N and 36°N can be achieved (chapter 2.3.4).

Hence, MOC monitoring based on the monitoring strategy proposed by Marotzke et al. (2002) and Hirschi et al. (2003) is applicable - in the model employed - at latitudes where bottom velocities are small. At these latitudes, an array based on density and surface wind stress measurements can reproduce the MOC in its temporal and vertical structures. In contrast, at latitudes of high bottom velocity only an array including additional observations of the complete bottom velocity field is able to capture the main characteristics of the MOC.

6.1.2 Can the intuition-based array design be improved by an optimized array design?

Two optimization techniques (sequential and global optimization) were tested at 26°N and 53°N. I found that sequential optimization does not improve on heuristic array design, since the incremental addition of profiles is not able to capture the characteristics of this convex problem (chapter 3.3.2). The global optimization, however, outperforms the heuristic array design if one chooses to optimize the MOC timeseries at 1000 m at both latitudes (chapter 3.3.3). But at 53°N, *i.e.*, at a latitude where the proposed monitoring strategy does not have the ability to reproduce the MOC at 1000 m, the improved quality of the global optimization over heuristic array design relies mainly on an accidental compensation of transport overestimates and transport underestimates, and the suggested setup is not physically meaningful (chapter 3.3.5).

Hence, global optimization has the potential to facilitate pre-deployment array design. However, the physical meaningfulness of the results has to be established subsequently, as the global optimization might merely represent an accidental compensation of misfits.

6.1.3 Is the proposed 26°N MOC monitoring array able to reliably capture long-term changes in the MOC?

In the model employed, the proposed 26°N MOC monitoring array is able to capture the short-term variability, the long-term (up to multidecadal) variability, and changes in the mean value induced by anthropogenic forcing (chapter 4.2.3).

6.1.4 Can changes in the MOC be detected faster with array measurements at 26°N or with repeated hydrographic transects?

To investigate this question, I analyze three realizations of the emissions scenario A1B[1] in a coupled model, in which the MOC gradually weakens by 30 percent between 2001 and 2100, but does not collapse. Applying a statistically rigorous detection algorithm to a univariate MOC timeseries yields that observation periods of less than 20 years carry a high probability to result in 'false alarms'. If MOC changes

[1] In this scenario, the CO_2 concentrations rise from 380 ppmv (year 2001) to 700 ppmv (year 2100). The simulations are extended until the year 2199 with greenhouse gas concentrations fixed at the levels of the year 2100.

at 26°N should be detected on the basis of a univariate MOC timeseries with a reliability of 95 percent, decades to a century of continuous observations are required, depending on the observation error (chapter 4.3.2.2). For an observation error of 3 Sv (standard deviation), and a detection with 95 percent reliability, continuous observations result in a detection time of about 100 years, while hydrographic sections every 20 years result in a detection time of about 120 years (chapter 4.3.2.2). Note that the detection time for continuous observations with an observation error of 1 Sv is reduced to approximately 60 years (with 95 percent reliability) (chapter 4.3.2.2).

A multivariate detection analysis yields considerably shorter detection times of the MOC weakening in the same A1B scenario simulation. However, this result applies not to a composite of transport timeseries, but rather using zonal density gradients at 26°N: the detection time (95 percent reliability) that results from examining zonal density gradients between 1700 m and 3100 m at 26°N, with an assumed observation error of 0.01 kg m^{-3}, lies at about 30 years (chapter 5.4.2).

Hence, in this particular model and emission scenario, MOC changes at 26°N are detected (*i*) after more than a century using repeated hydrographic transects, (*ii*) after 60 to 100 years for a univariate timeseries derived from an MOC monitoring array, and (*iii*) after about 30 years for a multivariate analysis of zonal density gradients derived from an MOC monitoring array.

6.1.5 Based on the already existing measurements of density and related meridional transports at 26°N, is it possible to distinguish between natural variability and a real trend in the MOC strength?

To test this, I project the observations onto a time-independent, fixed spatial pattern of natural variability of the zonal density gradients (chapter 5.4.1). This natural variability is derived from the model's control simulation, but has been confirmed against observations: the observed difference in temperature and salinity found between the 1957 and the 2004 occupation of the 26°N section are similar to the anomaly patterns found in the model when temperature and salinity are regressed against the strength of the MOC (chapter 5.3.1). For each observation year, a detection variable is computed and compared to a confidence interval that is computed by projecting simulated observations within an independent control simulation onto the derived pattern of natural variability. Over none of the analyzed depth ranges is a significant trend found in the detection variable between 1957 and 2004 (chapter

5.4.2), implying that there has been no detectable MOC trend over the last 50 years.

Hence, the changes in existing density observations and related meridional transports at 26°N (Bryden et al., 2005) are within the employed model's range of natural variability.

6.1.6 Concluding Remarks Regarding MOC Monitoring at 26°N

The results presented here suggest that continuous MOC monitoring at 26°N could play an essential role in assessing the strength of the MOC and its variability. Here, I briefly summarize the findings of this thesis with respect to the latitude's 26°N particular adequacy for MOC monitoring.

The continuous monitoring of the confined western boundary current ensures coverage of the depth-dependent velocities, which in turn allows one to recover the full MOC from additional density and zonal wind stress measurements. The underlying assumption that the thermal wind and Ekman contribution are the dominant terms in the force balance governing the MOC is not readily justified at other latitudes (chapter 2.3.4); this result has been confirmed by the findings of Köhl (2005) and Hirschi and Marotzke (2006).

For any given reliability in the detection of MOC changes at 26°N, a continuous observing system is less expensive than repeated hydrographic sections (chapter 4.4).

Zonal density gradients at 26°N yield a reliable detection variable for MOC changes at 26°N; observations limited to the eastern or the western boundary, or either the salinity or the temperature field alone, are not capable of delivering this information (chapters 5.3.2, 5.4.2).

The uninterrupted continuation of the deployed RAPID-MOC 26°N array is a necessary step towards the continuous observation of the MOC. An immediate advancement of it will be an improved understanding of the variability of the different transport components at short timescales. This will allow for a partial re-design of the array, with the ultimate goal of the operational deployment of a continuous observing system. Such an observing system would then permit improved studies of the attribution and prediction of future MOC changes.

6.2 Outlook

MOC observations at 26°N are only a first step towards a comprehensive observing system of the North Atlantic MOC. However, the results presented here suggest that the RAPID-MOC 26°N array should be an integral part of such a system, and it is therefore necessary to continue the RAPID-MOC measurements at 26°N.

A comprehensive observing array for the North Atlantic MOC needs to be designed aiming at continuous observation and ultimately predicting the MOC. The identification of the optimal locations for the required measurements to monitor the MOC is an important research task, and - in advance - investigations into the nature of the propagation of the MOC signal and the coherence of the MOC cell are necessary. Further, the locations and oceanic fields that allow to forecast MOC changes months or years ahead, need to be identified.

In a first step, an integrated picture of the existing observing campaigns that have been in place to monitor transports in the North Atlantic would be useful. These observational campaigns spread over a variety of locations (and timescales): for example, the 16° MOVE western boundary current array, direct flow measurements at the exit of the Labrador Sea, overflow measurements at the Faroe-Shetland channel and in the Denmark Strait, the OVIDE project, and the other RAPID UK projects.

Subsequently, these data need to be combined in a model-data synthesis based on data assimilation, using *e.g.*, the ECCO model (*e.g.*, Stammer et al., 2002, 2003). Such synthesis allows one to describe the spatial and temporal signal of MOC variability (*e.g.*, Wunsch and Heimbach, 2006), and investigate its underlying dynamics.

Future array design concerning the detection of MOC changes might include a multivariate analysis with respect to extending the climate vector with respect to its spatial dimension an the employed variables. Additionally, optimal observations (*e.g.*, Köhl and Stammer, 2004; Köhl, 2005) provide a powerful tool to identify suitable places and variables for monitoring and predicting the MOC.

Ultimately, the results of such model-based studies should be connected to actual field work. The design of future observational campaigns could rely on a combination of both observational insights and the knowledge gained from model-based array design studies; eventually aiming to jointly realize and operate the most adequate observing network for monitoring and predicting MOC changes.

BIBLIOGRAPHY

Adams, R., Brown, M., Colgan, C., Flemming, N., Kite-Powell, H., McCarl, B., Mjelde, J., Solow, A., Teisberg, T., and Weiher, R. (2000). The economics of sustained ocean observations: Benefits and rationale for public funding. Technical report, A joint publication of the National Oceanic and Atmospheric Administration and the Office of Naval Research.

Ali, M. M., Khompatraporn, C., and Zabinsky, Z. (2005). A numerical evaluation of several stochastic algorithms on selected continuous global optimization test problems. *Journal of Global Optimization*, 31(4):635–672.

Alley, R. B., Marotzke, J., Nordhaus, W. D., Overpeck, J. T., Peteet, D. M., Pielke Jr., R. A., Pierrehumbert, R. T., Rhines, P. B., Stocker, T. F., Talley, L. D., and Wallace, J. M. (2003). Abrupt climate change. *Science*, 299:2005–2010.

Arbic, B. K. and Owens, W. B. (2001). Climate warming of Atlantic Intermediate Waters. *Journal of Climate*, 14:4091–4108.

Athias, V., Mazzega, P., and Jeandel, C. (2000). Selecting a global optimization method to estimate the oceanic particle cycling rate constants. *Journal of Marine Research*, 58(5):675–707.

Baehr, J., Hirschi, J., Beismann, J., and Marotzke, J. (2004). Monitoring the meridional overturning circulation in the North Atlantic: A model-based array design study. *Journal of Marine Research*, 62 (3):283–312.

Baehr, J., Keller, K., and Marotzke, J. (2006). Detecting potential changes in the meridional overturning circulation at 26°N in the Atlantic. *Climatic Change*. In press.

Banks, H. and Wood, R. A. (2002). Where to look for anthropogenic climate change in the ocean? *Journal of Climate*, 15:879–891.

Banks, H. T. and Bindoff, N. L. (2003). Comparison of observed temperature and salinity changes in the Indo-Pacific from the coupled cliamte model HadCM3: processes and mechanisms. *Journal of Climate*, 16:156–166.

Baringer, M. O. and Larsen, J. C. (2001). Sixteen years of Florida Current transport at 27°N. *Geophysical Research Letters*, 28:3179–3182.

Barnett, T. P. (1991). *Greenhouse-Gas-Induced-Climatic Change: A Critical Appraisal of Simulations and Observations*, chapter An attempt to detect the greenhouse-gas signal in a transient GCM simulation, pages 559–568. Elsevier Science.

Barnett, T. P., Pierce, D. W., and Schnur, R. (2001). Detection of anthropogenic climate change in the world's oceans. *Science*, 292:270–274.

Barnier, B., Siefriedt, L., and Marchesiello, P. (1995). Thermal forcing for a global ocean circulation model using a three-year climatology of ECMWF analyses. *Journal of Marine Systems*, 6(4):363–380.

Barth, N. and Wunsch, C. (1990). Oceanographic experiment design by simulated annealing. *Journal of Physical Oceanography*, 20:1249–1263.

Barth, N. H. (1992). Oceanographic experiment design II: Genetic algorithms. *Journal of Atmospheric and Oceanic Technology*, 9:434–443.

Beckmann, A. and Döscher, R. (1997). A method for improved representation of dense water spreading over topography in geopotential-coordinate models. *Journal of Physical Oceanography*, 27:581–591.

Beismann, J. and Redler, R. (2003). Model simulations of CFC uptake in North Atlantic deep water: Effects of parametrizations and grid resolution. *Journal of Geophysical Research*, 108(C5):3159, doi: 10.1029/2001JC001253.

Bennett, A. F. (1985). Array design by inverse methods. *Progress in Oceanography*, 15:129–156.

Bennett, A. F. and McIntosh, P. C. (1982). Open ocean modelling as an inverse problem: Tidal theory. *Journal of Physical Oceanography*, 12:1004–1018.

Böning, C. W. and Bryan, F. O. (1996). *The Warmwatersphere of the North Atlantic Ocean*, chapter Large-Scale Transport Processes in High-Resolution Circulation Models, pages 91–128. Gebrüder Bornträger, Berlin.

Böning, C. W., Dieterich, C., Barnier, B., and Jia, Y. (2001). Seasonal cycle of meridional heat transport in the subtropical North Atlantic: A model intercomparison in relation to observations near 25°N. *Progress in Oceanography*, 48:231–253.

Boyer, T. P. and Levitus, S. (1997). *Objective analyses of temperature and salinity for the world ocean on a 1/4 degree grid, NOAA Atlas NESDIS 11.* NOAA Atlas NESDIS, U.S. Dep. of Comm., Washington D. C.

Brennan, C. E., Matear, R. J., and Keller, K. (2006). Oxygen concentrations improve the detection capabilities of an ocean circulation observation array. In preparation.

Bretherton, F. P., Davis, R. E., and Fandry, C. B. (1976). A technique for objective analysis and design of oceanographic experiments applied to MODE-73. *Deep-Sea Research*, 23:559–582.

Bryden, H. L., Griffiths, M. J., Lavin, A. M., Millard, R. C., Parrilla, G., and Smethie, W. M. (1996). Decadal changes in water mass characteristics at 24°N in the Subtropical North Atlantic. *Journal of Climate*, 9:3162–3186.

Bryden, H. L. and Imawaki, S. (2001). *Ocean circulation and climate: Observing and modelling the global ocean*, chapter Ocean heat transport, pages 455–474. Academic Press, San Francisco.

Bryden, H. L., Johns, W. E., and Saunders, P. M. (2006). Deep Western Boundary Current east of Abaco: Mean structure and transport. *Journal of Marine Research*. Submitted.

Bryden, H. L., Longworth, H. R., and Cunningham, S. A. (2005). Slowing of the Atlantic meridional overturning circulation at 25°N. *Nature*, 438:655–657.

Bryden, H. L., McDonagh, E. L., and King, B. A. (2003). Changes in ocean water mass properties: Oscillations or trends? *Science*, 300:2086–2088.

Chereskin, T. K., Wilson, W. D., Bryden, H. L., Field, A., and Morrison, J. (1997). Observations of the Ekman balance at 8°30′N in the Arabian Sea during the 1995 southwest monsoon. *Geophysical Research Letters*, 21:2541–2544.

Cox, M. D. (1987). Isopycnal diffusion in a z-coordinate model. *Ocean Modeling*, 74:1–5.

Cunningham, S. A. (2005). RRS Discovery Cruise D279 04 APR - 10 MAY 2004: A transatlantic hydrography section at 24.5°N. Technical report, Southampton Oceanography Centre, Southampton.

Cunningham, S. A. and Alderson, S. (2006). Transatlantic temperature and salinity changes at 24.5°N from 1957 to 2004. In preparation.

Dansgaard, W., Johnsen, S. J., Clausen, H. B., Dahl-Jensen, D., Gundestrup, N. S., Hammer, C. U., Hvidberg, C. S., Steffensen, J. P., Sveinbjoernsdottir, A. E., Jouzel, J., and Bond, G. (1993). Evidence for general instability of past climate from a 250-kyr ice-core record. *Nature*, 364:218–220.

Dengg, J., Böning, C., Ernst, U., Redler, R., and Beckmann, A. (1999). Effects of an improved model representation of overflow water on the Subploar North Atlantic. *International WOCE Newsletter*, 37:10–15.

Dobrolyubov, S. A., Lappo, S. S., Morozov, E. G., Sokov, A. V., Tereschenkov, V. P., and Shapovalov, S. M. (2002). Water structure in the North Atlantic in 2001 based on a transatlantic section along 53°N. *Oceanology*, 382(4):543–546.

Eden, C. and Willebrand, J. (2001). Mechanism of interannual to decadal variability of the North Atlantic circulation. *Journal of Climate*, 14:2266–2280.

Fillenbaum, E. R., Lee, T. N., Johns, W. E., and Zantopp, R. J. (1997). Meridional heat transport variability at 26.5°N in the North Atlantic. *Journal of Physical Oceanography*, 27:153–174.

Fischer, J., Schott, F. A., and Dengler, M. (2003). Boundary ciruclation at the exit of the Labrador Sea. Submitted to Journal of Physical Oceanography.

Fuglister, F. C. (1960). *Atlantic Ocean atlas of temperature and salinity profiles and data from the International Geophysical Year of 1957-1958.* Woods Hole Oceanographic Institution, Woods Hole.

Ganachaud, A. (2003). Error budget of inverse box models: The North Atlantic. *Journal of Atmospheric and Oceanic Technology*, 20:1641–1655.

Ganachaud, A. and Wunsch, C. (2000). Improved estimates of global ocean circulation, heat transport and mixing from hydrographic data. *Nature*, 408:453–457.

Ganachaud, A. and Wunsch, C. (2002). Oceanic nutrient and oxygen transports and bounds on export production during the World Ocean Circulation Experiment. *Global Biogeochemical Cycles*, 16(4):1057–1071.

Gloor, M., Fan, S. M., Pacala, S., and Sarmiento, J. (2000). Optimal sampling of the atmosphere for purpose of inverse modeling: A model study. *Global Biogeochemical Cycles*, pages 407–428.

Goldberg, D. E. (1989). *Genetic algorithms in search, optimization, and machine learning.* Addison-Wesley Publishing Company, Reading, MA.

Gregory, J. M., Dixon, K. W., Stouffer, R. J., Weaver, A. J., Diesschaert, E., Eby, M., Fichefet, T., Hasumi, H., Hu, A., Jungclaus, J. H., Kamenkovich, I. V., Levermann, A., Montoya, M., Murakami, S., Nawrath, S., Oka, A., Sokolov, A. P., and Thorpe, R. B. (2005). A model intercomparison of changes in the atlantic thermohaline circulation in response to increasing atmospheric CO_2 concentration. *Geophysical Research Letters*, 32:L12703, doi: 10.1029/2005GL023209.

Guinehut, S., Larnicol, G., and P. Y. Le Traon (2002). Design of an array of profiling floats in the North Atlantic from model simulations. *Journal of Marine Systems*, 35:1–9.

Hackert, E. C., Miller, R. N., and Busalacchi, A. J. (1998). An optimized design for a moored array in the tropical Atlantic Ocean. *Journal of Geophysical Research*, 103(C4):7491–7509.

Hall, M. M. and Bryden, H. L. (1982). Direct estimates and mechanisms of ocean heat transport. *Deep Sea Research*, 29, No. 3A:339–359.

Harrison, D. E. (1989). Local and remote forcing of ENSO ocean waveguide response. *Journal of Physical Oceanography*, 19:691–695.

Harrison, D. E., Kessler, W. S., and Giese, B. J. (1989). Ocean circulation and model hindcasts of the 1982-83 El Nino: Thermal variability along the ship-of-opportunity tracks. *Journal of Physical Oceanography*, 19:397–418.

Hasselmann, K. (1979). *Meteorology of the Tropical Oceans*, chapter On the signal-to-noise problem in atmospheric response studies, pages 251–259. Royal Meteorological Society.

Hasselmann, K. (1993). Optimal fingerprints for the detection of time-dependent climate change. *Journal of Climate*, 6:1957–1971.

Hasselmann, K. (1998). Conventional and Bayesian approach to climate-change detection and attribution. *Quarterly Journal of the Royal Meteorological Society*, 124(552):2541–2565.

Hegerl, G., von Stroch, H., Hasselmann, K., Santer, B. D., Cubasch, U., and Jones, P. D. (1996). Detecting greenhouse-gas-induced climate change with an optimal fingerprint. *Journal of Climate*, 9:2281–2306.

Heinrich, H. (1988). Origin and consequences of cyclic ice rafting in the northeast Atlantic Ocean during the past 130,000 years. *Quaternary Research*, 29 (2):142–152.

Hernandez, F., Letraon, P., and Barth, N. (1995.). Optimizing a drifter cast strategy with a genetic algorithm. *Journal of Atmospheric and Oceanic Technology*, 12(2):330–345.

Hirschi, J., Baehr, J., Marotzke, J., Stark, J., Cunningham, S., and Beismann, J.-O. (2003). A monitoring design for the Atlantic meridional overturning circulation. *Geophysical Research Letters*, 30(7):1413, doi: 10.1029/2002GL016776.

Hirschi, J. and Marotzke, J. (2006). Reconstructing the meridional overturning circulation from boundary densities and zonal wind stress. *Journal of Physical Oceanography*. In press.

Hu, A., Meehl, G. A., and Han, W. (2004). Detecting thermohaline circulation changes from ocean properties in a coupled model. *Geophysical Research Letters*, 31:L13204, doi: 10.1029/2004GL020218.

Jayne, S. R. and Marotzke, J. (2001). The dynamics of ocean heat transport variability. *Reviews of Geophysics*, 39:385–411.

Jungclaus, J., Haak, H., Esch, M., Roeckner, E., and Marotzke, J. (2006a). Will Greenland melting halt the thermohaline circulation? *Geophysical Research Letters*. In press.

Jungclaus, J. H., Botzet, M., Haak, H., Luo, J., Latif, M., Marotzke, J., Mikolajewicz, U., and Roeckner, E. (2006b). Ocean circulation and tropical variability in the coupled model ECHAM5/MPI-OM. *Journal of Climate*, 19:3952–3972.

Kalnay, E., Kanamitsu, M., Kistler, R., Collins, W., Deaven, D., Gandin, L., Iredell, M., Saha, S., White, G., Woollen, J., Zhu, Y., Chelliah, M., Ebisuzaki, W., Higgins, W., Janowiak, J., Mo, K. C., Ropelewski, C., Wang, J., Leetmaa, A., Reynolds, R., Jenne, R., and Joseph, D. (1996). The NCEP 40-year reanalysis project. *Bulletin of the American Meteorological Society*, 77:437–471.

Keigwin, L. D. and Boyle, E. A. (2000). Detecting Holocene changes in thermohaline circulation. *Proceedings of the National Academy of Sciences of the United States of America*, 97(4):1343–1346.

Keller, K., Bolker, B. M., and Bradford, D. F. (2004). Uncertain climate thresholds and optimal economic growth. *Journal of Environmental Economics and Management*, 48:723–741.

Keller, K., Deutsch, C., Hall, M. G., and Bradford, D. F. (2006a). Early detection of changes in the North Atlantic meridional overturning circulation: Implications for the design of ocean observation systems. *Journal of Climate*. In review.

Keller, K., Yohe, G., and Schlesinger, M. (2006b). Managing the risks of climate thresholds: Uncertainties and information needs. *Climatic Change*. In press.

Kerr, R. A. (2005). The Atlantic conveyor may have slowed, but don't panic yet. *Science*, 310:1403–1405.

Köhl, A. (2005). Anomalies of meridional overturning: Mechanisms in the North Atlantic. *Journal of Physical Oceanography*, 35:1455–1472.

Köhl, A. and Stammer, D. (2004). Optimal observations for variational data assimilation. *Journal of Physical Oceanography*, 34:529–542.

Koltermann, K. P., Tereschenkov, A. V., Dobroliubov, S. A., Lorbacher, K., and Sy, A. (1999). Decadal changes in the thermohaline circulation of the North Atlantic. *Deep-Sea Research II*, 46:109–138.

Larsen, J. C. (1985). Florida current volume transports from voltage measurements. *Science*, 277:302–304.

Larsen, J. C. (1992). Transport and heat flux of the Florida Current at 27°N derived from cross-stream voltages and profiling data: theory and observations. *Philosophical Transactions of the Royal Society, London*, A 338:169–236.

Latif, M., Roeckner, E., Botzet, M., Esch, M., Haak, H., Jungclaus, J., Legutke, S., Marsland, S., Mikolajewicz, U., and Mitchell, J. (2004). Reconstructing, monitoring and predicting multidecadal-scale changes in the North Atlantic thermohaline circulation with sea surface temperature. *Journal of Climate*, 17:1605–1614.

Lavin, A., Bryden, H. L., and Parrilla, G. (1998). Meridional transport and heat flux variations in the subtropical North Atlantic. *The Global Atmosphere and Ocean System*, 6:231–241.

Lee, T. and Marotzke, J. (1997). Inferring meridional mass and heat transports of the Indian Ocean by fitting a general circulation model to climatological data. *Journal of Geophysical Research*, 102 (C5):10,585–10,602.

Lee, T. and Marotzke, J. (1998). Seasonal cycles of meridional overturning and heat transport of the Indian Ocean. *Journal of Physical Oceanography*, 28:923–943.

Lee, T. N., Johns, W., Schott, F., and Zantopp, R. (1990). Western boundary current structure and variability east of Abaco, Bahamas at 26°N. *Journal of Physical Oceanography*, 20:446–466.

Lee, T. N., Johns, W. E., Zantopp, R. J., and Fillenbaum, E. R. (1996). Moored observations of western boundary current variability and thermohaline circulation at 26.5°N in the subtropical North Atlantic. *Journal of Physical Oceanography*, 26:962–983.

Lempert, R. (2002). A new decision sciences for complex systems. *Proceedings of the National Academy of Sciences of the United States of America*, 99:7309–7313.

Levermann, A., Griesel, A., Hoffmann, M., Montoya, M., and Rahmstorf, S. (2005). Dynamic sea level changes following changes in the thermohaline circulation. *Climate Dynamics*, 24:347–354.

Levitus, S., Burgett, R., and Boyer, T. (1994). *World ocean atlas 1994, Vol. 3: Salinity, NOAA Atlas NESDIS 3.* NOAA Atlas NESDIS/ U.S. Dept. of Comm., Washington D. C.

Lohmann, G., Haak, H., and Jungclaus, J. H. (2006). Detecting climate change in the Atlantic meridional overturning circulation. *Journal of Climate.* Submitted.

Longworth, H. R., Bryden, H. L., and Duncan, L. M. (2005). Historical estimates of Atlantic meridional overturning circulation. Second RAPID Annual Science Meeting and Workshops; http://www.soc.soton.ac.uk/rapid/sci/AnnualMeeting2005.php.

Losch, M., Redler, R., and Schröter, J. (2002). Estimating a mean ocean sate from hydrography and sea-surface height with a nonlinear inverse model: Twin experiments with a synthetic dataset. *Journal of Physical Oceanography*, 32:2096–2112.

Macdonald, A. M. (1998). The global ocean circulation: A hydrographic estimate and regional analysis. *Progress in Oceanography*, 41:281–382.

Macdonald, A. M. and Wunsch, C. (1996). An estimate of global ocean circulation and heat fluxes. *Nature*, 382:436–439.

Manabe, S. and Stouffer, R. J. (1994). Multiple-century response of a coupled ocean-atmosphere model to an increase of atmospheric carbon dioxide. *Journal of Climate*, 7:5–23.

Marotzke, J. (1997). Boundary mixing and the dynamics of three-dimensional thermohaline circulations. *Journal of Physical Oceanography*, 27:1713–1728.

Marotzke, J. (2000). Abrupt climate change and thermohaline circulation: Mechanisms and predictability. *Proceedings of the National Academy of Sciences of the United States of America*, 97:1347–1350.

Marotzke, J., Cunningham, S. A., and Bryden, H. L. (2002). Monitoring the Atlantic meridional overturning circulation at 26.5°N. Proposal accepted by the Natural Environment Research Council (UK), Available at: http://www.noc.soton.ac.uk/rapidmoc/.

Marotzke, J., Giering, R., Zhang, K. Q., Stammer, D., Hill, C., and Lee, T. (1999). Construction of the adjoint MIT ocean general circulation model and application to Atlantic heat transport sensitivity. *Journal of Geophysical Research*, 104:29,529–29,547.

Marotzke, J. and Klinger, B. A. (2000). The dynamics of equatorially asymmetric thermohaline circulations. *Journal of Physical Oceanography*, 30:955–970.

Marsh, R., de Cuevas, B. A., Coward, A. C., Bryden, H. L., and Alvarez, M. (2005). Thermohaline circulation at three key section in the North Atlantic over 1985-2002. *Geophysical Research Letters*, 32:doi:10.1029/2004GL022281.

Marsland, S. J., Haak, H., Jungclaus, J. H., Latif, M., and Röske, F. (2003). The Max-Planck-Institute global ocean/sea ice model with orthogonal curvilinear coordinates. *Ocean Modelling*, 5:91–127.

McCreary, J. P. and Lu, P. (1994). Interaction between the Subtropical and Equatorial ocean ciruclations: The Subtropical Cell. *Journal of Physical Oceanography*, 24:466–497.

McInerney, D. and Keller, K. (2006). Economically optimal risk reduction strategies in the face of uncertain climate thresholds. *Climatic Change*. In press, available at: http://www.geosc.psu.edu/∼kkeller/publications.html.

McIntosh, P. C. (1987). Systematic design of observational arrays. *Journal of Physical Oceanography*, 17:885–902.

McManus, J. F., Francois, R., Gheradi, J., Keigwin, L. D., and Brown-Leger, S. (2004). Collapse and rapid resumption of Atlantic meridional circulation linked to deglacial climate changes. *Nature*, 428:834–837.

McTaggert, K. E., Johnson, G. C., Fleurant, C. I., and Baringer, M. O. (1999). CTD/O_2 measurements collected on a Climate and Global Change cruise along 24°N in the Atlantic Ocean (WOCE section A6) during January - February 1998. Technical Report Contribution No. 2056, NOAA/ Pacific Marine Environmental Laboratory.

Meinen, C. S., Garzoli, S. L., Johns, W. E., and Baringer, M. O. (2004). Transport variability of the Deep Western Boundary Current and the Antilles Current off Abaco Island, Bahamas. *Deep-Sea Research I*, 11(51):1397–1415.

Mikolajewicz, U. and Voss, R. (2000). The role of individual air-sea flux components in CO_2-induced changes of the ocean's circulation and climate. *Climate Dynamics*, 16:627–642.

Moles, C., Banga, J., and Keller, K. (2004). Solving nonconvex climate control problems: pitfalls and algorithm performances. *Applied Soft Computing*, 5(1):35–44.

Moles, C., Mendes, P., and Banga, J. (2003). Parameter estimation in biochemical pathways: A comparison of global optimization methods. *Genome Research*, 13(11):2467–2474.

Nakicenovic, N. and Swart, R. (2000). Special report on emission scenarios. Technical report, Intergovernmental Panel on Climate Change (IPCC).

National Research Council (2002). *Abrupt Climate Change: Inevitable Surprises*. R. B. Alley, J. Marotzke, W. D. Nordhaus, J. T. Overpeck, D. M. Peteet, R. A. Pielke Jr., R. T. Pierrehumbert, P. B. Rhines, T. F. Stocker, L. D. Talley, J. M. Wallace, National Academy Press, Washington, D.C.

Natural Environment Research Council (2003). Natural Environment Research Council (NERC), UK, thematic programme: Rapid Climate Change. Available at: http://www.nerc.ac.uk/funding/thematics/rcc/Scienceplan.shtml.

Nordhaus, W. and Popp, D. (1997). What is the value of scientific knowledge? an application to global warming using the price model. *Energy Journal*, 1(18):1–45.

Pacanowski, R. (1995). MOM2 documentation (User's guide and reference manual). Technical Report GFDL Ocean Technical Reports 3, Princeton University.

Parrilla, G., Lavin, A., Bryden, H., Garcia, M., and Millard, R. (1994). Rising temperatures on the subtropical North Atlantic Ocean over the past 35 years. *Nature*, 369:48–51.

Patra, P. K. and Maksyutov, S. (2002). Incremental approach to the optimal network design for CO_2 surface source inversion. *Geophysical Research Letters*, 20(10):No. 1459.

Peck, S. C. and Teisberg, T. J. (1996). Uncertainty and the values of information with stochastic losses from global warming. *Risk Analysis*, 16(2):227–235.

Poje, A. C., Toner, M., Kirwan Jr., A. D., and Jones, C. K. R. T. (2002). Drifter launch strategies based on Lagrangian templates. *Journal of Physical Oceanography*, 32:1855–1869.

Quadfasel, D. (2005). The Atlantic heat conveyor slows. *Nature*, 438:565–566.

Rayner, D. (2005). RRS Discovery Cruise D277/D278 RAPID mooring cruise report February - March 2004. Technical report, Southampton Oceanography Centre, Southampton.

Rayner, P. J., Enting, I. G., and Trudinger, C. M. (1996). Optimizing the CO_2 observing network for constraining sources and sinks. *Tellus*, 48B:433–444.

Redi, M. H. (1982). Oceanic isopycnal mixing by coordinate rotation. *Journal of Physical Oceanography*, 12:1154–1158.

Reichert, B. K., Schnur, R., and Bengtsson, L. (2002). Global ocean warming tied to anthropogenic forcing. *Geophysical Research Letters*, 29(11):1525, doi:10.1029/2001GL013954.

Rintoul, S. R. and Wunsch, C. (1991). Mass, heat, oxygen and nutrient fluxes and budgets in the North Atlantic Ocean. *Deep-Sea Research*, 38, Suppl. 1:S355–S377.

Robbins, P. E. and Toole, J. M. (1997). The dissolved silica budget as a constraint on the meridional overturning circulation of the Indian Ocean. *Deep-Sea Research I*, 44(5):879–906.

Roeckner, E., Bäuml, G., Bonaventura, L., Brokopf, R., Esch, M., Giorgetta, M., Hagemann, S., Kirchner, I., Kornblueh, L., Manzinie, E., Rhodin, A., Schlese, U., Schulzweida, U., and Tompkins, A. (2003). The atmospheric general circulation model ECHAM5, part I: Model description. Technical Report 349, Max Planck Institute for Meteorology.

Roemmich, D. and Wunsch, C. (1985). Two transatlantic sections: Meridional circulation and heat flux in the subtropical North Atlantic Ocean. *Deep-Sea Research*, 32(6):619–664.

Santer, B. D., Mikolajewicz, U., Brüggemann, W., Cubasch, U., Hasselmann, K., Höck, H., Maier-Reimer, E., and Wigley, T. L. (1995). Ocean variability and its influence on the detectability of greenhouse warming signals. *Journal of Geophysical Research*, 100(C6):10693–10725.

Sato, O. T. and Rossby, T. (2000). Seasonal and low-frequency variability of the meridional heat flux at 36°N in the North Atlantic. *Journal of Physical Oceanography*, 30:606–621.

Scheinert, M. (2003). Mechanismen niederfrequenter Schwankungen des westlichen Randstroms im subpolaren Nordatlantik. (Diplomarbeit, in German). Master's thesis, IfM Kiel, Germany.

Schiermeier, Q. (2004). Gulf Stream probed for early warnings of system failure. *Nature*, 427:769.

Schröter, J. and Wunsch, C. (1986). Solution of non-linear finite difference ocean models by optimization methods with sensitivity and observational strategy analysis. *Journal of Physical Oceanography*, 16:1855–1874.

Stammer, D., Tokmakian, R., Semtner, A., and Wunsch, C. (1996). How well does a 1/4° global circulation model simulate large-scale oceanic observations? *Journal of Geophysical Research*, 101:25779–25811.

Stammer, D., Wunsch, C., Giering, R., Eckert, C., Heimbach, P., Marotzke, J., Adcroft, A., Hill, C. N., and Marshall, J. (2002). Global circulation during 1992-1997, estimated from ocean observations and a general circulation model. *Journal of Geophysical Research*, 107(C9):3118–3155.

Stammer, D., Wunsch, C., Giering, R., Eckert, C., Heimbach, P., Marotzke, J., Adcroft, A., Hill, C. N., and Marshall, J. (2003). Volume, heat and freshwater transports of the global ocean circulation 1993-2000, estimated from a general circulation model constrained by World Ocean Circulation Experiment (WOCE) data. *Journal of Geophysical Research*, 108(C1):3007–3030.

Stocker, T. F. and Schmittner, A. (1997). Influence of co_2 emission rates on the stability of the thermohaline circulation. *Nature*, 388:862–865.

Storn, R. and Price, K. (1997). Differential evolution - a simple and efficient heuristic for global optimization over continuous spaces. *Journal of Global Optimization*, 11:341–359.

Talley, L. (2003). Shallow, intermediate, and deep overturning components of the global heat budget. *Journal of Physical Oceanography*, 33:530–560.

Taylor, K. E. (2001). Summarizing multiple aspects of model performance in a single disgram. *Journal of Geophysical Research*, 106(D7):7183–7192.

The International Ad Hoc Detection and Attribution Group (2005). Detecting and attributing external influences on the climate system: a review of recent advances. *Journal of Climate*, 18:1291–1314.

Thorpe, R. B., Gregory, J. M., Johns, T. C., Wood, R. A., and Mitchell, J. F. B. (2001). Mechanisms determining the Atlantic Thermohaline Circulation response to greenhouse gas forcing in a non-flux-adjusted coupled climate model. *Journal of Climate*, 14:3102–3116.

Trenberth, K. E. and Solomon, A. (1994). The global heat balance: Heat transport in the atmosphere and ocean. *Climate Dynamics*, 10(3):107–134.

Vellinga, M. and Wood, R. A. (2002). Global climatic impacts of a collapse of the Atlantic thermohaline circulation. *Climatic Change*, 54:251–267.

Vellinga, M. and Wood, R. A. (2004). Timely detection of anthropogenic change in the atlantic meridional overturning circulation. *Geophysical Research Letters*, 31:L14203, doi: 10.1029/2004GL020306.

Wahr, J., Molenaar, M., and Bryan, F. (1998). Time variability of the Earth's gravity field: Hydrological and oceanic effects and their possible detection using GRACE. *Journal of Geophysical Research*, 103(B3):30,205–20,229.

Wahr, J. M., Jayne, S. R., and Bryan, F. O. (2002). A method of inferring changes in deep ocean currents from satellite measurements of time-variable gravity. *Journal of Geophysical Research*, 107(C12):3218, doi: 1029/2001JC001274.

Webb, D. J. (1996). An ocean model code for array processor computers. *Computers & Geosciences*, 22(5):569–578.

Willebrand, J., Barnier, B., Böning, C., Dietrich, C., Killworth, P. D., le Provost, C., Jia, Y., Molines, J.-M., and New, A. L. (2001). Circulation characteristics in three eddy-permitting models of the North Atlantic. *Progress in Oceanography*, 48:123–161.

Wood, R. A., Keen, A. B., Mitchell, J. F. B., and Gregory, J. M. (1999). Changing spatial structure of the thermohaline circulation in response to atmospheric CO_2 forcing in a climate model. *Nature*, 399:572–575.

Wunsch, C. and Heimbach, P. (2006). Estimated decadal changes in the North Atlantic meridional overturning circulation and heat flux 1993-2004. *Journal of Physical Oceanography*. In press.

Yohe, G. (1991). Uncertainty, climate change and the economic value of information - an economic methodology for evaluating the timing of relative efficacy of alternative response to climate change with application to protecting developed property from greenhouse induced sea-level rise. *Policy Sciences*, 24(3):245–269.

Yohe, G. (1996). Exercises in hedging against extreme consequences of global change and the expected value of information. *Global Environmental Change*, 6:87–101.

ACKNOWLEDGEMENTS

First and foremost I wish to thank my supervisor Jochem Marotzke for his constant guidance and support, enlightening and inspiring discussions, and his reassuring trust and optimism throughout my entire studies.

Many thanks go to my colleagues in our research group, who provided a stimulating and vivid research environment. I also enjoyed the fruitful collaborations with researchers from the National Oceanographic Centre in Southampton, and Penn State University. In particular, I would like to thank Joël Hirschi and Klaus Keller for intensive discussions and continuous encouragement.

The first year of my PhD I spent at the National Oceanographic Centre in Southampton, where I received much appreciated advise form Harry Bryden and Neil Wells in the panel meetings.

I would also like to thank my summer students Vincent Lavalle, Leonid Mordoukhovski, and Adrianne Stroup for their help.

I received invaluable assistance from the library team, the CIS group, and the administration; and - surely not to be forgotten - Kornelia Müller's unique backup with respect to all practical matters of life.

My sincere thanks go to my friends and my family for their unreserved backing and wonderful distractions, and to Thomas for being with me, all the time.

Publikationsreihe des MPI-M
„Berichte zur Erdsystemforschung“ , „*Reports on Earth System Science*“, ISSN 1614-1199
Sie enthält wissenschaftliche und technische Beiträge, inklusive Dissertationen.

Publikationsreihe des MPI-M
„Berichte zur Erdsystemforschung“ , „*Reports on Earth System Science*“, ISSN 1614-1199
Sie enthält wissenschaftliche und technische Beiträge, inklusive Dissertationen.

Berichte zur Erdsystemforschung Nr.16 Oktober 2005	**Aerosol Indirect Effect in the Thermal Spectral Range as Seen from Satellites** Abhay Devasthale
Berichte zur Erdsystemforschung Nr.17 Dezember 2005	**Interactions between Climate and Land Cover Changes** Xuefeng Cui
Berichte zur Erdsystemforschung Nr.18 Januar 2006	**Rauchpartikel in der Atmosphäre: Modellstudien am Beispiel indonesischer Brände** Bärbel Langmann
Berichte zur Erdsystemforschung Nr.19 Februar 2006	**DMS cycle in the ocean-atmosphere system and its response to anthropogenic perturbations** Silvia Kloster
Berichte zur Erdsystemforschung Nr.20 Februar 2006	**Held-Suarez Test with ECHAM5** Hui Wan, Marco A. Giorgetta, Luca Bonaventura
Berichte zur Erdsystemforschung Nr.21 Februar 2006	**Assessing the Agricultural System and the Carbon Cycle under Climate Change in Europe using a Dynamic Global Vegetation Model** Luca Criscuolo
Berichte zur Erdsystemforschung Nr.22 März 2006	**More accurate areal preciption over land and sea, APOLAS Abschlussbericht** K. Bumke, M. Clemens, H. Graßl, S. Pang, G. Peters, J.E.E. Seltmann, T. Siebenborn, A. Wagner
Berichte zur Erdsystemforschung Nr.23 März 2006	**Modeling cold cloud processes with the regional climate model REMO** Susanne Pfeifer
Berichte zur Erdsystemforschung Nr.24 Mai 2006	**Regional Modeling of Inorganic and Organic Aerosol Distribution and Climate Impact over Europe** Elina Marmer
Berichte zur Erdsystemforschung Nr.25 Mai 2006	**Proceedings of the 2nd HyCARE meeting, Laxenburg, Austria, 19-20 Dec 2005** Edited by Martin G. Schultz and Malte Schwoon
Berichte zur Erdsystemforschung Nr.26 Juni 2006	**The global agricultural land-use model KLUM – A coupling tool for integrated assessment** Kerstin Ellen Ronneberger
Berichte zur Erdsystemforschung Nr.27 Juli 2006	**Long-term interactions between vegetation and climate -- Model simulations for past and future** Guillaume Schurgers
Berichte zur Erdsystemforschung Nr.28 Juli 2006	**Global Wildland Fire Emission Modeling for Atmospheric Chemistry Studies** Judith Johanna Hoelzemann
Berichte zur Erdsystemforschung Nr.29 November 2006	**CO_2 fluxes and concentration patterns over Eurosiberia: A study using terrestrial biosphere models and the regional atmosphere model REMO** Caroline Narayan

Publikationsreihe des MPI-M
„Berichte zur Erdsystemforschung“ , „*Reports on Earth System Science*“, ISSN 1614-1199
Sie enthält wissenschaftliche und technische Beiträge, inklusive Dissertationen.



ISSN 1614-1199